University of California
Los Angeles

Optimal Oscillations and Chaos Generation in Biologically-Inspired Systems

A dissertation submitted in partial satisfaction
of the requirements for the degree
Doctor of Philosophy in Mechanical Engineering

by

Saba Kohannim

2016

Abstract of the Dissertation

Optimal Oscillations and Chaos Generation in Biologically-Inspired Systems

by

Saba Kohannim

Doctor of Philosophy in Mechanical Engineering

University of California, Los Angeles, 2016

Professor Tetsuya Iwasaki, Chair

Biological systems display a variety of complex dynamic behaviors, ranging from periodic orbits to chaos. Regular rhythmic behavior, for instance, is associated with locomotion, while chaotic behavior is observed in neural interactions. Both these cases can be mathematically expressed as the interaction of a collection of coupled bodies or oscillators that are actuated to behave with a desired pattern. In animal locomotion, this desired pattern is the periodic body motion (gait) that interacts with the environment to generate thrust for motion. By contrast, the observed behavior of a network of neurons is possibly chaotic and flexible. This research focuses on the design and analysis of these two types of behaviors in biologically-inspired systems.

A fundamental problem in animal locomotion is determining a gait that optimizes an essential performance while satisfying a desired velocity constraint. In this study, a functional model is developed for a general class of three dimensional locomotors with full (six) degrees of freedom, in addition to arbitrary finite degrees of freedom for body shape deformation. An optimal turning gait problem is then formulated for a periodic body movement that minimizes a quadratic cost function while achieving a steady turning motion with prescribed average linear and angular velocities. The problem is shown to reduce equivalently to two separate and simpler minimization problems that are both solvable for globally optimal solutions.

Optimal gait theory can also be utilized in order to determine analytical justifications for observed behavior in biological systems. In this study, a simple body-fluid fish model is developed, and steady swimming at various speeds is analyzed using optimal gait theory. The results show that the gait that minimizes bending moment over tail movements and stiffness matches data from observed swimming of saithe. Furthermore, muscle tension is reduced when undulation frequency matches the resonance frequency, which maximizes the ratio of tail-tip velocity to bending moment.

The final task is to design the interconnections in a network of Andronov-Hopf oscillators in order to generate desired chaotic behavior. Due to the structure of the oscillators, it is possible to generate chaos by using weak linear coupling to destabilize the phase difference between the oscillators. To this end, a set of sufficient conditions are determined to guarantee the instability of a desired periodic solution through phase destabilization. Subsequently, a condition is found to guarantee the absence of any stable harmonic orbit. Finally, additional properties are considered, where small variations in a parameter can lead to chaotic behavior. With additional research, these results can be expanded to the design of a chaotic neural controller to generate adaptive locomotion for a mechanical rectifier.

The dissertation of Saba Kohannim is approved.

Lieven Vandenberghe

Robert Thomas M'Closkey

Jason L. Speyer

Tetsuya Iwasaki, Committee Chair

University of California, Los Angeles

2016

To Andy, who has always been by my side during this entire journey...

...specifically, my left side.

Table of Contents

List of Figures

List of Tables

Acknowledgments

I would like to first thank my advisor Professor teD Iwasaki, who has been my academic role model since the first day of MAE171A, when I was a measly undergraduate student. His knowledge, guidance, patience, and preference of such $\mathcal{N}$o$\mathcal{T}$a$\mathbb{T}i\mathcal{O}\hat{n}s$ has been instrumental to the completion of this dissertation and everything I have learned along the way. I am also extremely thankful for the financial support for this research provided by NSF Graduate Research Fellowship under Grant No. DGE-1144087 and NSF grant no.1068997.

I would like to thank my committee members, Professor Speyer, Professor M'Closkey, and Professor Vandenberghe, for their helpful inputs and constructive criticisms. I am also grateful to all the former and present members of the Cybernetic Control Lab, particularly Dr. Xinmin Liu for being such a helpful mentor. This dissertation would also not be possible without the continuous assistance of all the MAE staff, especially Angie, Abel, and Lance.

I am grateful to all the life-long friends I have made during graduate school including, but not limited to, Andy, Chin, Luke, Nolan, and Mike. I can't imagine where I would be without this network of amazing individuals. They provided the necessary outlet from the stress of research, and made this journey fun and memorable. I am also thankful for my non-graduate school friends who continuously put up with my busy schedule, and were always there to make holidays and celebrations magical. I am indebted to my best friend Evelyn, who has been my confidant since we were melodramatic preteens. I am grateful to my parents for teaching me the value of education, and eventually supporting me in all of my decisions. I also need to thank my brother for teaching me math and science lessons that were four years above my level.

Last but not least, I would like to thank bouldering and foosball for being my rock and roll. While I wish I had found my passion for these hobbies sooner in life, I cannot imagine sharing this discovery alongside anyone else.

Vita

2011	B.S. (Mechanical Engineering), University of California, Los Angeles, CA
2013	M.S. (Mechanical Engineering), University of California, Los Angeles, CA
2011-2016	Graduate Student Researcher, Mechanical and Aerospace Engineering Department, University of California, Los Angeles, Los Angeles, CA
2016	Teaching Assistant, Mechanical and Aerospace Engineering Department, University of California, Los Angeles, Los Angeles, CA

Publications

S. Kohannim and T. Iwasaki, "Dynamical model and optimal turning gait for mechanical rectifier systems," *IEEE Transactions on Automatic Control* (May 2017).

S. Kohannim and T. Iwasaki, "Analytical insights into optimality and resonance in fish swimming," *Journal of The Royal Society Interface*, vol. 11, no. 92, 2014.

S. Kohannim and T. Iwasaki, "Optimal turning gait for mechanical rectifier systems with three dimensional motion," in *Decision and Control (CDC), IEEE*, 2014, pp. 5862–5867.

S. Kohannim, J. Chen, and T. Iwasaki, "Optimality analyses of carangiform and anguilliform swimming", in *The 7th World Congress of Biomechanics*, July 2014.

S. Kohannim and T. Iwasaki, "Resonance in fish swimming to minimize muscle tension", in *Proceedings of The Society for Integrative & Comparative Biology Annual Meeting*, 53:E311

- E311, January 2013.

S. Kohannim and T. Iwasaki, "Optimal turning gait for undulatory locomotion," in *American Control Conf. (ACC), 2012 IEEE*, 2012, pp. 3459–3464.

CHAPTER 1

Introduction

Various complex dynamic behaviors, ranging from stable periodic limit cycles to chaos, have been observed and studied in healthy biological systems. An essential example of regular rhythmic behavior observed in biology is animal locomotion, i.e. walking, flying, swimming, and crawling. Animal locomotion can be regarded as a type of mechanical rectification, in which sustained propulsive forces are produced through the interaction of the environment with the animal's periodic body motions (gaits) [3, 4, 5]. The specific periodic gait of an animal is chosen depending on its body conditions and environmental effects, as well as its desired locomotion speed and path. Due to their observed adaptability, agility, and robustness properties, animal locomotion has motivated the design of robotic vehicles that possess these same qualities. Mathematical and engineering tools can be effectively used in the design of efficient robotic systems; furthermore, they can also be used to analyze and explain observed behaviors and tendencies in natural locomotion.

In contrast to the rhythmic behavior of animal locomotion, evidence of chaos is prevalent in various biological systems, particularly in neural and brain dynamics and cardiac rhythm. Chaotic behavior has been observed in both single neurons, as well as groups of neurons that belong to a small functional network, such as the central pattern generator (CPG) [6, 7, 8]. The CPG comprises of a group of coupled neurons or oscillators located within the central nervous system that control motor activities [9]. Although CPGs produce periodic patterns, the neurons in the CPG present chaotic behavior,which is believed to be responsible for the CPG's flexibility to quickly adapt to environmental changes [10]. One popular hypothesis for the existence of chaotic regimes in neural networks is the ability to stabilize an unstable periodic orbit embedded in a strange attractor with minimal cost [6].

In this research, we focus on two fundamental questions in the study and design of dynamic behavior in biologically-inspired systems. The first problem is determining possible appropriate gaits of an animal given its environment and desired tasks. The optimal solution of this question can then be used to analytically study natural gaits observed in biology. The second problem is determining the interconnections between a group of coupled oscillators or neurons in order to generate desired chaotic behavior embedded in a strange attractor. The purpose of this research is to analytically pose and solve these questions and provide numerical support for the solutions.

The first essential problem in the design of biologically-inspired robotic locomotors is determining a gait that optimizes an important performance or cost function while satisfying a desired trajectory constraint. This problem has been studied extensively in the literature for various mechanical rectifiers, but due to inherent difficulties, most existing results only provide solutions that are locally optimal. For locally optimal solutions, a standard approach is based on nonlinear optimal control theory. For example, in [11], Pontryagin maximum principle is used to characterize the optimal gait of a seven-link biped robot in terms of a two-point boundary value problem. A similar method was used in discrete-time setting [12] to solve for snake-like link structures. Another popular approach is to reduce the problem to a finite dimensional parametric optimization. In [13] and [14], this approach is taken to find optimal gaits for an underwater eel-like robot and for a nonholonomic snakeboard, respectively, by solving a stationarity condition using Newton iteration algorithms. The parametric approach is also used for biped robots with direct numerical optimizations through sequential quadratic programming [15, 16], steepest gradient descent method [17], and a commercial software package [18].

There are a few approaches for computing global solutions of certain optimal gait problems. One approach is inspired by biology, where an optimization problem is formulated over a narrow set of possible gaits that are observed in animal locomotion. Since the parameter space of various gaits is restricted, it is possible to find the globally optimal solution by simulations on gridded parameter points [19] or by analytical perturbation methods [20]. These methods find reasonable gaits, but can miss better gaits that deviate from those observed

in biology. Another approach to globally optimal gaits is to restrict the class of underlying locomotion dynamics rather than the class of possible gaits. Reference [21] considers a general class of mechanical rectifiers that are in continuous interactions with the environment, including swimming, flying, and slithering. A simplified bilinear model is developed under the assumption of small curvature deformation, capturing essential rectifier dynamics necessary for locomotion. An optimal gait problem is then formulated as a minimization of a quadratic cost function over all periodic body movements achievable with a given set of actuators, subject to a constraint on the average locomotion velocity. The globally optimal solution is obtained using generalized eigenvalue computation, and the method's utility is validated by case studies of a link-chain rectifier swimming in water.

The methods mentioned above are primarily used to find optimal gaits for locomotion along a straight line, but the problem can also be extended for turning along a curved path. Turning motion has been investigated by [12, 20, 22] for planar eel swimming and snake crawling. In all these cases, a constant offset is added to the harmonic shape variable to achieve turning; however, only the harmonic terms are included in the optimization and the offsets are set to prescribed values, with no basis for the separation of the offset terms from the periodic terms. Thus, it remains open how to optimize the gait for turning locomotion in three dimensional space while minimizing a general cost function.

In our research, we address this open problem; we develop a functional model for a general class of mechanical rectifiers in three dimensional space, and extend the approach by [21] to find globally optimal gaits that satisfy a desired steady turning constraint. We then use the tools from the optimal gait analysis in order to find simple analytical justifications for the observed gait and oscillation frequencies of swimming fish.

Fish swim by generating thrust through interactions between their body movement and the surrounding water. Studies of fish locomotion aim to understand how fish choose a frequency and gait of tail oscillation, how thrust is generated efficiently through hydrodynamic forces, and how body shape and muscle activation are adjusted to regulate swim speed. Fish locomotion has been investigated using various methods, including kinematic and biomechanical data analysis of live fish, swimming experiments using flexible fish body models,

and computational/experimental analyses of oscillating foils in fluids. Several theories have been formulated using these methods.

One prevalent theory is that fish minimize mechanical bending cost, or maximize thrust, by tuning their natural frequency to the tail-beat frequency [23, 24]. Studies suggest that fish use their muscles, skin, and tendons, to alter their body stiffness to achieve the required natural frequency [25, 26]. Previous studies on the relationship between tail-beat frequency, amplitude, and speed have concluded a linear relationship between speed and frequency [27, 28]. Experimental data on pumpkinseed sunfish suggest that fish increase their flexural stiffness to increase their tail-beat frequency to achieve faster swimming speeds, while maintaining constant tail-tip amplitudes [29].

Thrust production in swimming has been analyzed through vortex structure and energy expenditure of the wake. Experiments on foils oscillating in fluids have demonstrated that maximum thrust occurs when the nondimensional Strouhal number is within 0.25-0.35 [30], agreeing with values observed in biology 0.2-0.4 [31]. Optimum hydrodynamic efficiency is achieved when foil oscillation frequency coincides with the frequency of maximum spatial amplification of unstable wake [32], or "wake resonance frequency" [33, 34].

The results of our research using optimal gait analysis shows that the optimal gait which minimizes bending moment or muscle tension, closely resembles observed swimming gait. Furthermore, minimizing muscle tension explains the observed tendency of increasing tail-beat frequency and stiffness to achieve higher velocities, while maintaining constant tail amplitude. The optimal frequency occurs at the resonance which maximizes the ratio of tail-tip velocity to bending moment; this resonance results from both the body resonance and the fluid resonance.

The final task of this research is to design the coupling between oscillators or neurons to generate chaotic behavior, similar to what is observed in many biological systems. According to [35], various human rhythmic movements result from chaotic motion on strange attractors. Chaotic regimes have also been observed in the nervous system [36] and neural assemblies, and are known to promote adaptability and flexibility [10]. Chaos has also been found

to be related to neuromuscular control of locomotion [37]. For example, in [38], arm and leg movements of skiers were found to fluctuate in a chaotic manner as they adapted to environmental perturbations. According to [39], chaos in the CPG allows for rapid switching to multiple stable gaits available in the attractor.

Based on the observed benefits of chaotic neuronal control, various papers have attempted to control locomotion using chaos. In [40], chaos control was used to generate complex behavior for an autonomous six-legged robot. The discrete-time chaotic CPG reliably switched between various periodic gaits. In [41], distributed chaotic elements coupled with musculoskeletal system showed adaptability to changes in body-environment dynamics. In [42], a CPG modeled with four coupled chaotic Rössler oscillators recovered various natural gaits in animals.

Although these papers motivated the application of chaos in neural control for locomotion, they did not design the interconnections between oscillators to generate chaotic behavior on a desired strange attractor. To our knowledge, there is currently no methodological and analytical method for designing coupled chaotic oscillators. In [43] and [44] chaos in coupled Kuramoto oscillators was discovered using phase destabilization. However, subsequent works on the design of desynchronization of coupled oscillators using delayed-feedback required simulation results and parameter tuning [45, 46, 47]. Most recently, [48] provided semi-analytical guidelines for designing a chaotic system. However, their method requires nonlinear control, and does not apply to systems where the necessary nonlinearity is embedded in the plant. Additionally, the final chaotic motion is not on a desired strange attractor. Therefore, it remains open how to design chaotic coupled oscillators with desired limit cycles embedded in the strange attractor.

This research seeks to solve this open problem. We consider a set of linearly coupled two-dimensional Andronov-Hopf oscillators, and find conditions on the interconnections to generate chaos with a desired unstable limit cycle embedded in the strange attractor.

This dissertation is organized as follows. In Chapter 2, we develop the dynamic model and optimal turning gait analysis for a general mechanical rectifier in three dimensional space.

In Chapter 3, we use optimal gait analysis to provide analytical insights into the observed carangiform swimming of saithe fish and the hypothesis that fish exploit resonance to reduce the cost of swimming. In Chapter 4, we determine conditions on the interconnections between a set of coupled Andronov-Hopf oscillators in order to generate desired chaotic behavior. Finally, in Chapter 5, we provide concluding remarks and discuss future works that remain open for further study.

Notations: The set of positive integers is denoted by $\mathbb{Z}$. The sets of n by m real and complex matrices are denoted by $\mathbb{R}^{n\times m}$ and $\mathbb{C}^{n\times m}$ respectively. For vectors f and x, the $(i,j)^{th}$ entry of $\partial f/\partial x$ is given by $\partial f_j/\partial x_i$. For a complex matrix X, the transpose, complex conjugate transpose, and real part are denoted by $X^\intercal$, X^*, and $\Re[X]$ respectively. The matrix (or vector) obtained by stacking matrices X_i, $i \in \mathbb{Z}_n$, in a column is denoted by $\mathrm{col}(X_1,\ldots,X_n)$. Similarly, $\mathrm{diag}(X_1,\ldots,X_n)$ denotes the block diagonal matrix with X_i stacked on the diagonal. The eigenvalues with the smallest and largest real parts of a matrix X are denoted by $\underline{\mathrm{eig}}(X)$ and $\overline{\mathrm{eig}}(X)$, respectively.

CHAPTER 2

Dynamic Model and Optimal Turning Gait Analysis for Mechanical Rectifiers

2.1 Overview

The purpose of this chapter is to develop a functional model for a general class of mechanical rectifiers in three dimensional space, and extend the approach by [21] to find globally optimal gaits that satisfy a desired steady turning constraint. We consider a multi-body mechanical rectifier with full (six) degrees of freedom (DOF) for position and orientation within the inertial frame, in addition to arbitrary finite degrees of freedom for body shape deformation. The body is assumed to be in continuous contact with its environment, receiving environmental forces that are proportional to the relative velocities with directional preference. This class of rectifier systems has been considered in [21], where the equations of motion are derived within the inertial frame. We build on the previous result and transform the equations of motion into body coordinates in order to provide a comprehensible description of the dynamics for arbitrary three dimensional maneuvers from the "pilot's view", and independent of an inertial frame. A mathematical proof is given to confirm the physical intuition that dynamics of body shape and linear/angular velocities are independent of body orientation. Assuming small body deformation, the nonlinear model is reduced to a simplified model that is tractable and captures the essential rectifying dynamics.

An optimal turning gait problem is then formulated for the simplified model as the search for a periodic body movement that minimizes a quadratic cost function while achieving a steady turning motion with prescribed linear and angular velocities on average over each cycle. Similar to the previous methods mentioned above, shape offsets are added to the

periodic shape variables to allow for turning motion; however, in this case the shape offsets are not specified *a priori*, but included in the optimization. The problem is shown to reduce equivalently to two separate and simpler minimization problems that are both solvable for globally optimal solutions. The first problem solves for the nominal (fixed) body shape that yields the desired turning rate while minimizing the additional drag due to turning. The second solves for the optimal periodic body movement that would minimize the cost function if the locomotion were achieved at the prescribed tangential speed without the turning constraint, under increased environmental drag and modified body dynamics. Thus, our main result proves a separation principle in optimal turning gait where the cost function and optimization variables can both be decoupled into rotational and translational terms. The rotational problem is a simple convex optimization and we provide an analytical solution, while the translational problem takes the same form as the one solved in [21] in terms of generalized eigenvalues, where a harmonic gait is shown to be optimal. The utility of the developed model and the optimal turning gait results are tested by a numerical case study of an arbitrary swimming locomotor designed to allow thrust generation in roll, pitch, and yaw turning directions.

2.2 Mechanical Rectifier System

We consider a general mechanical system composed of multiple rigid bodies that are connected arbitrarily to each other at rigid or flexible joints with rotational and/or linear degrees of freedom. The shape of the system is defined by relative positions and orientations of the multiple bodies, and can be deformed through actuators placed at some of the joints. The multi-body system can rotate and translate in three-dimensional space due to interactive forces resulting from continuous contact with the environment (e.g. water, air, ground). We assume that the gravity effect can be neglected due to e.g. neutral buoyancy of the system in a fluid. When the system interacts with the environment to convert periodic body motion to a net thrust over each cycle, we call it a mechanical rectifier. Such systems would represent animal locomotions or their robotic realizations such as fish and batoid swimming,

eel/serpent slithering, and balloon flight with flapping wing.

The environmental force on each body is roughly modeled as a static linear function of the relative velocities seen from the body frame. The linear dependence of the force on velocity is meant to capture the qualitative nature of resistive interactions with the environment in various contexts (hydrodynamic drag in swimming, Coulomb friction in slithering, etc.). The values of the drag coefficients are chosen to quantitatively dictate the net effect over each cycle of body oscillation. For instance, hydrodynamic force in swimming may be modeled by a nonlinear function of the velocity $f(v)$ [49, 50]. However, if the velocity is roughly sinusoidal $v(t) \cong a\sin(\omega t + b)$ during periodic body movements, the net effect of the nonlinear force may be approximated by a Fourier series truncation to yield the linear term $f(v) \cong \kappa(a)v$ where $\kappa(a)$ is the describing function [51]. The truncated higher order harmonics would have a small impact on the overall behavior if they are damped out due to the low pass filtering effect of the body dynamics with inertia.

The next sections outline the derivation of analytical models for mechanical rectifiers, with supplementary details given in the Appendix. The equations of motion with respect to the inertial frame can be developed through the Euler-Lagrange equation, using a set of generalized coordinates as in [21]. However, our goal is to analyze turning motion of the rectifier with a fixed average locomotion speed and angular velocity. Therefore, we will develop equations of motion with respect to a body frame, so that the dynamics are described independently of the position and orientation with respect to the inertial frame, as a consequence of the symmetry/invariance property of the environmental forces. The equations of motion are then reduced, assuming small body oscillations, to a simpler state space form that is reasonably accurate, tractable, and usable for analytical study of optimal gaits for turning.

2.2.1 General Equations of Motion

This section provides a brief summary of equations of motion for the mechanical rectifier described in the inertial frame. The equations have been derived in [21] at a conceptual

level as outlined here, and further details of the model equations, not worked out in [21] but necessary for the coordinate transformation in the next section, are presented in the appendix.

A mechanical rectifier in three dimensional space has $n = 6 + \ell$ degrees of freedom, describing its position (3 DOF), orientation (3 DOF), and flexible body shape (ℓ DOF). In particular, the motion can be described by the generalized coordinates $q := \mathrm{col}(w, \theta)$, where $w(t) \in \mathbb{R}^3$ is the position of the center of mass of the entire system and $\theta(t) \in \mathbb{R}^{\ell+3}$ are the variables specifying the orientation and shape of the multi-body system. The equations of motion for a general mechanical rectifier can be developed using the Euler-Lagrange equation given by

$$\frac{d}{dt}\left(\frac{\partial L}{\partial \dot{q}}\right) - \frac{\partial L}{\partial q} = \hbar, \tag{2.1}$$

where $L := \mathrm{T} - V$ is the Lagrangian, $\mathrm{T}(q, \dot{q}) \in \mathbb{R}$ is the total kinetic energy of the system, $V(q) \in \mathbb{R}$ is the total potential energy, and $\hbar(t) \in \mathbb{R}^n$ are the generalized forces.

The total kinetic energy of the system T includes the translational kinetic energy of each body's center of mass plus the rotational kinetic energy around each body's center of mass. Using the generalized coordinates q, T is given by

$$\mathrm{T}(q, \dot{q}) = \frac{1}{2} m ||\dot{w}||^2 + \frac{1}{2} \dot{\theta}^{\mathsf{T}} \mathrm{J}(\theta) \dot{\theta}, \tag{2.2}$$

where m is the total mass, and $\mathrm{J}(\theta)$ represents the moment of inertia matrix. The total potential energy of the system V captures the elastic potential energy associated with body deformation and is only a function of the shape of the mechanical rectifier, i.e. $V = V(\theta)$.

The generalized forces consist of environmental forces $\hbar_e(t) \in \mathbb{R}^n$ and actuator input forces $\hbar_a(t) \in \mathbb{R}^n$, so that $\hbar = \hbar_e + \hbar_a$. We assume an environmental force acts on each surface area segment of each body, and roughly estimate that the force is proportional to the velocity in each direction of each body's coordinates. Therefore, the force from the environment, acting on an infinitesimal segment on the surface of body i (Fig. 2.1), is assumed to be resistive and proportional to the velocity $\dot{\sigma}_i(\mathrm{s})$ of point c in the local body frame, and is given by

$$df_i = -\Omega(\psi_i)^{\mathsf{T}} \Delta_i \Omega(\psi_i) \dot{\sigma}_i(\mathrm{s}) da_i,$$

where $\Delta_i \in \mathbb{R}^{3\times 3}$ is a constant matrix of drag/friction coefficients, s is the vector from the center of mass of body i to point c, $\dot{\sigma}_i(\mathrm{s})$ is the velocity of point c, and da_i is the surface area of the segment. The virtual work done on the segment is $\delta W_i(\mathrm{s}) = \delta\sigma_i(\mathrm{s})^\intercal df_i$, where $\delta\sigma_i(\mathrm{s})$ is the virtual displacement. Integrating over body i's surface and summing over all bodies, the generalized environmental forces are then given by

$$\hbar_e = -\begin{bmatrix} \mathsf{C}(\theta) & \mathsf{E}(\theta)^\intercal \\ \mathsf{E}(\theta) & \mathsf{D}(\theta) \end{bmatrix} \begin{bmatrix} \dot{w} \\ \dot{\theta} \end{bmatrix}, \tag{2.3}$$

for coefficient matrices $\mathsf{C}(\theta)$, $\mathsf{D}(\theta)$, and $\mathsf{E}(\theta)$ defined in the appendix.

In order to calculate the generalized forces due to actuator inputs, we let $u(t) \in \mathbb{R}^r$ be the actuator force/torque inputs, and assume that their displacements are linear functions of shape variables given by $\mathsf{B}^\intercal q$ for a coefficient matrix $\mathsf{B} \in \mathbb{R}^{n\times r}$ with its first six rows being zero. Then, the generalized force of actuators can be expressed as

$$\hbar_a = \mathsf{B}u, \qquad \mathsf{B} := \begin{bmatrix} 0 \\ B \end{bmatrix},$$

where B denotes the bottom $(\ell+3)\times r$ block of B.

Using the given expressions for kinetic energy, potential energy, and generalized forces, the Euler-Lagrange equation reduces to the following two equations of motion:

$$\begin{aligned} &\mathsf{J}(\theta)\ddot{\theta} + \mathsf{G}(\theta,\dot{\theta})\dot{\theta} + \mathsf{D}(\theta)\dot{\theta} + \mathsf{E}(\theta)\dot{w} + k(\theta) = Bu, \\ &m\ddot{w} + \mathsf{C}(\theta)\dot{w} + \mathsf{E}(\theta)^\intercal\dot{\theta} = 0. \end{aligned} \tag{2.4}$$

The terms $\mathsf{J}(\theta)\ddot{\theta} + \mathsf{G}(\theta,\dot{\theta})\dot{\theta}$ and $m\ddot{w}$ are the inertial torques and forces, $\mathsf{D}(\theta)\dot{\theta} + \mathsf{E}(\theta)\dot{w}$ and $\mathsf{C}(\theta)\dot{w} + \mathsf{E}(\theta)^\intercal\dot{\theta}$ capture the environmental torques and forces, $k(\theta)$ are the torques due to body stiffness, and $u \in \mathbb{R}^r$ are the forces/torques applied through actuators.

2.2.2 Coordinate Transformation

The general equations of motion in (2.4) describe the dynamics of the mechanical rectifier with respect to the inertial frame. Our goal is to analyze turning motion of the mechanical rectifier with a fixed average locomotion speed and a fixed average angular velocity. In order

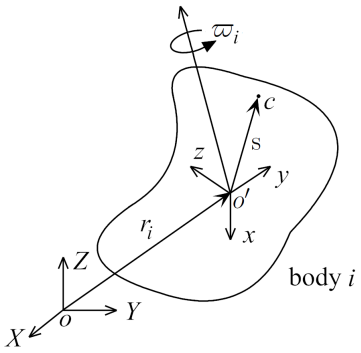

Figure 2.1: Coordinates for body i in the mechanical rectifier

to achieve this, we use a coordinate transformation to derive another set of equations of motion that are equivalent to (2.4), but expressed with respect to a body frame. This new model will show more explicitly how the dynamics are related to shape, orientation, and velocity.

To this end, consider a particular body i in the rectifier in an inertial reference frame with (X, Y, Z)-axes and origin at point o (Fig. 2.1). The orientation of body i can be described by a rotated reference frame fixed on the body with (x, y, z)-axes, which can be related to the inertial frame with a sequence of three elemental rotations or Euler angles. Let $\psi_i \in \mathbb{R}^3$ be a stacked vector of the Euler angles that specify the orientation of body i with respect to the inertial frame. For a given vector, its inertial coordinates $\mathrm{v} := \mathrm{col}(v_X, v_Y, v_Z)$ are related to the body coordinates $v := \mathrm{col}(v_x, v_y, v_z)$ by $v = \Omega(\psi_i)\mathrm{v}$, where $\Omega(\psi_i) \in \mathbb{R}^{3\times 3}$ is an orthogonal rotation matrix defined by the Euler angle sequence.

We now introduce a coordinate transformation by arbitrarily picking one of the multiple bodies forming the rectifier as a reference for orientation and calling it body B. Let us first choose $\theta := \mathrm{col}(\psi, \phi)$, where $\psi \in \mathbb{R}^3$ describes the orientation of body B, and $\phi \in \mathbb{R}^\ell$ are the orientation and position of the remaining bodies with respect to body B, representing the shape of the rectifier. The angular velocity of body B, $\varpi \in \mathbb{R}^3$, can be expressed in the body frame as

$$\varpi := P(\psi)\dot{\psi},$$

where $P(\psi) \in \mathbb{R}^{3\times 3}$ is a matrix-valued function uniquely determined from the choice of the

Euler angle sequence. Define the velocity of the center of mass with respect to body B's frame:

$$\boldsymbol{\nu} := \mathrm{col}(\boldsymbol{\nu}_x, \boldsymbol{\nu}_y, \boldsymbol{\nu}_z) := \Omega(\psi)\dot{w},$$

where $\boldsymbol{\nu}_x$, $\boldsymbol{\nu}_y$, and $\boldsymbol{\nu}_z$ are the velocity components along the respective axes of the body frame. We consider the following coordinate transformation:

$$(w, \dot{w}, \psi, \dot{\psi}, \phi, \dot{\phi}) \leftrightarrow (w, \boldsymbol{\nu}, \psi, \varpi, \phi, \dot{\phi}),$$

where the left hand side is the state variables for the original system in (2.4), and the right hand side is the new state variables by which we will describe the rectifier motion.

With the coordinate transformation, the equations of motion can now be written as

$$\begin{aligned} &\mathcal{J}(\phi)\ddot{\xi} + g(\phi, \dot{\xi}) + \mathcal{D}(\phi)\dot{\xi} + \mathcal{E}(\phi)\boldsymbol{\nu} + \mathsf{k}(\phi) = Bu, \\ &m\dot{\boldsymbol{\nu}} + mQ(\varpi)\boldsymbol{\nu} + \mathcal{C}(\phi)\boldsymbol{\nu} + \mathcal{E}(\phi)^{\intercal}\dot{\xi} = 0. \end{aligned} \tag{2.5}$$

where the variable $\dot{\xi} \in \mathbb{R}^{\ell+3}$ is defined as a stacked vector containing the angular velocity of body B and the shape derivative, i.e., $\dot{\xi} := \mathrm{col}(\varpi, \dot{\phi})$. Details of the derivation are given in the appendix. The original equations in (2.4) are expressed with respect to the inertial frame, and therefore the coefficient matrices all depend on the rectifier's orientation ψ. When the equations are viewed from the reference frame of body B, however, this dependence on the orientation changes. All the coefficient matrices in (2.5) are independent of the rectifier's orientation and only functions of the rectifier's shape ϕ and angular velocity ϖ. The body orientation ψ never appears in the equations, similar to how the position w of the center of mass never appears in the equations. These properties allow us to specify desired nominal locomotion velocity and angular velocity in the optimal gait problem.

Let us conceptually explain why the coefficient matrices are independent of the body orientation ψ (see the appendix for mathematical justification). The environmental forces acting on the rigid bodies of the rectifier were estimated to be static functions of the *relative* velocities; therefore, the coefficient matrices for the environmental forces in the new model, $\mathcal{D}(\phi)$, $\mathcal{E}(\phi)$, $\mathcal{C}(\phi)$, are independent of the orientation and only a function of the shape ϕ. For a mechanical rectifier consisting of multiple bodies, the moment of inertia matrix in

the inertial frame, $\mathsf{J}(\theta)$ in (2.4), depends on the orientation, but $\mathcal{J}(\phi)$ in (2.5) with respect to the body frame, will be a function of only the shape of the rectifier and the mass distribution of each body. Overall, the entire dynamics in the body frame are free from the body orientation ψ, including the $g(\phi, \dot{\xi})$ term in (2.5), whose independence from ψ is proven mathematically in Lemma 11 in the appendix. The result is not surprising if we consider the dynamics intuitively. To gain this intuition, we imagine an animal swimming in a vast three dimensional ocean with no sense of a fixed inertial frame such as the water surface or ocean floor. Without any reference to a fixed frame, the animal can still swim and turn in any trajectory with respect to its own body's frame. We expect then, that the output body shape and velocity of the animal, given the input torques at the joints, will not depend on the orientation of the animal.

Finally, the $Q(\varpi)$ term in the second equation of (2.5) arises from the fact that the linear acceleration $\ddot{w}$ is seen in the body frame as $\Omega(\psi)\ddot{w} = \dot{\nu} + Q(\varpi)\nu$. With the choice of the variable $\dot{\xi}$, the torque vector due to body stiffness $\mathsf{k}(\phi)$ depends only on the body shape ϕ and has zeros in its first three elements to have no direct influence on rotational torque on the whole body. Similarly, since the displacements of the actuator inputs are functions of the shape variables, the first three rows of matrix B are zero.

2.2.3 Approximate Model for Trimmed Locomotion

In order to analyze the locomotion mechanism of a mechanical rectifier (2.5), and formulate a tractable and meaningful optimal turning gait problem, we develop the simplest approximated model that still captures the essential rectifying dynamics. We focus on a trim condition for steady turning locomotion where the rectifier body moves through space at a constant speed ν and angular velocity ϖ. Since the thrust is generated by rectifying the effect of periodic body oscillation, the actual values of ν and ϖ oscillate around fixed constants. The objective is to develop a simple model that captures the perturbed dynamics around the trim condition, including the thrust generation mechanisms.

In [21], simplified equations of motion for a general mechanical rectifier in a similar

form to (2.5), but in the inertial frame, were developed to capture the dynamics during locomotion *along a straight line*. The simple model was used for analytical study of optimal gaits and was shown to be valid for snake-like undulation and jellyfish-like flapping of link-chain locomotors in comparison with numerical simulations of the original nonlinear model. In their approach, it was assumed that the body oscillated about some nominal posture, defined as a fixed body shape and orientation that allow coasting along a straight line in the absence of any actuator inputs. The oscillation about the nominal posture was assumed small and of order ϵ, and Taylor series expansions were used to reduce the equations to their simplest forms by retaining up to second order $\mathcal{O}(\epsilon^2)$ terms that had essential contribution to the thrust generation.

Here, we use a similar approach to [21], but modify it to make it applicable for turning motion. Since body orientation ψ does not appear in the new equations of motion (2.5), there is no need to introduce nominal orientation angles. This feature is essential for turning analysis. We consider the nominal body shape ϕ defined as follows. Let $\mathbb{V} \subset \mathbb{R}^3$ be a linear subspace (straight line) indicating the intended direction of locomotion in the body frame. The shape $\phi(t) \equiv \eta \in \mathbb{R}^\ell$ is said to be nominal along $\mathbb{V}$ if

$$\mathsf{k}(\eta) = 0, \qquad \mathcal{E}(\eta)\mathbb{V} = 0, \qquad \mathcal{C}(\eta)\mathbb{V} \subseteq \mathbb{V}. \tag{2.6}$$

Under these conditions, $(\varpi, \phi, \dot{\phi}) = (0, \eta, 0)$ satisfies (2.5) with some $\boldsymbol{\nu}(t) \in \mathbb{V}$ and $u(t) \equiv 0$, which can be physically interpreted as follows. At a nominal shape, the body is at rest with minimum elastic potential ($\mathsf{k}(\eta) = 0$), and the rectifier can coast without changing its orientation or shape under no actuator inputs ($\mathcal{E}(\eta)\mathbb{V} = 0$), while keeping the same direction of locomotion velocity ($\mathcal{C}(\eta)\mathbb{V} \subseteq \mathbb{V}$).

We consider the situation where a small body deformation $\varphi(t) := \phi(t) - \eta$ around a nominal shape η achieves steady turning with nearly constant speed $\boldsymbol{\nu}$ and angular velocity ϖ. Without loss of generality, we choose the body frame so that the rectifier travels in the y-axis direction during an intended locomotion; $\mathbb{V} = \{ve_2 : v \in \mathbb{R}\}$, where $v := \boldsymbol{\nu}_y$ is the tangential velocity, and $e_i \in \mathbb{R}^3$ is a vector whose i^{th} entry is one and all others are zero. This setting allows us to neglect higher order terms of angular acceleration $\dot{\varpi}$ and normal

velocity components $\delta := \mathrm{col}(\nu_x, \nu_z)$, which are perpendicular to the direction of locomotion. Assuming that φ, δ, and $\dot{\varpi}$ are small and of order ϵ, we use Taylor series expansions, like in [21], and linearize the shape equation or the first equation in (2.5), as well as the normal velocity equation for $\dot{\delta}$. However, we keep up to the quadratic or $\mathcal{O}(\epsilon^2)$ terms in the tangential velocity equation for $\dot{v}$ to keep the thrust term embedded in $\mathcal{E}(\phi)^\intercal \dot{\xi}$, which would be lost if linearized. Note that neither turning rate ϖ nor locomotion speed v is assumed small, and all the terms associated with these variables are retained.

The general equations of motion in (2.5) then reduce to (see the Appendix for details)

$$\begin{aligned} \dot{x} &= \mathcal{A}(\varpi, v)x + \mathcal{B}u, \\ \dot{v} &= (\mathfrak{b}^\intercal x - \mathfrak{a})v + x^\intercal \mathcal{S}(\varpi, v)x, \end{aligned} \qquad x := \mathrm{col}(\varpi, \dot{\varphi}, \delta, \varphi), \tag{2.7}$$

where $v := \nu_y \in \mathbb{R}$, $\delta := \mathrm{col}(\nu_x, \nu_z) \in \mathbb{R}^2$, and $\varphi := \phi - \eta \in \mathbb{R}^\ell$. All the coefficients are a function of the nominal shape η. Coefficients $\mathfrak{a}$, $\mathfrak{b}$, and $\mathcal{B}$ are constant scalar, vector, and matrix, and $\mathcal{A}(\varpi, v)$ and $\mathcal{S}(\varpi, v)$ are affine in $\mathrm{col}(\varpi, v)$ except that the last ℓ columns of $\mathcal{A}(\varpi, v)$ have additional terms that are quadratic in ϖ. Furthermore, $\mathcal{S}(\varpi, v)$ is symmetric and has zeros in its first 3×3 block. The parameter $\mathfrak{a}$ is positive, representing the drag from the environment under the nominal condition $x = 0$. These properties become useful when formulating and solving the optimal turning gait problem.

The definition of nominal shape in (2.6) may not be the best for turning motion analysis since the trim condition results in coasting along a straight line. Alternatively, a nominal shape could be defined to maintain a specified locomotion speed and nonzero angular velocity given a known constant actuator input to keep the shape and a fictitious thrust to sustain the speed. However, finding such a nominal shape is strenuous as it requires solving a complex nonlinear vector equality. Instead, we define the nominal shape by more tractable condition (2.6) that is generically satisfied by well-designed mechanical rectifiers with streamlined bodies, like those found in nature.

The nominal shape would typically have some symmetry to maintain straight coasting, but body oscillation around an asymmetric shape can be needed for turning. We use model (2.7) and optimal gait analysis to find the optimal body shape offset that satisfies the desired

angular velocity. This process is guaranteed to work only when the desired turning can be achieved by small body shape offsets because model (2.7) assumes small body deformation around a nominal shape. However, a large body shape offset that achieves higher desired turning rates may be found through an iteration process, where the optimal gait analysis defines the nominal shape used in the next iteration step, which maintains a specific angular velocity at a desired locomotion speed.

2.3 Optimal Turning Locomotion

We will formulate an optimal turning gait problem and provide a solution to find the best body oscillation of the mechanical rectifier that achieves steady locomotion with a desired speed and turning rate on average. The problem formulation and solution are based on the simplified model in (2.7); however, functionality of the result will be confirmed later for the original model (2.5) through a case study.

2.3.1 Problem Statement

We seek the optimal periodic gait $\varphi(t)$ and corresponding periodic control input $u(t)$ that minimizes a quadratic cost function, subject to constraints on the average locomotion velocity v and angular velocity ϖ, with normal velocities δ oscillating about zero. The optimal turning gait problem is formulated for the mechanical rectifier (2.7) as follows:

$$\min_{\tau\in\mathbb{R}} \min_{u\in\mathbb{P}_\tau} \quad \frac{1}{\tau}\int_0^\tau z^\intercal \Upsilon z dt, \qquad z := F(s)\begin{bmatrix} x \\ u \end{bmatrix}, \tag{2.8}$$

$$\text{subject to} \quad \frac{1}{\tau}\int_0^\tau v\, dt = v_o, \tag{2.9}$$

$$\frac{1}{\tau}\int_0^\tau y\, dt = y_o, \qquad y := \mathcal{C}x, \tag{2.10}$$

where we assume that system (2.7) admits a τ-periodic solution (x, v) in response to τ-periodic input u. The optimal periodic control input $u \in \mathbb{P}_\tau$ and its period $\tau > 0$ are to be found, where $\mathbb{P}_\tau$ is the set of possibly vector-valued τ-periodic signals. The objective

function is the average value of a quadratic form $z^\mathsf{T}\Upsilon z$, where Υ is a constant symmetric matrix, and $z \in \mathbb{P}_\tau$ is a selected performance output specified by filtering $\varsigma := \mathrm{col}(x, u) \in \mathbb{P}_\tau$ through a transfer function $F(s)$. Note that $z = F(s)\varsigma$ under an appropriately chosen initial condition that makes the output τ-periodic without transient. The constraints are imposed on the average values of v and y with desired values v_o and y_o. Here, we let $y := \mathrm{col}(\varpi, \delta)$ be the constrained output with target value $y_o := \mathrm{col}(\varpi_o, \delta_o)$, and choose $\mathcal{C}$ accordingly. A typical value of target normal velocity is zero ($\delta_o = 0$), although we allow nonzero values.

The objective function in (2.8), which is quadratic in variable $\varsigma := \mathrm{col}(x, u)$, is defined in terms of $F(s)$ and Υ. For technical simplicity, we assume that these filter and weight are chosen such that the bias term $\bar{\varsigma} := \frac{1}{\tau}\int_0^\tau \varsigma\, dt$ has no contribution to the value of the objective function. It can readily be verified that the assumption is satisfied if and only if $\bar{\varsigma}^\mathsf{T}\Pi(0)\bar{\varsigma} = 0$ holds for the frequency weight $\Pi(j\omega) := F(j\omega)^*\Upsilon F(j\omega)$. Even with this assumption, (2.8) captures useful cost functions through appropriate choices of $F(s)$ and Υ. Table 2.1 gives examples of such objective integrands that are practically important, together with the corresponding frequency weights $\Pi(j\omega)$, where U and W are defined such that $\dot{\zeta} := \mathrm{col}(\varpi, \dot{\varphi}) = U^\mathsf{T}x$ and $\dot{\varphi} = W^\mathsf{T}x$. The input power and shape derivative have nonzero $\Pi(0)$, but it can be verified that $\bar{\varsigma}^\mathsf{T}\Pi(0)\bar{\varsigma}$ is zero by noting that the bias of $\dot{\varphi}$ is zero. Other costs can also be defined with possibly discontinuous function $\Pi(j\omega)$. For instance, if velocity ripples are undesired, the oscillation amplitudes of ϖ and δ can be penalized by choosing $\Pi(j\omega) = \mathrm{diag}(\mathcal{C}^\mathsf{T}\mathcal{C}, 0)$ for $\omega \neq 0$ and $\Pi(0) = 0$. Finally, a cost can be given as a linear combination of various costs.

2.3.2 Problem Reformulation Using Phasors

Solving the optimal gait problem in (2.8)-(2.10) for a globally optimal solution is difficult. For tractability, we reformulate the problem assuming small body deformation φ and truncating its higher order terms.

Table 2.1: Objective Functions

Quantity	Objective Function	$\Pi(j\omega)$
Input Power	$\frac{1}{\tau}\int_0^\tau \dot{\zeta}^\intercal B u\, dt$	$\frac{1}{2}\begin{bmatrix} 0 & UB \\ B^\intercal U^\intercal & 0 \end{bmatrix}$
Input Torque Rate	$\frac{1}{\tau}\int_0^\tau \|\|\dot{u}\|\|^2 dt$	$\begin{bmatrix} 0 & 0 \\ 0 & \omega^2 I \end{bmatrix}$
Shape Derivative	$\frac{1}{\tau}\int_0^\tau \|\|\dot{\varphi}\|\|^2 dt$	$\begin{bmatrix} WW^\intercal & 0 \\ 0 & 0 \end{bmatrix}$

Let us start by introducing some notation and providing a brief review of mathematical preliminaries. A periodic signal $u \in \mathbb{P}_\tau$ can be approximated by its Fourier series

$$u(t) = \bar{u} + \sum_{k=1}^{h} \Re[\hat{u}_k e^{j\omega k t}], \tag{2.11}$$

where $h \in \mathbb{Z}$ can be arbitrarily large, $\omega := 2\pi/\tau$ is the fundamental frequency, $\bar{u} \in \mathbb{R}^r$ is the bias, and $\hat{u}_k \in \mathbb{C}^r$ is the phasor for the k^{th} harmonic term. We denote the phasor of u as $\hat{u} := \mathrm{col}(\hat{u}_1, \ldots, \hat{u}_h)$. For a transfer function $F(s)$, we define

$$F_\omega^h := \mathrm{diag}(F(j\omega), F(j2\omega), \ldots, F(jh\omega)). \tag{2.12}$$

The notations $\bar{u}$, $\hat{u}$, and F_ω^h will be used for generic periodic signals and transfer functions. The following result is elementary and can be proven by straightforward calculations (hence a proof is omitted).

Lemma 1. *Let periodic signals $z, \varsigma \in \mathbb{P}_\tau$ and a transfer function $F(s)$ be given. Then*

$$z = F(s)\varsigma \qquad \Rightarrow \qquad \bar{z} = F(0)\bar{\varsigma}, \qquad \hat{z} = F_\omega^h \hat{\varsigma}.$$

For signals $x, y \in \mathbb{P}_\tau$ of the form (2.11), we have

$$\frac{1}{\tau}\int_0^\tau x(t)^\intercal y(t)\, dt = \bar{x}^\intercal \bar{y} + \frac{1}{2}\sum_{k=1}^{h} \Re[\hat{x}_k^* \hat{y}_k].$$

We now reformulate the optimal gait problem. One factor that makes the problem difficult is the ripples in the locomotion velocity; if $v(t)$ were constant, the analysis would

be easier. We realize this ideal situation by adding a fictitious force $\varepsilon(t)$, with zero average, to the right hand side of the $\dot{v}$ equation in (2.7). Consider the situation where τ-periodic inputs $u, \varepsilon \in \mathbb{P}_\tau$ for (2.7), with $\varepsilon(t)$ specifically chosen to regulate the swim speed $v(t)$, result in constant locomotion velocity $v(t) \equiv v_o$ and τ-periodic response $x(t)$. Approximate $u, x \in \mathbb{P}_\tau$ by truncations of the Fourier series as in (2.11) for a chosen $h \in \mathbb{Z}$. Assume that the bias term $\bar{\varphi}$ and all the harmonic terms $\hat{x}$ are small and of order ϵ, and neglect the $\mathcal{O}(\epsilon^2)$ and $\mathcal{O}(\epsilon^3)$ terms, respectively, in the $\dot{x}$ and $\dot{v}$ equations in (2.7). We equate the periodic terms in the first equation of (2.7) to obtain

$$\hat{x}_k = M(jk\omega)\hat{u}_k, \qquad M(s) := \Big(sI - \tilde{\mathcal{A}}(\varpi_o, v_o)\Big)^{-1}\mathcal{B},$$

where $\tilde{\mathcal{A}}$ is defined to be identical to $\mathcal{A}$ except that the linear terms of ϖ in the first three columns are multiplied by two. The bias terms in the first equation of (2.7) give

$$\bar{x} = H\bar{u}, \qquad H := -\mathcal{A}(\varpi_o, v_o)^{-1}\mathcal{B}.$$

Using the above expression, the angular and normal velocity constraint in (2.10) can be rewritten as

$$\mathcal{H}\bar{u} = y_o, \qquad \mathcal{H} := \mathcal{C}H, \tag{2.13}$$

Since we assumed a fictitious force ε, with zero average, is applied to keep $v \equiv v_o$, the average of the velocity equation in (2.7) over one cycle should also be zero. Averaging (2.7), we replace the velocity constraint integral in (2.9) by

$$\frac{1}{\tau}\int_0^\tau \Big((\mathfrak{b}^\intercal x - \mathfrak{a})v_o + x^\intercal \mathcal{S}(\varpi, v_o)x\Big)dt = 0, \tag{2.14}$$

yielding the thrust-drag balance at $v(t) \equiv v_o$ with no fictitious forcing on average. The integral in (2.14) can be converted to a quadratic constraint in $\bar{u}$ and $\hat{u}$ using Lemma 1 as follows:

$$\hat{u}^* Y_\omega^h \hat{u} - \breve{u}^\intercal Z \breve{u} = 1,$$

where $\breve{u} := \mathrm{col}(\bar{u}, 1)$ and

$$\begin{aligned} &Y(j\omega) := M(j\omega)^* \mathcal{S}(\varpi_o, v_o) M(j\omega)/(2\mathfrak{a}v_o), \\ &Z := -\begin{bmatrix} \nabla & \mathfrak{d} \\ \mathfrak{d}^\intercal & 0 \end{bmatrix}, \qquad \begin{aligned} &\mathfrak{d} := H^\intercal \mathfrak{b}/(2\mathfrak{a}), \\ &\nabla := H^\intercal \mathcal{S}(\varpi_o, v_o)H/(\mathfrak{a}v_o). \end{aligned} \end{aligned} \tag{2.15}$$

Similarly, the objective integral in (2.8) can equivalently be written by $\hat{u}^* X_\omega^h \hat{u}$, where

$$X(j\omega) := \frac{1}{2} \begin{bmatrix} M(j\omega) \\ I \end{bmatrix}^* \Pi(j\omega) \begin{bmatrix} M(j\omega) \\ I \end{bmatrix}. \tag{2.16}$$

In summary, the original optimal gait problem formulated in (2.8)-(2.10) is approximated by the following quadratic optimization problem:

$$\min_{\omega \in \mathbb{R}} \min_{\substack{\hat{u} \in \mathbb{C}^{rh} \\ \bar{u} \in \mathbb{R}^r}} \hat{u}^* X_\omega^h \hat{u} \qquad \text{s.t.} \quad \begin{array}{l} \hat{u}^* Y_\omega^h \hat{u} = 1 + \breve{u}^\intercal Z \breve{u}, \\ \mathcal{H} \bar{u} = y_o, \end{array} \tag{2.17}$$

which is to be solved for the control bias $\breve{u} := \mathrm{col}(\bar{u}, 1)$ and the control phasor $\hat{u}$.

Since the cost or performance function is generally chosen to represent a physical quantity such as energy cost or a vector norm, it is a valid assumption for the cost to be positive. Due to the environmental drag $\mathfrak{a} > 0$, coasting without deceleration is impossible, and there will always be a nonzero cost for any locomotion at nonzero (linear or angular) velocity. Thus we impose the following.

Assumption 1. *Consider the optimization problem in (2.17). The constraints are feasible, and the value of the objective function is positive on the feasible set for any nonzero v_o or ϖ_o and for any $\mathfrak{a} > 0$.*

The assumed property turns out to have favorable implications to tractability of the optimization problem as shown in the next section.

2.3.3 Optimal Turning Gait

The optimal gait problem for locomotion along a straight line is a special case of (2.17), and has been solved in [21]. However, the additional turning rate constraint makes it more difficult. For straight locomotion without turning ($y_o = 0$), zero bias $\bar{u} = 0$ satisfies the second constraint in (2.17) making $\breve{u}^\intercal Z \breve{u} = 0$, and problem (2.17) reduces to

$$\min_{\omega \in \mathbb{R}} \min_{\hat{u} \in \mathbb{C}^{rh}} \hat{u}^* X_\omega^h \hat{u} \qquad \text{s.t.} \quad \hat{u}^* Y_\omega^h \hat{u} = 1. \tag{2.18}$$

While this problem is nonconvex since matrices X_ω^h and Y_ω^h are generally indefinite, [21] has shown that the problem can be equivalently converted to a generalized eigenvalue computation using the S-procedure [52]. For the turning locomotion, however, there are two equality constraints on mixed real ($\bar{u}$) and complex ($\hat{u}$) variables , and direct application of the S-procedure is conservative (inaccurate). One could eliminate the linear equality constraint by solving it for $\bar{u}$, but we take a different approach to gain insights into the turning problem.

Our approach is to reduce the problem to two tractable problems by proving a separation principle under the property in Assumption 1. First note that the cost $\hat{u}^* X_\omega^h \hat{u}$ is small if the oscillation amplitude $\|\hat{u}\|$ is small. The thrust-drag balance, i.e. the first constraint in (2.17), indicates that $\|\hat{u}\|$ is smaller if $\breve{u}^\mathsf{T} Z \breve{u}$ is smaller. Hence, the term $\breve{u}^\mathsf{T} Z \breve{u}$ can be thought of as the cost associated with turning. Indeed, this term is nonnegative as shown below.

Lemma 2. *Suppose Assumption 1 holds. Then*

$$\breve{u} = col(\bar{u}, 1), \qquad \mathcal{H}\bar{u} = y_o \qquad \Rightarrow \qquad \breve{u}^\mathsf{T} Z \breve{u} \geq 0. \tag{2.19}$$

Proof. Suppose condition (2.19) does not hold. Then there is a $\bar{u}$ such that $\mathcal{H}\bar{u} = y_o$ but $\breve{u}^\mathsf{T} Z \breve{u} < 0$. Since Z is proportional to $1/\mathfrak{a}$, an appropriate scaling of $\mathfrak{a}$ can make $1 + \breve{u}^\mathsf{T} Z \breve{u} = 0$. For this value of $\mathfrak{a}$, $\hat{u} = 0$ is a feasible control input that satisfies constraint (2.17), and makes the cost $\hat{u}^* X_\omega^h \hat{u} = 0$. Since this contradicts the original assumption, condition (2.19) must hold. □

Thus, the minimum value of $\breve{u}^\mathsf{T} Z \breve{u}$ is zero and is achieved when the input bias $\bar{u}$ is set to zero for straight locomotion ($y_o = 0$) as in [21]. For general turning locomotion ($y_o \neq 0$), we may minimize the turning cost $\breve{u}^\mathsf{T} Z \breve{u}$ separately by choosing $\bar{u}$. This idea is formally justified as follows.

Lemma 3. *Consider problem (2.17) and*

$$\min_{\omega \in \mathbb{R}} \min_{\hat{u} \in \mathbb{C}^{rh}} \quad \hat{u}^* X_\omega^h \hat{u} \qquad s.t. \quad \hat{u}^* R_\omega^h \hat{u} = 1, \tag{2.20a}$$

$$\mu := \min_{\bar{u} \in \mathbb{R}^r} \breve{u}^\mathsf{T} Z \breve{u} \qquad s.t. \quad \mathcal{H}\bar{u} = y_o, \tag{2.20b}$$

where

$$R(j\omega) := Y(j\omega)/(1+\mu), \qquad \breve{u} := col(\bar{u}, 1).$$

Suppose Assumption 1 holds. Then, problem (2.20) and problem (2.17) are equivalent in the sense that they have the equal value of the optimal cost function and the same optimizer solution.

Proof. It suffices to show that problems (2.17) and (2.20), excluding the minimization over ω, are equivalent for each fixed ω. Let γ_1 be the optimal value of the cost function in (2.17) with optimizer $(\bar{u}_1, \hat{u}_1)$, let γ_2 be the optimal value of the cost in (2.20a) with optimizer $\hat{u}_2$, and let $\bar{u}_2$ be an optimizer for (2.20b). Define

$$\begin{aligned} \alpha_i &:= 1 + \breve{u}_i^{\mathsf{T}} Z \breve{u}_i, & \breve{u}_i &:= \mathrm{col}(\bar{u}_i, 1), \\ \mathsf{R}_i &:= Y_\omega^h / \alpha_i, & \hat{u}_o &:= \sqrt{(\alpha_2/\alpha_1)}\hat{u}_1, \end{aligned}$$

for $i = 1, 2$. Because (2.19) holds, α_i is always positive, and by definition, $\mathsf{R}_2 = R_\omega^h$. We will show that problems (2.17) and (2.20) are equivalent by showing $\gamma_1 \leq \gamma_2$ and $\gamma_2 \leq \gamma_1$.

The proof for $\gamma_1 \leq \gamma_2$ is simple. Because $\hat{u}_2^* Y_\omega^h \hat{u}_2 = 1 + \mu$ where $\mu = \breve{u}_2^{\mathsf{T}} Z \breve{u}_2$, the parameter $(\bar{u}_2, \hat{u}_2)$ satisfies both constraints in problem (2.17) and is a possible solution to (2.17). However, since γ_1 is the optimal solution to (2.17), it follows that $\gamma_1 \leq \hat{u}_2^* X_\omega^h \hat{u}_2 = \gamma_2$. To show the other direction, note that the optimizer $(\bar{u}_1, \hat{u}_1)$ satisfies the constraints in (2.17), and hence $\hat{u}_1^* \mathsf{R}_1 \hat{u}_1 = 1$. We then see that $\hat{u}_o^* \mathsf{R}_2 \hat{u}_o = \hat{u}_1^* \mathsf{R}_1 \hat{u}_1 = 1$, so that $\hat{u}_o$ satisfies the constraint in (2.20a). It now follows that

$$\gamma_2 \leq \hat{u}_o^* X_\omega^h \hat{u}_o = (\alpha_2/\alpha_1) \hat{u}_1^* X_\omega^h \hat{u}_1 \leq \gamma_1,$$

where the first inequality holds because γ_2 is the optimal solution to (2.20a), and the second inequality holds since $\bar{u}_2$ is the optimal solution to (2.20b) and therefore $\alpha_2 \leq \alpha_1$. This completes the proof. □

Lemma 3 proves that the optimization problem in (2.17) can be reduced, equivalently, to two minimization problems, where the optimal bias term is found *separately* from the optimal periodic component. The physical interpretation of (2.20b) is the minimization of

the environmental drag due to the bias $\bar{u}$, given by $\breve{u}^\intercal Z \breve{u}$, with the achievement of the desired turning rate ϖ_o. Equivalently, it can be seen as finding the optimal nominal body shape of the rectifier to reduce the environmental drag effect. According to Lemma 3, the optimal bias offset is independent of the effects of the periodic component or even the choice of cost functions. On the other hand, (2.20a) has the same form as (2.18), and is essentially the optimal straight locomotion problem with the modification of the velocity constraint, which compensates for the drag effect μ due to the turning component.

The phasor optimization problem in (2.20a) can be solved using a previous result for straight locomotion (Lemmas 2 and 3 in [21]). The result shows that the optimal value of the cost $\hat{u}^* X_\omega^h \hat{u}$ is independent of h, meaning that the optimum can always be achieved by a purely sinusoidal input and no further reduction of the cost is possible by a general periodic input. The optimal cost can be found from the generalized eigenvalues of the pair $(X(j\omega), R(j\omega))$ with a line search over ω, and the phasor of the optimal input is given as the corresponding eigenvector.

For the bias optimization problem in (2.20b), $\breve{u}^\intercal Z \breve{u}$ is an indefinite quadratic form, and hence is not convex. However, it turns out that the objective function is convex on the feasible set under Assumption 1. Therefore, the problem has only one local minimum, and the global minimizer can be found by a local algorithm or convex programming. In fact, the problem admits a closed form solution of the global minimizer as follows.

Lemma 4. *Consider the problem (2.20b). Suppose the problem is feasible and condition (2.19) holds. Then an optimizer is given by*

$$\bar{u}_\flat = \bar{u}_o - N(N^\intercal \nabla N)^\dagger N^\intercal (\nabla \bar{u}_o + \mathbf{d}), \tag{2.21}$$

where $(\cdot)^\dagger$ *denotes the Moore-Penrose inverse, and*

$$N := I - \mathcal{H}^\dagger \mathcal{H}, \qquad \bar{u}_o = \mathcal{H}^\dagger y_o.$$

Proof. The result follows from a standard linear algebra result [53]. □

We can now summarize the main result. Consider the optimal turning gait problem given by (2.8)-(2.10) for the mechanical rectifier in (2.7) with desired locomotion speed v_o,

turning rate ϖ_o, and cost weights Υ and $F(s)$. Suppose the objective function value is zero when u and x are constant solutions of (2.7). Then, based on the reformulation procedure in Section 2.3.2, the problem reduces, approximately, to the quadratic optimization given by (2.17), where matrices $X(\omega)$, $Y(\omega)$, Z, and $\mathcal{H}$ are defined in (2.15), (2.16), and (2.13). The optimizers of the two problems are related by (2.11). The globally optimal solution to (2.17) is given by the following result.

Theorem 1. *Consider the optimal turning gait problem given by (2.17). Suppose Assumption 1 holds. Then the optimal bias $\bar{u}_\flat$ is given by (2.21), and optimal phasor $\hat{u}_\flat$ and frequency $\omega_\flat$ can be found as follows. For each $\omega > 0$, define*

$$R(\omega) := Y(\omega)/(1 + \breve{u}_\flat^T Z \breve{u}_\flat), \qquad \breve{u}_\flat := col(\bar{u}_\flat, 1),$$

and let λ_ω be the largest real generalized eigenvalue of the pair $(X(\omega), R(\omega))$ that satisfies the condition $X(\omega) \geq \lambda_\omega R(\omega)$. Let $\hat{u}_\omega$ be the eigenvector corresponding to λ_ω, normalized such that $\hat{u}_\omega^* R(\omega) \hat{u}_\omega = 1$. The optimal frequency $\omega_\flat$ is given by ω that minimizes λ_ω, and the optimal phasor $\hat{u}_\flat$ is the corresponding eigenvector $\hat{u}_{\omega_\flat}$.

Proof. Problem (2.17) can be equivalently split into the bias and harmonics (phasor) optimizations in (2.20) as shown in Lemma 3. The optimal bias $\bar{u}_\flat$ is given by Lemma 4, and the optimal phasor $\hat{u}_\flat$ is obtained from the result in [21] as described. □

Theorem 1 states that the optimal control input for the original problem (2.8)–(2.10) can be approximately given by the exact solution $u_\flat(t)$ to the reformulated problem (2.17). The optimal solution $u_\flat(t)$ is purely sinusoidal and has the form

$$u_\flat(t) = \bar{u}_\flat + \Re[\hat{u}_\flat e^{j\omega_\flat t}],$$

where $\bar{u}_\flat$ and $\hat{u}_\flat$ are found by an explicit formula and eigenvalue computation. The optimal frequency $\omega_\flat$ can be found through a line search by gridding the frequency axis and plotting the optimal cost value λ_ω as a function of ω. The optimal gait, or body shape $\varphi_\flat(t)$ corresponding to $u_\flat(t)$, is also sinusoidal and its bias $\bar{\varphi}_\flat$ and phasor $\hat{\varphi}_\flat$ are found by computing $(\bar{x}_\flat, \hat{x}_\flat)$ using the equations following (2.11). Note that the optimal bias shape $\bar{\varphi}_\flat$ is independent of the cost function.

2.4 Numerical Example: The H-Swimmer

This section demonstrates the utility of the optimal turning gait problem formulation and solution through numerical examples of an arbitrary locomotor swimming in water. The mechanical rectifier is H-shaped, and is composed of a main body (54.5×9.1 mm, 0.33 g) with six degrees of freedom of translation and rotation, and twenty identical panels (9.1×9.1 mm, 0.083 g each) connected at rotational joints, each with one degree of freedom for a total of $n = 26$ degrees of freedom (Fig. 2.2). Half of the panels are located in front of the main body, divided between right and left sides (arms), and can rotate along the pitch direction, and half of the panels are located behind the main body, divided between right and left sides (legs), and can rotate along the yaw direction. The rectifier's total length along the y-axis is 100 mm, and its width along the x-axis is 54.5 mm. It is placed in a fluid environment, subject to hydrodynamic forces and torques that interact with the body motion to produce thrust for locomotion. The hydrodynamic forces acting on each panel are approximated by linear functions of the relative velocities of the respective segments; $f_{n_i} = c_{n_i} v_{n_i}$ and $f_{t_i} = c_{t_i} v_{t_i}$ in the normal and tangential directions, where $(c_{n_i}, c_{t_i}) = (41, 0.62)$ mN·s/m for the small panels and $(c_n, c_t) = (60, 0.88)$ mN·s/m for the main body. All the model parameter values are set for physical plausibility from experimental data of leech swimming [50].

The body frame is attached to the main body as shown in Fig. 2.2, and its Euler angles $\psi \in \mathbb{R}^3$ and angular velocity $\varpi \in \mathbb{R}^3$ represent the orientation and turning rate of the rectifier. The joint angles $\phi \in \mathbb{R}^{20}$ specify the body shape, and are defined so that $\phi = 0$ when the

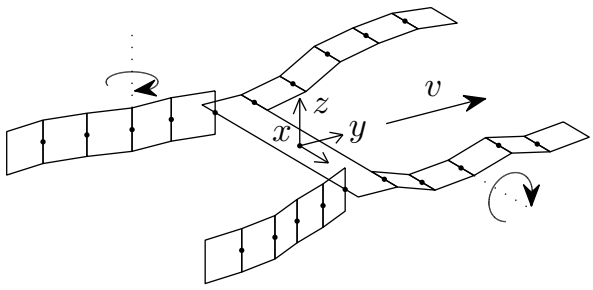

Figure 2.2: Swimming locomotor model consisting of $\kappa = 21$ bodies and $n = 26$ degrees of freedom

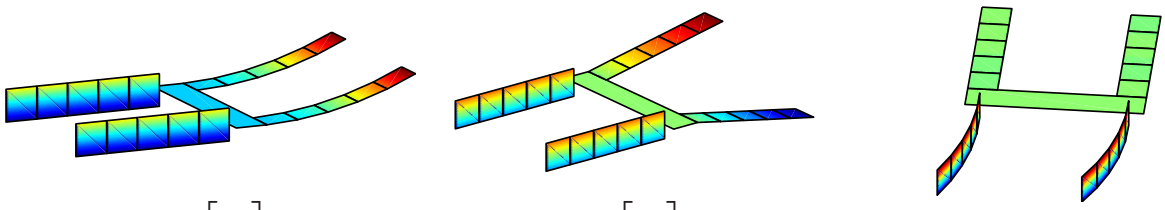

(a) Pitch, $\varpi_o = \begin{bmatrix} 0.8 \\ 0 \\ 0 \end{bmatrix}$ (b) Roll, $\varpi_o = \begin{bmatrix} 0 \\ 0.8 \\ 0 \end{bmatrix}$ (c) Yaw, $\varpi_o = \begin{bmatrix} 0 \\ 0 \\ 0.8 \end{bmatrix}$

Figure 2.3: Optimal shape with only bias of the joint angles $\bar{\varphi}_\flat$, around which the body oscillates

arms and legs are stretched along the y-axis. Each joint is actuated by a torque input, such that $u(t) \in \mathbb{R}^{20}$, and the adjoining panels are connected by linear bending stiffnesses 3×10^{-4} Nm/rad. Finally, the nominal shape is set to be straight ($\eta = 0$), where the flexible joints are at rest.

This particular locomotor design serves two features. The first is that it is not replicating any particular underwater animal that could give us a reasonable gait without using optimal gait analysis. The second feature is that it allows for torque production in any direction of rotation such that a bias shape $\bar{\varphi}$ exists for any feasible value of the desired angular velocity ϖ_o. This can be better understood by Fig. 2.3, which shows the optimal bias shapes for basic pitch, roll, and yaw rotations calculated from (2.21). Pure pitch rotation is achieved by a body shape with left-right symmetry where the arms are curled up along the radius of rotation. Similarly, pure yaw rotation is achieved by the legs curving along the radius of rotation about the z-axis. Pure roll rotation, however, requires asymmetry in the body where one arm pushes the fluid upward and the other arm pushes the fluid downward.

We find the optimal torque input, optimal frequency, and optimal body shape for the three cost functions provided in Table 2.1 subject to an average locomotion velocity of $v_o = 100$ mm/s, an average angular velocity of $\varpi_o = \text{col}(75, 75, 400)$ rad/ks, and average $\delta_o = \text{col}(0, 0)$ mm/s. Table 2.2 gives the optimal frequencies and the average values of the steady state velocities obtained by simulating the simplified model (2.7). The optimal frequencies for

the three cost functions range between 2 Hz to 4 Hz. The results show that average velocities close to the desired values are achieved for shape-derivative and torque-rate optimizations; however, there are some large errors in the simulated velocities for power optimization. These errors are due to the large harmonics of the angular velocity $\hat{\varpi}$ that violate the assumption that $\hat{\varpi}$ is of order ϵ. The errors can be reduced, if desired, by penalizing a linear combination of power and angular velocity oscillations.

Minimization of each cost function leads to a distinct gait whose optimality is not obvious from physical intuition. Snapshots of these optimal gaits over one period are shown in Figs. 2.4-2.6. Thrust generation in the power optimal gait is achieved by the arms sending asymmetrical waves down the right and left sides of the body, while the legs oscillate from side to side with small amplitudes (Fig. 2.4). The oscillation amplitudes are larger on the left hand side to achieve the desired turning. This asymmetrical gait has a lower power cost than a gait with symmetrical waves traveling down the right and left sides of the locomotor. The shape-derivative cost is minimized when the legs use a flapping motion to propel the locomotor forward, similar to the gait in jellyfish swimming (Fig. 2.5). This gait is desirable because it minimizes large changes in the body shape and allows the main body to remain steady without large oscillations about its orientation. However, it comes at a price of very large torque and power costs. In the optimal torque-rate gait, the legs synchronously oscillate from side to side at a relatively high frequency, similar to the motion of caudal fins in fish (Fig. 2.6). This gait saves input torque magnitude, but sacrifices large body shape changes and yawing motion.

Figures 2.4-2.6 show that it is optimal to use either arms or legs to generate thrust for locomotion, but it is not desirable to combine all four limb movements. This is a counterintuitive result (valid at least for the simplified model) that one would not be able to predict without using the optimal gait theory. Furthermore, the left-right asymmetry in the optimal gaits resulting from turning requirement, which is most prevalent in power optimization, demonstrates the following point. Although the harmonic term of the body shape is found by solving a problem of the same form as the straight locomotion problem, the oscillatory component of the optimal gait is still a function of the desired angular velocity due to the

dependence of $X(\omega)$ and $Y(\omega)$ on ϖ_o.

Table 2.2: Target values, optimal frequencies, and simulated velocities of the simplified model (2.7)

objective	$\omega_\flat$ [Hz]	v [mm/s]	δ [mm/s]	ϖ [rad/ks]
(Target Value)	—	100	$\begin{bmatrix} 0 \\ 0 \end{bmatrix}$	$\begin{bmatrix} 75 \\ 75 \\ 400 \end{bmatrix}$
Power	2.00	101.0	$\begin{bmatrix} -1.7 \\ -0.1 \end{bmatrix}$	$\begin{bmatrix} 100 \\ 85 \\ 499 \end{bmatrix}$
Shape	2.26	99.5	$\begin{bmatrix} -0.2 \\ 0.0 \end{bmatrix}$	$\begin{bmatrix} 75 \\ 75 \\ 413 \end{bmatrix}$
Torque	3.66	98.8	$\begin{bmatrix} -1.8 \\ 0.0 \end{bmatrix}$	$\begin{bmatrix} 73 \\ 69 \\ 394 \end{bmatrix}$

Table 2.3: Simulated velocities of the original model (2.5)

objective	v [mm/s]	δ [mm/s]	ϖ [rad/ks]
Power	87.2	$\begin{bmatrix} 0.2 \\ 1.9 \end{bmatrix}$	$\begin{bmatrix} 84 \\ 60 \\ 312 \end{bmatrix}$
Shape	95.7	$\begin{bmatrix} -0.1 \\ -2.4 \end{bmatrix}$	$\begin{bmatrix} 74 \\ 64 \\ 518 \end{bmatrix}$
Torque	107.2	$\begin{bmatrix} -0.8 \\ -3.2 \end{bmatrix}$	$\begin{bmatrix} 114 \\ 75 \\ 499 \end{bmatrix}$

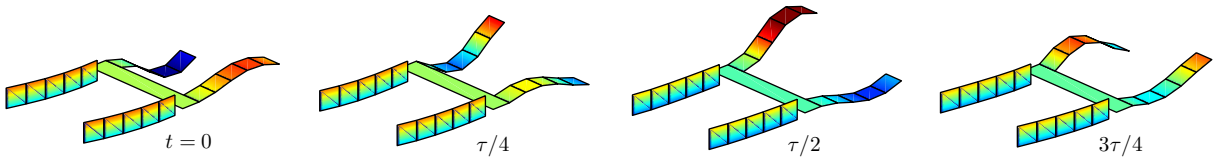

Figure 2.4: Snapshots of the power optimal gait

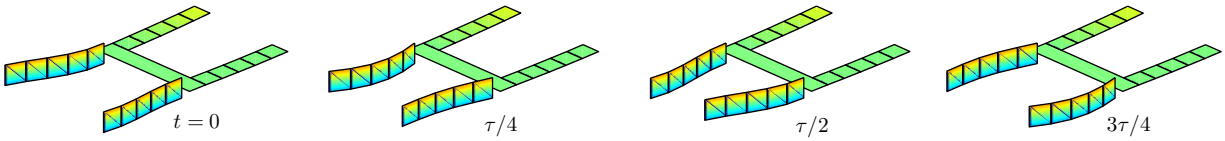

Figure 2.5: Snapshots of the shape-rate optimal gait

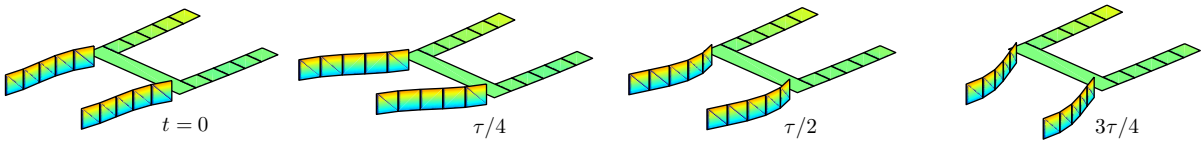

Figure 2.6: Snapshots of the torque-rate optimal gait

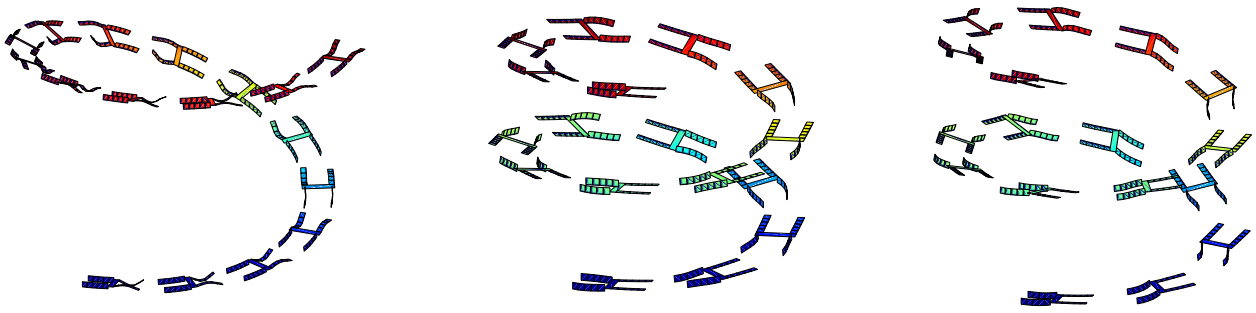

(a) Power (b) Shape (c) Torque

Figure 2.7: Nonlinear model trajectory over 25 seconds

In order to analyze the accuracy of the optimal gait result from the simplified model (2.7), we look at the simulated velocities of the original nonlinear model (2.5) given in Table 2.3. The different gaits result in different accuracies depending on how well they satisfy the assumptions on small body deformation and small angular velocity harmonics. In torque-rate optimization, in particular, the pitch rate is much larger than desired. This occurs because the gait in torque-rate optimality has large roll rate harmonics due to the motion of the back panels pushing the main body from side to side, thereby violating the assumption that $\hat{\omega}$ is of order ϵ. The roll rate harmonics can be reduced by actuating the rectifier at a higher oscillation frequency with smaller amplitudes, thereby achieving simulated velocities that are closer to the desired values.

Figure 2.7 shows snapshots of the trajectories for the original nonlinear model (2.5) over 25 seconds. The slower nominal speed and smaller yaw rate in power optimization results in a trajectory with a larger radius of rotation and a larger bank angle. The larger yaw rate and smaller roll rate in shape-derivative optimization results in a smaller radius of rotation and a tighter distance between the turns. The larger locomotion speed and pitch rate in torque-rate optimization results in the locomotor traveling at a faster pace with a larger bank angle. Despite the discrepancies between the simulated velocities, all the trajectories follow the desired path at least qualitatively, demonstrating the utility of the optimal turning gait formulation and solution for robotic locomotor designs. Although optimality of the simplified model does not guarantee global optimality for the original nonlinear model, the optimal gait

found can be used as an initial condition to find optimal gaits for the fully nonlinear model.

2.5 Discussion

Analytical studies of (animal or robotic) locomotion systems require dynamic models of the body-environment interactions. While most of the past modeling efforts have addressed specific locomotor configurations, it is desired to have a "paradigm model" for a class of locomotors, upon which a general theory of locomotion can be developed. A successful paradigm model, based on geometric mechanisms, exists [54, 14, 13, 55], which encompasses modeling/analysis of locomotors interacting with environment through kinematic (nonholonomic) constraints (rolling wheels, momentum preservation, etc.). This paradigm does not capture locomotors interacting with the environment through resistive forces resulting from relative body motion (swimming, slithering) under nontrivial inertia effects. The dynamical models we developed in Section 2.2 capture this class of locomotors, providing a basis for further analytical studies.

In general, robotic locomotors are subject to many uncertainties embedded in various features, and their accurate modeling is infeasible. Hence, a good practice in robotic control design or motion planning, in our opinion, is to analyze a simple model capturing the essential dynamics and develop a rough plan for operation, followed by fine tuning on site through experiments. With this scenario in mind, we have derived the equations of motion (2.5) for a general class of mechanical rectifiers traveling in three dimensional space with full rotation and translation. The resistive nature of the body-environment interactions is qualitatively captured by forces linearly dependent on the relative velocities, with drag coefficients quantitatively dictating the net effect over a cycle of body oscillation. We then reduced the model to the simplest form (2.7) that maintained the necessary rectifying dynamics, assuming small body deformation. The state space model (2.7) unveils the dynamical structure of mechanical rectifiers, explicitly showing how variables are interlaced to produce thrust for propulsion and moment for turning. Our simple analytical model is not only applicable for numerical simulations, but also for theoretical study.

We then formulated an optimal turning gait problem as the minimization of a quadratic cost function subject to constraints on the average locomotion velocity and angular velocity. Physical properties (Assumption 1) were exploited to reduce the optimality problem equivalently to two separate minimization problems, solvable for globally optimal solutions. It was proven that the optimal offset resulting in turning is first found independently of the periodic term resulting in translation, while the optimal periodic term is adjusted to compensate for the environmental drag due to the shape offset. Furthermore, it was shown that, like optimal locomotion in a fixed direction, the optimal periodic term is purely sinusoidal.

To confirm the utility of the optimal gait problem and solution, numerical examples of a swimming locomotor were presented. The examples showed that while the optimality problem is formulated and solved for a simplified model, the optimal gaits are reasonable for the original nonlinear model even when the assumptions of small body deformation are slightly violated. The results showed the benefits of the optimal gait theory in finding optimal gaits that can achieve a desired trajectory and speed.

The theoretical framework developed through a series of research, including [21] and in this chapter, are useful for understanding biological mechanisms underlying animal locomotion. For instance, in the next chapter, we will demonstrate how modeling and gait analyses within our framework supports the hypotheses that carangiform fish exploit body-fluid resonance for efficient swimming. Another example of this theory supporting animal locomotion includes the two representative gaits of batoids, undulation and oscillation [56], which result from energy optimization under round and triangular shapes of large pectoral fins [57, 58]. In the field of engineering, our framework is useful for proof-of-concept designs of mechanical rectifiers. Our theory can quickly provide a list of reasonable gaits for a creative (not necessarily bio-inspired) design of a robotic locomotor, without any *a priori* knowledge or prejudice from animal locomotion. These innovative designs of locomotors can be achieved through design/analysis iterations to go beyond mimicking what we observe in nature.

CHAPTER 3

Analytical Insights into Optimality and Resonance in Fish Swimming

3.1 Overview

The purpose of this chapter is to demonstrate the utility of the optimal gait theory not only for design, but also as a tool for analyzing biology. We provide simple analytical explanations for why fish choose a specific gait and oscillation frequency when swimming at a steady-state velocity. We first hypothesize that the natural gait is optimal and minimizes a mechanical cost. For instance, the natural gait may be minimizing muscle tension, power consumption, body shape curvature, or a combination thereof. Furthermore, we hypothesize that resonance is exploited in reducing the cost. Because both frequency tuning and hydrodynamic wake resonance have been observed, this resonance likely depends on both body and fluid dynamics. In contrast with previous works that focused on individual aspects of biomechanics and hydrodynamics of swimming, this chapter presents an integrative view of fish swimming mechanisms, based on a simple model of body-fluid dynamics.

The primary analysis focuses on saithe (*pollachius virens*) swimming. Carangiform locomotion of saithe has been studied using Lighthill's slender body theory by [1, 2, 59], which modeled saithe as a continuous dynamic beam under hydrodynamic forces and moments. Here, we develop a discrete model using three rigid bodies with two rotational joints that only permit lateral oscillation. We consider standard form drag on the whole body and added-mass effect on the tail for thrust generation [60, 61, 62] to model the resistive/reactive hydrodynamic forces. To determine whether natural swimming gait is optimal, we compare numerical results from model-based analysis to data from observed swimming. We find op-

timal gaits using the approach developed in [21] and extended in Section 2.3.3, where tail motion is optimized to achieve a given average velocity with minimal mechanical cost. This simple method allows us to develop analytical insights into the connection between optimality and resonance, plus various properties including Strouhal number, power consumption, and Froude efficiency.

3.2 Body-Fluid Interaction Model

Saithe fish exhibit carangiform locomotion, where undulation is concentrated in the posterior half of the body. In our study, we use a simple model with three rigid bodies and two rotational joints (figure 3.1), representing a heavy head and trunk region ("main body") and undulating precaudal and caudal regions ("tail"). The main body of the fish, with the center of mass at (x_o, y_o), is assumed to move only in the x direction, with no rotation or translation in the y direction, such that its motion is solely described by the position x_o and velocity $v := -\dot{x}_o$. This is a reasonable model to study carangiform locomotion along a straight line. Tail motion is described by the angular displacements of the oscillating panels $\theta \in \mathbb{R}^2$ and is generated from the net effects of hydrodynamic forces and muscle bending moments. Although we are only considering a model where the tail section is represented by two panels with two rotating joints, the tail can be similarly divided for an arbitrary dimension of n oscillating panels with analogous analytical results.

The muscle bending moments consist of active and passive components [63]. The active component $u \in \mathbb{R}^2$ results from the difference in antagonistic left/right muscle tensions and is directly controlled through motoneuron activation. The passive component results from co-contraction of left/right muscles plus intrinsic elasticity of the tissues, and is modeled proportional to the curvatures (angular displacements) at the two joints with proportionality constants (stiffnesses) k_1 and k_2. Undulatory motion of fish is driven by anterior muscles in the precaudal region, and the resulting wave is propagated down the tail through the body's passive stiffness [64, 65, 66]. To make our model similar to live fish, we allow the tail to oscillate passively; the active muscle bending moment u_1 is applied only at the anterior joint,

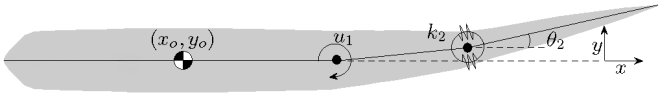

Figure 3.1: Top view of fish model. A large main body is constrained to move along the x-axis, and two oscillating panels represent the flexible tail section.

with the posterior joint assumed passive, i.e. $u_2(t) \equiv 0$, unless otherwise noted. Each rigid body is subject to forces and torques due to the external environment, neglecting gravity and buoyancy. Non-linear equations of motion can be found using torque and force balances or the Euler-Lagrange equation.

In carangiform locomotion, with Reynolds number (Re) between 2×10^5 and 8×10^5 [1], there is little time for resistive forces to build up in the undulating sections of the body, and thrust generation is dominated by reactive forces due to the water inertia. Therefore, we only consider resistive drag acting on the "zeroth" main body constrained to the x-axis and reactive thrust in the tail. The drag force f_o is proportional to the fish's total (main body and tail) wetted surface area A_w and the square of the velocity v, with drag coefficient c_D, which is approximately 0.01 for swimming fish [62]:

$$f_o = cv^2, \qquad c := \frac{1}{2} c_D \rho A_w,$$

where ρ is the water density.

The mean thrust necessary to balance the drag is generated reactively in the undulating sections. In inviscid flow, this reactive force arises from the volume of water accelerated by the panels in the normal direction at each cross section of the body. In this simple body-fluid model, we assume all the thrust is generated at the unconstrained pre-caudal and caudal tail sections; and the added mass of the accelerated fluid adds to the body mass of the fish, to give a total effective mass. In his reactive theory of a slender fish, Lighthill models the fluid acceleration at section i with

$$a_i = \dot{w}_i + \frac{v}{\cos^2 \theta_i} \dot{\theta}_i, \tag{3.1}$$

where w_i is defined as the velocity in the y-direction of a water slice, pushed away by cross section i of the body [60]. Here, we assume the volume of water accelerates in the normal

direction with the body and slides in the tangential direction, such that the after a time δt, the volume of water remains in its x-position, (figure 3.2). This assumption gives a fluid acceleration of

$$a_{n_i} = \alpha_{n_i} - 2\nu_{t_i}\dot{\theta}_i, \tag{3.2}$$

where α_{n_i} and ν_{t_i} are the normal acceleration and tangential velocity of the ith panel respectively [50]. The reactive force f_i is normal to the panel, and its lateral component is proportional to the acceleration and mass of the water slice [67]. Hence, f_i is given by

$$f_i = m_{A_i} a_{n_i},$$
$$m_{A_i} := \rho V_i c_{A_i},$$

where m_{A_i} is the added mass accelerated by the ith body, ρ is the water density, V_i is the cylindrical volume of water, and c_{A_i} is the added mass coefficient that takes into account shape dependence on the acceleration reaction [67]. It can be shown that this reactive force model is equivalent to the spatial discretization of the slender-body theory by Lighthill [60]. The model is also equivalent to the one previously used for anguilliform swimming [50] when both models are linearized using small oscillation angle approximations.

With the model for hydrodynamic forces and torques, nonlinear equations of motion are derived from first principles of physics, such as the Euler-Lagrange equation, as in the previous chapter, in Section 2.2. To gain insights into swimming mechanisms, we simplify the equations of motion to develop bilinear equations of motion using small oscillation angles and Taylor series expansions. Additionally, we consider steady-state swimming at a constant average speed v resulting from τ-periodic body movements θ, and take the average over a cycle τ to remove acceleration. Using these assumptions, we get the following equations of motion:

$$J\ddot{\theta} + 2vG\dot{\theta} + K\theta = Bu, \tag{3.3}$$
$$cv^2 + \overline{\theta^{\intercal} G^{\intercal} \ddot{\theta}} = 0, \tag{3.4}$$

where J, G, K, and B are constant 2×2 matrices representing the moment of inertia of the total effective mass, coefficient for reactive hydrodynamic torque, body stiffness, and

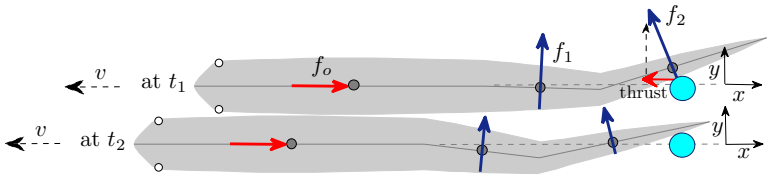

Figure 3.2: Hydrodynamic forces acting on the body model. Two snapshots at different time instants are shown with a lateral offset for clarity. The main body experiences resistive drag force f_o. The tail receives reactive hydrodynamic forces, f_1 and f_2, due to the mass of fluid pushed in the lateral direction of the oscillating body. In steady swimming, the average reactive forces in the x-direction (thrust) balance the resistive drag. Reactive forces in the y-direction would balance the lateral resistive drag on the main body (not shown) if it were not constrained to only move in the x-direction.

transformation from bending moment to inertial torque, respectively. The first equation shows how the muscle bending moment u results in body motion θ, and the second equation shows the force balance where cv^2 represents the total drag and $-\overline{\theta^\intercal G^\intercal \ddot{\theta}}$ the average thrust force over one cycle. Here, the notation $\overline{x}$ for a τ-periodic signal x means the average $\overline{x} := (1/\tau)\int_0^\tau x(t)dt$. Although velocity fluctuations are ignored in the first equation adding limitations to the model, the simplification helps us find important properties in steady swimming otherwise hidden in a complicated mathematical model. A detailed derivation is given in the Appendix.

3.2.1 Model Parameters

We fix model parameters using data on the body dimensions, kinematics, and observed gaits of live saithe provided by [1, 2]. According to the data, a saithe, on average, travels approximately 86% of its body length in one tail-beat cycle. Therefore, a 40 cm saithe swims at approximately 1.2 m/s with a frequency of 3.5 Hz. The body dimensions of saithe and kinematic data, averaged over 13 video sequences, are given in table 3.1. Based on the distribution of amplitude of movement along the body, we approximate the main body to

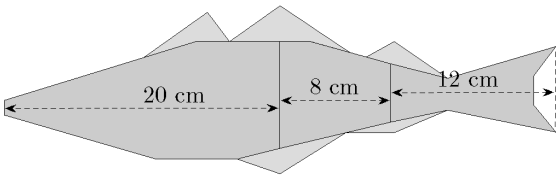

Figure 3.3: Approximated side view of saithe.

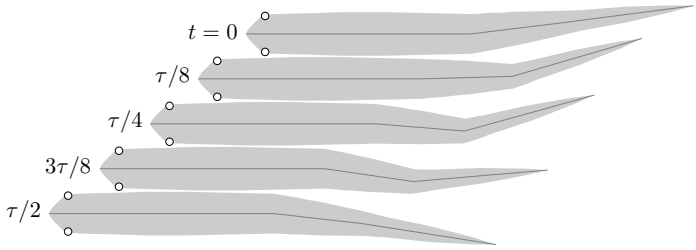

Figure 3.4: Snapshots of observed swimming gait over a half cycle [1], with period τ, during steady-state swimming.

be 50% of the entire length, and approximate the undulating precaudal region and caudal tail fin to be 40% and 60% of the posterior half, respectively. The fish's side view is given in figure 3.3, with body parameters in table 3.2.

Table 3.1: Averaged body dimensions and kinematic data from saithe

total body length	$l_b = 0.40$ m
total body mass	$m = 11.3 l_b^3$ kg/m^3
wetted surface area	$A_w = 0.401\ l_b^2$
tail-beat period	$\tau = 0.278$ s
tail-beat amplitude	$h = 0.083\ l_b$
swimming speed	$v = 0.86\ l_b/\tau$

The saithe's natural gait is described by the distribution of amplitude and phase of movement along the body length. Two observed gaits at two swim speeds are given in [1]. Snapshots of one observed gait, traveling at 1.2 m/s with an oscillating frequency of 3.49 Hz, are shown in figure 3.4, where the tail angles $\theta_{nat}(t)$ were determined by spatial

Table 3.2: Model parameters

	tail panel 1	tail panel 2
length	$2l_1 = 8$ cm	$2l_2 = 12$ cm
height	$d_1 = 6.09$ cm	$d_2 = 3.75$ cm
mass	$m_1 = 177$ g	$m_2 = 67.9$ g
fluid volume/length	$A_1 = 0.0182 l_b^2$	$A_2 = 0.0174 l_b^2$
added-mass coefficient	$c_{A_1} = 1$	$c_{A_2} = 2.53$
drag coefficient	$c_D = 0.009$	
water density	$\rho = 1000$ kg/m^3	

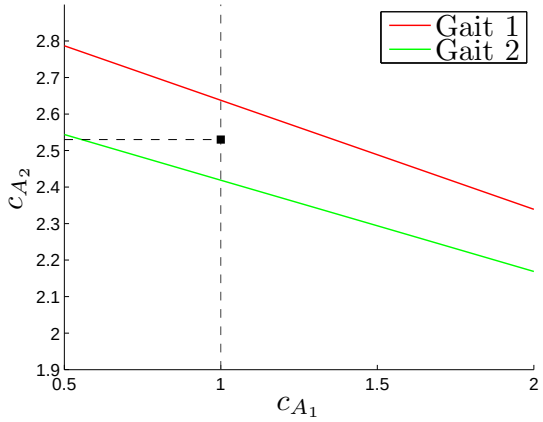

Figure 3.5: Estimation of the added-mass coefficients (virtual mass divided by nominal cylindrical mass) of the two tail links (c_{A_1}, c_{A_2}). For values on the two lines, average thrust and drag forces balance in the two observed gaits provided by [1], resulting in steady swimming. In the analysis, $c_{A_1} = 1$ and the average value of c_{A_2} for the two gaits (marked by a square) are used.

discretization. For a 40 cm fish, the tail-tip amplitude y_{max} is approximately 3.3 cm. We define the nondimensional frequency called the Strouhal number, as $St = fh/v$, where f is the tail-beat frequency in Hertz, and $h = 2y_{max}$ is the peak-to-peak tail-tip amplitude. For an average fast-swimming saithe, the Strouhal number is about 0.20. This value is at the low end of the 0.2-0.4 range observed in fish and cetaceans [68].

The fluid drag depends on the drag coefficient c_D. According to [69], this value is approximately 0.01 for salmon and herring swimming at $Re \sim 10^6$. The averaged drag coefficient calculated from saithe the data in [1] is $c_D \approx 0.009$, and we use this value for our analysis. The thrust generated in the undulating tail sections depends on added-mass coefficients c_{A_1} and c_{A_2}. The precaudal tail section is close to a rectangular panel and it is reasonable to approximate the added-mass coefficient $c_{A_1} \approx 1$; however, the caudal tail shape is not close to a rectangle, and calculating the exact value of c_{A_2} is tedious. To find a reasonable value for c_{A_2}, we compute the value that balances thrust and drag forces for the two observed gaits provided by [1]. Figure 3.5 plots the lines in the (c_{A_1}, c_{A_2}) plane on which the thrust and drag balance for the two observed gaits. Averaging c_{A_2} values at $c_{A_1} = 1$ gives $c_{A_2} = 2.53$. The fluid force parameters used in our analysis are summarized in table 3.2, where A_i is the cross-sectional area of the cylindrical fluid accelerated by the ith tail panel. Note that with this body division, A_1 and A_2 are approximately equal, leading to insightful results later.

3.3 Optimal Gait Analysis

Various periodic forcing of the bending moment results in different tail oscillation patterns (gaits), which may lead to different characteristics (e.g. efficiency) of swimming. To determine whether natural swimming gait is optimal, we compare the frequency and shape of body oscillation observed in natural swimming with the solution from optimal gait theory [21]. An optimal periodic body motion can be defined and computed by the minimization of a quadratic cost function subject to drag-thrust balance at a desired locomotion velocity.

Optimal gaits are specified as follows. We apply a sinusoidal bending moment at the anterior tail joint. The amplitude and frequency of the driving input are constrained so that the model fish swims at a prescribed average velocity in the steady-state, balancing thrust and drag. Among those satisfying this constraint, we choose the bending moment that gives the smallest value of a selected cost function. The optimal input, and hence the optimal gait at a prescribed velocity, are thus determined for a given set of body and fluid parameters. We have examined various cost functions including the power consumption and

body curvature, and found that choosing the smallest amplitude of active bending moment gave the optimal gait closest to the observed motion; the result of this case will be reported below.

For minimal cost of bending moment due to muscle tension, the problem is formulated as follows:

$$\min_{u,\theta\in\mathbb{P}_\tau} \quad \frac{1}{\tau}\int_0^\tau ||u||^2\,\mathrm{d}t \tag{3.5}$$

subject to (3.3) and (3.4), where $\mathbb{P}_\tau$ is the set of τ-periodic signals. The theory [21] indicates that the optimal bending moment $u \in \mathbb{P}_\tau$ is a sinusoid and has the form $u(t) = \Re[\hat{u}e^{j\omega t}]$, where $\hat{u} \in \mathbb{C}^2$ is the phasor of $u(t)$, and $\omega := 2\pi/\tau$ is the oscillation frequency. In particular, the optimal solution is given in terms of the largest eigenvalue λ_o and the corresponding eigenvector $\hat{u}_o$ of the matrix Z:

$$Z := \mathcal{P}_\omega^*(G+G^\mathsf{T})\mathcal{P}_\omega(\omega/v)^2/(2c) \tag{3.6}$$

where $\mathcal{P}_\omega := \mathcal{P}(j\omega)$ is the frequency response of the transfer function from the bending moment u to the tail angle θ:

$$\mathcal{P}(s) := (Js^2 + 2vGs + K)^{-1}B.$$

The minimal value of the cost in (3.5) for a given frequency ω is equal to $1/\lambda_o$; thus, the optimal frequency, ω_o, that minimizes the muscle tension cost, can be found using a line search over all frequencies to maximize λ_o. Consequently, the optimal body shape phasor, $\hat{\theta}_o$, can be found using the transfer function at the optimal frequency; $\hat{\theta}_o = \mathcal{P}(j\omega_o)\hat{u}_o$. We can then compare the optimal gait, $\theta_o(t) = \Re[\hat{\theta}_o e^{j\omega_o t}]$, with the natural gait $\theta_{nat}(t)$.

The same active bending moment can generate tail oscillations of different shapes depending upon the tail stiffness. Therefore, the stiffness value can have a large impact on the swimming performance. While observations and experiments in the literature provide preliminary results on how body flexibility varies with body position and speed, they do not provide actual values for live saithe the body stiffness that can be used to determine k_1 and k_2 in our model. In fact, stiffness values are probably actively adjusted for a given speed through co-contraction of left/right muscles [24]. To test this hypothesis, we set k_1 to be a

reasonable scalar multiple of k_2, and include k_2 in the optimal gait problem as an adjustable parameter. We examine cases with various ratio k_1/k_2, for a sensitivity study, since a definite relationship between the body flexibility at various points on the body is not known.

Overall, the frequency and amplitude of sinusoidal active bending moment u_1 and tail stiffness k_2 are optimized to achieve a given average speed with minimum amplitude of u_1, while hydrodynamic and body geometry/mass parameters, and the stiffness distribution over the body, k_1/k_2, are fixed. The optimization is repeated for various swim speeds in a range observed in saithe swimming to determine whether the observed gaits can be explained by optimality. When we examine hydrodynamic resonance in Section 3.4.2.3, the procedure is modified by assuming that the fish body has no mass or stiffness and both tail joints are driven by active muscle bending moments. In this case, tail stiffness parameters are set to zero ($k_1 = k_2 = 0$), and frequency, amplitudes, and phases of bending moments u_1 and u_2 are adjusted to minimize the sum of squares of the bending moment amplitudes.

3.4 Results

3.4.1 Intrinsic Properties of Steady Fish Swimming

Given a particular gait θ, the equations of motion, (3.3) and (3.4), allow us to determine the muscle bending moment u that generated the motion, and the resulting average steady speed v. Various combinations of (θ, u, v) would satisfy the equations, but there are certain properties that are shared by all combinations. This section presents such gait-independent intrinsic properties.

3.4.1.1 Strouhal Number

In equation (3.4), the average thrust force over one cycle is balanced with the total drag to achieve a steady-state velocity. Rewriting this thrust-drag balance using phasor notation $\theta(t) = \Re[\hat{\theta} e^{j\omega t}]$ gives:

$$\omega^2 \hat{\theta}^* (G + G^\intercal) \hat{\theta} = 4cv^2. \tag{3.7}$$

The matrix G is a function of the undulating panel lengths, $2l_i$, and the added mass of the fluid accelerated by each panel, $m_{A_i} := \rho A_i(2l_i)$. For the saithe model, with parameters given in Section 3.2.1, the virtual mass per unit length is roughly constant, i.e. $A_1 = A_2 =: A_o$. In this case, the rank of the matrix $G + G^\intercal$ becomes one, and we can factor it out as $G + G^\intercal = \rho A_o l l^\intercal$, where $l \in \mathbb{R}^2$ is a stacked vector of panel lengths $2l_i$. Assuming small oscillation angles θ_i, the lateral tail-tip displacement can be approximated as $y \cong l^\intercal \theta$. The thrust-drag balance equation can then be simplified to give the following expression for the ratio of the locomotion velocity v to the maximum tail-tip velocity $v_t := \max_t \dot{y}$:

$$\frac{v}{v_t} = \sqrt{\frac{A_o}{2c_D A_w}}. \tag{3.8}$$

Equation (3.8) implies that the average swimming velocity is proportional to the maximum tail-tip velocity, with a constant determined from only the fish's body geometry and hydrodynamic force parameters. If a fish has a large drag coefficient c_D or a large wetted area A_w, a higher tail-tip velocity v_t is required to achieve a given speed v. The relationship expressed in equation (3.8) agrees with observations from biology. Data on carangiform locomotion of live scombroid fish shows a linear relationship between swim speed and tail speed [70, 71]. This relationship was calculated by [72] to be $v/v_t = 1.21$ for steady swimming, and $v/v_t = 1.9$ for swimming starting from rest. Tail velocity also appears to be directly proportional to swim velocity in anguilliform swimming of eel [73]. In our simple model, we get $v/v_t = 1.57$, similar to the expressions found by [72], while live fish observation gives $v/v_t = 1.44$ [2].

The nondimensional Strouhal number is defined by $St = h/(v\tau)$, and can be interpreted as the ratio of the peak-to-peak tail amplitude h to the distance traveled over a cycle $v\tau$. Because the maximum tail-tip velocity is given by $v_t = \pi h/\tau$ for sinusoidal oscillations, the Strouhal number can also be viewed as the ratio $St = (1/\pi)(v_t/v)$, leading to the expression:

$$St = \frac{1}{\pi}\sqrt{2c_D \cdot \frac{A_w}{A_o}}. \tag{3.9}$$

The relationship (3.8) between the locomotion velocity and tail-tip velocity makes St predetermined based on the fish's body geometry and fluid parameters, and independent of gait

and velocity. Slow propulsion with fast tail-beat (higher St) results from a larger wetted area A_w, larger drag coefficient c_D, and/or smaller amount of water pushed by the tail A_o. The saithe model has $St = 0.2$, which is close to values observed for live saithe. If the virtual masses per unit length are not equal, i.e. $A_1 \neq A_2$, the expression for St in (3.9) remains with a new definition for A_o:

$$A_o := A_2 + (A_1 - A_2)(v_m/v_t)^2,$$

where v_m is the maximum lateral velocity of the posterior joint. Consequently, St may vary with the distribution of lateral velocity along the body.

3.4.1.2 Power Consumption and Froude Efficiency

In the literature, power consumption and Froude efficiency have been calculated using Lighthill's reactive theory for a continuum model of fish body that periodically undulates at a frequency ω, and sends traveling waves down its body to swim at a constant (average) velocity v. In this study, we calculate these quantities using the discrete and bilinear model (3.3) and (3.4). The calculated values will not be perfectly accurate due to the simplification of the model, but provide new analytical insights into efficiency associated with swimming dynamics.

Basic power equations are obtained by multiplying (3.3) and (3.4) by $\dot{\theta}^\intercal$ and v, respectively:

$$E = R + V + W, \qquad \overline{D} = \overline{P} v \tag{3.10}$$

where E is the power supplied by the muscle, W is the power lost into water, R and V are the rotational kinetic and elastic potential powers, D is the power loss due to viscous fluid drag, and P is the thrust force. These quantities are defined by

$$E := \dot{\theta}^\intercal B u, \qquad R := \dot{\theta}^\intercal J \ddot{\theta}, \qquad V := \dot{\theta}^\intercal K \theta, \qquad W := 2v\dot{\theta}^\intercal G \dot{\theta}, \qquad \overline{D} := cv^3, \qquad \overline{P} := -\overline{\theta^\intercal G^\intercal \ddot{\theta}}.$$

During steady swimming, the average kinetic and potential energies are constant. Thus, averaging of the first equation in (3.10) yields $\overline{E} = \overline{W}$, indicating that the muscle power supply $\overline{E}$ is equal to the power lost into water $\overline{W}$. The second equation in (3.10) shows that

the thrust power gained by the body through reactive hydrodynamic forces equals the power loss due to drag during steady swimming.

Now, based on the above analytical formulas for W and P, one can readily verify through integral by parts that $\overline{W} = 2\overline{P}v$. This implies $\overline{E} = 2cv^3$, and thus the total power consumption E on average is estimated to be twice the power required for towing the fish body, and is independent of the body gait and oscillating frequency. Therefore, it does not make sense to optimize the gait to minimize power consumption because the total power $\overline{E}$ is determined only by the swimming velocity v and the fluid drag coefficient c, which are fixed in this analysis. The expression for $\overline{E}$ arises from the work done to push fluid both axially and laterally, as explained in Section 3.5.1. For saithe, the power consumption at a nominal speed 1 m/s is estimated to be $\overline{E} = 0.58$ W. The average power consumption for saithe was calculated in [2] to be $0.0014\rho l_b^5 T^{-3}$ which equals 0.61 W for a 0.4 m fish swimming at 3.5 Hz. The Froude efficiency, or the propulsive efficiency, is the ratio of useful power output to the total power consumption, defined as $\eta := \overline{P}v/\overline{E}$. According to our results using a bilinear, discrete reactive fluid model, $\overline{E} = 2\overline{P}v$. This relationship makes the Froude efficiency always equal to $\eta = 0.5$, regardless of the swimming gait, speed, and body geometry.

3.4.2 Optimal Gait Analysis

3.4.2.1 Natural Gait is Optimal

This section examines whether the observed gait of saithe is optimal with respect to a certain cost function. The previous section revealed that both total power consumption and Froude efficiency are independent of gait, and not appropriate cost functions for characterizing the natural gait in terms of an optimality. As an alternative, we minimize the muscle tension or bending moment cost while maintaining a given swimming speed, and solve for the optimal periodic body shape and oscillation frequency, using optimal gait theory provided in Section 2.3. We compare the optimal gaits at various speeds with data on live saithe swimming provided by [1, 2] to examine optimality of the natural gaits. We also determine the role that body stiffness, driving frequency, and tail-tip amplitude play in varying the

desired speed.

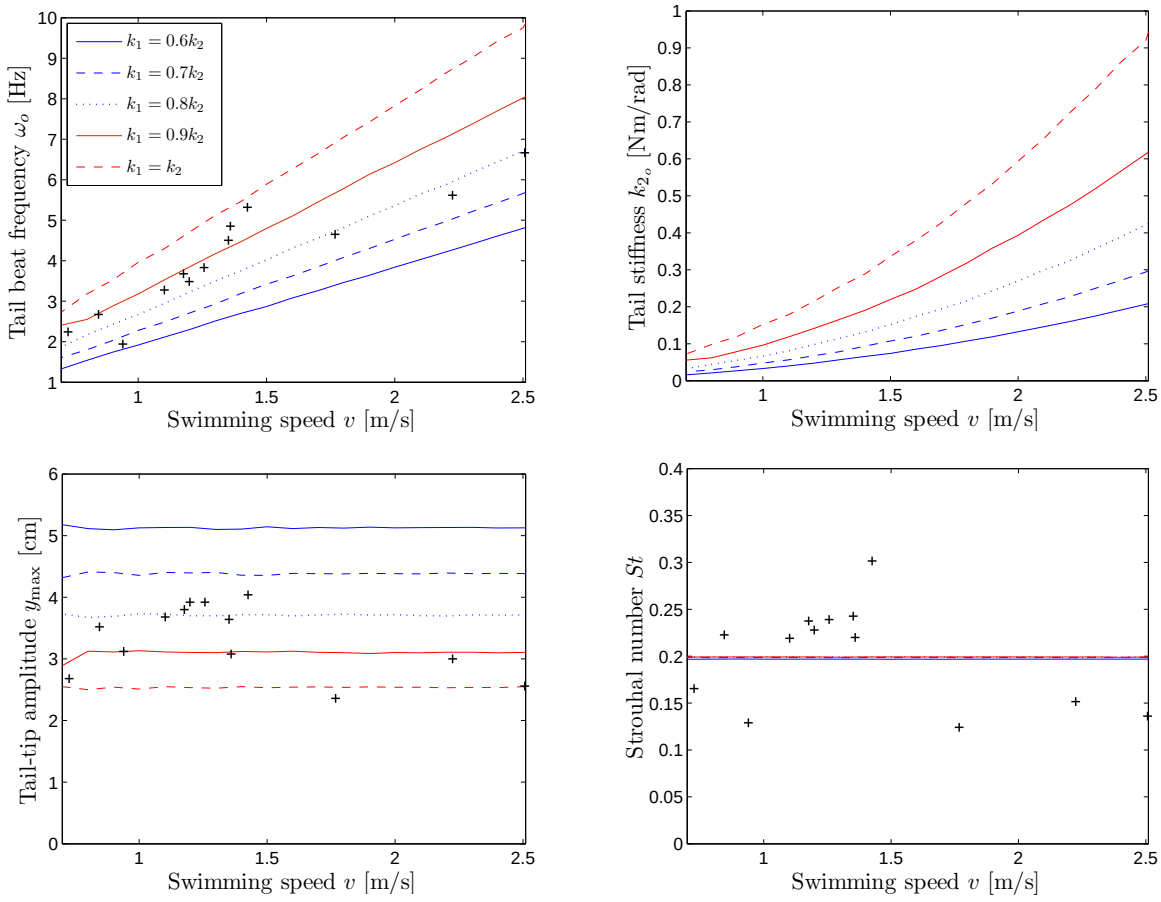

Figure 3.6: Results for optimal gait that minimizes muscle bending moment for the saithe model with a passive tail over a range of velocities. The tail joint stiffness is also optimized while the ratio of anterior stiffness to posterior stiffness is fixed. The data points indicated by "+" are from [2]. As the swimming speed increases, the frequency linearly increases while the amplitude remains roughly constant so that St stays constant as analytically predicted. The optimal gaits are reasonably close to the observed data.

Undulatory motion of fish is driven by anterior muscles in the precaudal region, and the resulting wave is propagated down the tail through the body's passive stiffness [64, 65, 66]. To make our model similar to live fish, we allow the tail to oscillate passively; the muscle bending moment u_1 is applied only at the first joint between the main body and precaudal region, and the second joint between the precaudal and caudal tail sections is assumed

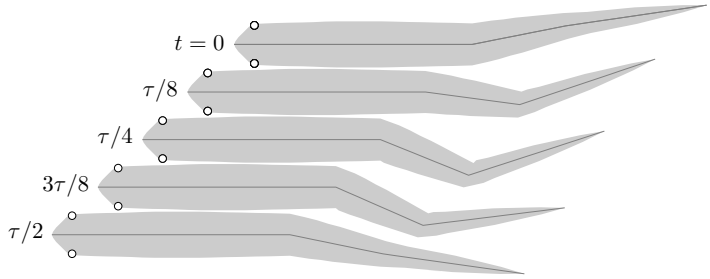

Figure 3.7: Snapshots of the optimal gait that minimizes muscle bending moment at a locomotion velocity of 1.2 m/s. The precaudal and caudal tail stiffnesses are optimized assuming $k_1/k_2 = 0.85$. The optimal oscillation frequency is 3.52 Hz and the optimal stiffness is $k_{2_o} = 0.117$ Nm/rad.

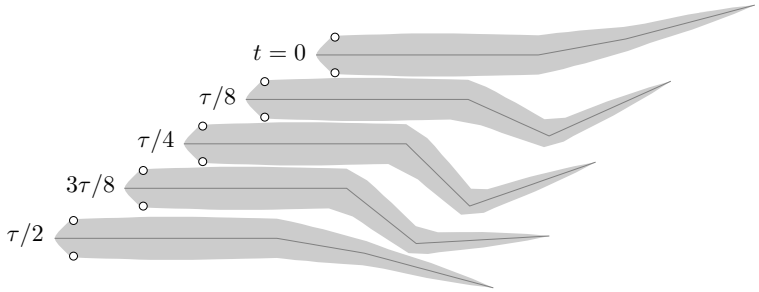

Figure 3.8: Snapshots of the hydrodynamically optimal gait. The conditions are the same as those for Fig. 3.7, except the fish model has no body mass or body stiffness, and both joints receive bending moment inputs. The optimal oscillation frequency is 2.38 Hz.

completely passive, i.e. $u_2(t) \equiv 0$. In this case, u and B are redefined to be u_1 and the first column of the original B matrix, respectively (see the Appendix).

While observations and experiments in the literature provide preliminary results on how body flexibility varies with body position and swimming speed, they do not provide actual values for live saithe body stiffness that can be used to determine k_1 and k_2 in our model. In fact, the stiffness values are probably actively adjusted for a given swimming speed through co-contraction of left/right muscles [24]. Therefore, we set k_1 to be a reasonable scalar multiple of k_2, and include k_2 in the optimal gait problem as an adjustable parameter. We examine cases with various ratio k_1/k_2 since a definite relationship between the body

flexibility of live fish at various points on the body is not known.

The results of the optimal gait calculations (figure 3.6) show that the optimal frequency ω_o increases linearly with increasing locomotion velocity v. The optimal stiffness at the second joint between the precaudal and caudal regions, k_{2_o}, exhibits polynomial growth with an increase in velocity. In fact, it can be analytically verified that optimal ω_o and k_{2_o} are proportional to v and v^2, respectively. The tail-tip amplitude $y_{max} := \max\ y(t)$, however, remains constant, keeping the Strouhal number St also a constant. The results from the optimal gait closely match the data of live saithe swimming when the precaudal stiffness is approximately 85% of the caudal stiffness. Snapshots of the optimal body motion are shown in figure 3.7 for the case $k_1 = 0.85k_{2_o}$, where the fish is swimming with an oscillation frequency of 3.52 Hz. The swimming motion in figure 3.7 closely resembles the observed swimming shown in figure 3.4. Thus, saithe appears to minimize active muscle bending moment during steady-state swimming by adjusting its gait, tail beat frequency, and body stiffness.

3.4.2.2 Optimal Gait Exploits Resonance

We will present an analytical explanation for the optimal frequency ω_o and why it is linearly proportional to swimming speed. We theorize that both body resonance and fluid resonance are exploited in the optimal frequency and in natural swimming. As in Section 3.4.1.1, we consider the case where the added masses per unit length are equal, i.e. $A_1 = A_2$. This approximation is reasonable for our model, and provides analytical insights into how optimal, and hence natural, gait exploits resonance.

When a sinusoidal bending moment of frequency ω is applied to the anterior tail joint, the tail tip oscillates laterally at the same frequency. According to the optimal gait theory, the cost of bending moment or muscle tension (3.5) is given by $1/\lambda_o$, where λ_o is the maximum eigenvalue of the matrix Z defined in (3.6). Assuming $A_1 = A_2 =: A_o$, the eigenvalue is given by

$$\lambda_o = \left(\frac{A_o}{c_D A_w}\right) \left\| \frac{Q(j\omega)}{v} \right\|^2, \qquad Q(s) := sl^{\mathsf{T}} P(s),$$

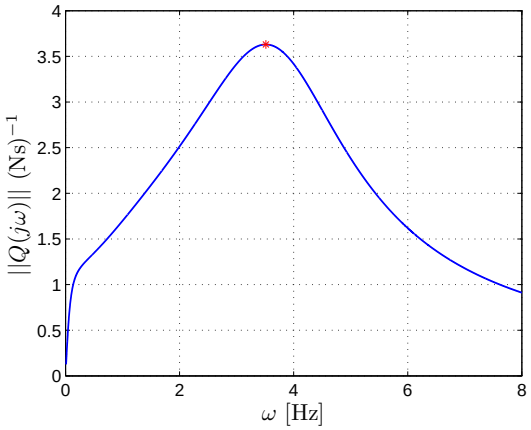

Figure 3.9: The gain of $Q(j\omega)$ over a range of frequencies, where $Q(s)$ is the transfer function from the muscle bending moment u_1 to the tail-tip velocity. The speed is $v = 1.2$ m/s and the tail stiffness is specified as $k_1 = 0.85k_2$ and $k_2 = 0.117$ Nm/rad. There is a peak, or resonance frequency at $\omega_r = 3.51$ Hz.

where $Q(s)$ is the transfer function from input torque u to the lateral tail-tip velocity $\dot{y}$. The optimal frequency that maximizes λ_o is the peak frequency that maximizes the gain (spectral norm) of $Q(j\omega)$. Thus, the optimal frequency that minimizes the torque or muscle tension cost is the resonance frequency that maximizes the tail-tip velocity for a given magnitude of the bending moment. Since steady swimming speed is proportional to the maximum tail-tip speed, (3.8), we can also interpret the resonance with the frequency that maximizes the ratio of swimming speed to input torque magnitude.

To verify existence of the resonance, we consider the optimal locomotion example shown in figure 3.7, where the optimal frequency is $\omega_o = 3.52$ Hz. The plot of the amplification factor $\|Q(j\omega)\|$ as a function of frequency ω is shown in figure 3.9. There is a well-defined resonance peak that maximizes $||Q(j\omega)||$ at 3.51 Hz. Because of the slight difference in the values A_1 and A_2, there is a negligible difference between the optimal frequency ω_o and the resonance frequency.

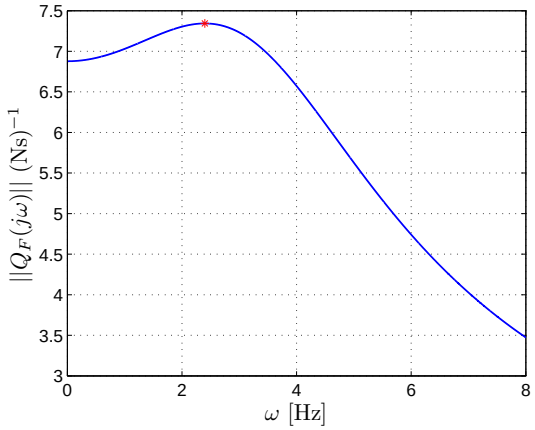

Figure 3.10: The gain of $Q_F(j\omega)$ over a range of frequencies, where $Q_F(s)$ is the transfer function from the muscle bending moments (u_1, u_2) to the tail-tip velocity when the fish has no body mass or body flexibility. There is a peak, or resonance frequency at $\omega_r = 2.4$ Hz.

3.4.2.3 Hydrodynamics and Body Flexibility Resonate

The previous two sections have shown that a swimming saithe exploits resonance to achieve a desired swimming speed with minimal load on muscle. This section explores the origin of the resonance. When the fish body is flexible, there may exist a peak resonance of the transfer function $Q(j\omega)$, that is close to the natural frequency of the fish body. But it is possible that this resonance is also related to a hydrodynamic resonance due solely to the fluid. We separately examine these two possible sources of resonance.

The moment of inertia matrix J in the equation of motion, (3.3), can be split into the summation of the fish body inertia matrix and the added-mass fluid inertia matrix, $J = J_B + J_F$. The natural frequencies of the fish body itself coincide with the resonance frequencies of $Q(s)$ without water:

$$Q_B(s) := sl^{\mathsf{T}}(J_B s^2 + K)^{-1} B,$$

and are equal to the square roots of the generalized eigenvalues of (J_B, K). For the swimming fish shown in figure 3.7, the first two natural frequencies of the body are 1.12 and 6.13 Hz, which are in the same order as the resonance frequency $\omega_r = 3.52$ Hz, but are not very close. Alternatively, the resonance frequencies can be defined using the effective inertia

matrix J containing both body and added-mass. In this case, (J, K) gives the frequencies of natural body oscillations in still water. These natural frequencies coincide with the resonance frequencies of $Q(s)$ at zero swimming speed:

$$Q_0(s) := sl^{\mathsf{T}}(Js^2 + K)^{-1}B.$$

With the fluid inertia added, the natural frequencies are at 0.49 Hz, and 3.29 Hz. Therefore, the tail beat frequency of optimal (and natural) swimming is close to the second natural mode of oscillation in $Q_0(s)$ resulting from body flexibility and total effective mass.

To study hydrodynamic resonance, we remove the stiffness and mass of the fish body, and assume that the fish model can achieve an arbitrary tail motion through bending moment inputs at both joints. In this case, the transfer function from bending moments to lateral tail-tip velocity $Q(s)$ becomes

$$Q_F(s) = l^{\mathsf{T}}(J_F s + 2vG)^{-1}B.$$

We can view $Q_F(s)$ as a transfer function which describes the input/output dynamics of a massless ribbon swimming in water. The moment of inertia matrix, J_F, is symmetric and positive definite; the hydrodynamic torque matrix G, however, is an asymmetric upper triangular matrix; thus, the transfer function contains the fluid inertia and skewed damping due to fluid flow. Although the body lacks stiffness, there is still a well-defined peak that maximizes the gain of the transfer function $Q_F(s)$ because of the structure of G (figure 3.10). This resonance occurs at $\omega_r = 2.4$ Hz, which is reasonably close to the natural swimming frequency at 3.5 Hz.

Figure 3.8 depicts snapshots of the optimal gait, which minimizes muscle tension, when there is no body mass or stiffness. Because the optimal frequency is at 2.4 Hz, and the fish is swimming with a locomotion speed of 1.2 m/s, the tail-tip height is larger than in observed swimming, such that the Strouhal number remains at 0.2.

3.5 Discussion

The results in this chapter are derived from a simple fish swimming model, with hydrodynamic forces modeled as static functions of relative velocity and acceleration. Due to the approximations, our results may not be exactly accurate in a quantitative sense, and we remain cautious when interpreting the results. Nevertheless, the model presumably captures essential dynamics of fish swimming, and the results should provide basic understanding of swimming mechanisms. The results are applicable when the body can be roughly separated into a main body and tail sections, the main body's lateral motion is negligible compared to the tail motion, and reactive force model for thrust generation is valid.

3.5.1 Power Equality for Lateral Kinetic Loss and Thrust

The total power used in swimming is found to be invariant over various gaits; it is always equal to $2cv^3$, twice the power loss due to resistive drag, regardless of the hydrodynamic parameter values, and is proportional to the swimming speed cubed. Regardless of the gait, a speed v is achieved with the same power cost as long as the maximum tail-tip speed v_t is a fixed fraction of v as specified by (3.8). Therefore, power optimality cannot be the reason why fish consistently choose particular gaits. It should be noted, however, that the "total power" we examined is the mechanical power output from muscle that is eventually dissipated into water; power loss associated with muscle activation is not considered. If the activation cost is considered, it may still be possible to explain the natural gait by power optimality.

Fish swim by transferring a supply of power between their muscles, their tail, and the water. Figure 3.11 shows a diagram of this energy transfer. First, muscles provide a total average supply of power, $\overline{E}$, to the tail, through bending moment input. The tail transfers this energy to the water as the rate of work $\overline{Y}$ done in the lateral direction; $\overline{E} = \overline{Y}$. The water then gains a portion as kinetic power, $\overline{T}$, and returns the rest, $\overline{P}v$, to the tail for thrust generation; $\overline{Y} = \overline{T} + \overline{P}v$. The thrust power is eventually dissipated as heat, $\overline{D}$, through resistive drag on the body; $\overline{P}v = \overline{D}$. Overall, the total power supplied by muscle is lost

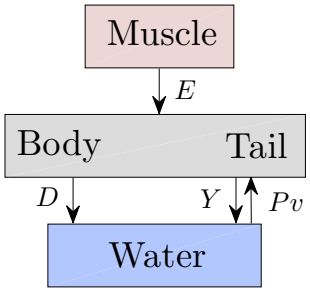

Figure 3.11: Diagram of the energy transfer that occurs between the fish muscles, the main body and tail, and water. E is the total power supplied by muscle, Y is the rate of work done by tail to water in the lateral direction, Pv is the thrust power returned by water to tail, and D is the power loss due to resistive drag.

into water in two forms, $\overline{E} = \overline{D} + \overline{T}$. The loss due to drag, $\overline{D} = cv^3$, is a price to be paid regardless. The additional loss, $\overline{T}$, is the overhead cost required when generating thrust by pushing water in the lateral direction; $T = w^\intercal f$ where $w := \dot{y} + v\theta$ is the fluid velocity in the y direction. A major finding of our analysis is that, to generate thrust power $\overline{P}v$, fish has to waste the same amount of power in the lateral direction as the rate of kinetic energy gained by water; $\overline{T} = \overline{P}v$. The thrust power is equal to the main body drag power D, dissipated as heat.

Because of the equality between kinetic power $\overline{T}$ and thrust power $\overline{P}v$, our result predicts that the ratio of useful power to total power, known as Froude efficiency, $\eta := \overline{P}v/\overline{E}$, is exactly $1/2$, regardless of the gait, swim speed, or driving frequency. Biological data [2] indicate that η is in the range 0.52–0.72 for steadily swimming saithe, which is larger than the predicted value $1/2$. We suspected that a large portion of the error is attributed to the approximation associated with linearizing the model, and studied the power transfer of the original nonlinear model from which the bilinear model, (3.3) and (3.4), was derived. The original nonlinear model contains trigonometric terms of θ, including the nonlinear acceleration term for reactive hydrodynamic forces as in [50]. Because it is difficult to study the nonlinear model analytically, numerical simulations are used to determine if the nonlinear model gives reasonable results. As expected, simulations of the nonlinear model give more

realistic values of Froude efficiency that are larger than or less than 1/2, depending on the gait, frequency, and steady swimming speed. Thus, we predict $\eta \approx 1/2$ for swimming with small oscillation amplitude. Higher Froude efficiency ($\eta > 0.8$) of thunniform swimming [74] cannot be predicted by our model since the main thrust source is lift force rather than added-mass effect [75].

3.5.2 Invariance of Strouhal Number

The non-dimensional Strouhal number St describes the wake structure in fish swimming. Fish and cetaceans generally swim with St between 0.2-0.4, with the saithe St lying on the lower end of this interval [68]. Biological data of a variety of fish, including dace, trout, goldfish, and jack mackerel, have pointed to a linear relationship between oscillation frequency and swim speed, and a direct relationship between tail-tip amplitude and body length. Based on these results, various literature have concluded that St remains constant for a fixed ratio of swim speed to tail-beat frequency v/ω [27, 76]. According to our analysis, thrust-drag balance requires the ratio of swim speed to maximum tail-tip speed v/v_t, and therefore St, be a constant depending on only the fish's body geometry and hydrodynamic parameters. The optimality for small tension then explains the observed proportionality of frequency and constancy of tail-tip amplitude with respect to speed.

Interestingly, [77] observed that St is a function of a single parameter called the Lighthill number $Li := c_D A_w / b^2$, where b is the tail tip height. If the volume of fluid accelerated by tail is estimated by a circular cylinder of diameter αb with a constant α depending on the tail geometry, then the cross-sectional area of the added mass is $A_o = \pi(\alpha b/2)^2$, and the formula in (3.9) reduces to $St = (2/\pi)^{3/2}\sqrt{Li}/\alpha$, explicitly showing the dependence of St on Li. Moreover, this simple formula with $\alpha \approx 0.5$ explains the (Li, St) relationships for many species in Fig. 4 of [77]. While [77] interpreted the result through power optimality, our analysis derives this formula from thrust-drag balance without optimality.

Experimental data from oscillating foil in fluids have demonstrated maximum Froude efficiency η for St in the range of 0.25-0.35 due to efficient thrust development [30, 34, 78].

There is an apparent discrepancy between these results and our results, which state that St is independent of gait optimality. This discrepancy arises because the literature defines wake resonance as maximum spatial amplification of unstable flow, while our St results follow from the assumption of thrust-drag balance. For a fixed oscillation frequency and tail-tip amplitude, our fish model will achieve a certain swimming speed; this speed is incomparable to the fixed fluid speed that flows past an airfoil which is oscillating mechanically with a fixed amplitude and frequency. Our results predict that if thrust-drag balance is taken into account in oscillating foil experiments, such that two parameters in (v, ω, h) are fixed and the third is measured in steady flow, the St will remain fairly constant.

3.5.3 Optimality of Natural Swimming

To determine whether the periodic body motion in natural swimming is optimal, we defined and solved the optimal gait that minimizes muscle bending moment, and compared the results to data of live saithe swimming. The model was adjusted to have an active anterior tail and a passive caudal tail fin, to capture the anatomy of live fish. Because no data is available on the body stiffness of swimming saithe, we included the stiffness as an optimization parameter, with a fixed ratio of precaudal stiffness k_1 to caudal stiffness k_2. Our choice to adjust stiffness while keeping k_1/k_2 constant was based on the observation that local body flexibility at a cross-section of a swimming fish is related to the muscle activation level and body curvature at that cross-section.

The total bending stiffness is determined by the active and passive stiffness of the muscle-tendon-skin system and the vertebral column stiffness [79, 25]. It is proposed that active muscles modulate the muscle stiffness to reduce the bending cost by bringing the body's natural frequency closer to the tail-beat frequency [26, 29, 80]. The increase in body stiffness is generated by negative muscle work to resist muscle strain [66]. Experimental results on the stiffness properties of the intervertebral joints of blue marlin suggest that caudal intervertebral joints have a higher stiffness than precaudal joints, and an increase in bending amplitude results in an increase in stiffness [81]. Experiments on the fish skin of longnose gar

suggest that skin resists bending at high curvatures and permits bending at small curvatures [26]. These studies indicate that the total fish stiffness should increase with an increase in swimming speed, and the stiffness in the caudal region should be greater than the precaudal region due to higher curvature and higher muscle strain. In the natural gait, the curvature of saithe at 50% of the body length is approximately 63% of the curvature at 70% of the body length [1]. According to [82] the red muscle strain of swimming mackerel at 50% of the axial position is approximately 80% of the strain at 70% of the axial position, while the curvature is about 55%. Consistent with these results, comparison of model-predicted optimal gaits with natural gaits of live saithe suggested that the precaudal stiffness k_1 is about 85% of the caudal stiffness k_2, and the stiffness is actively adjusted to increase quadratically with the swimming speed.

The results demonstrated that characteristics of natural gaits over a range of swimming speeds can be explained by optimality of minimum bending moment. In particular, the data collected from live saithe swimming indicated that the oscillation frequency linearly increases with speed while tail-tip amplitude remains constant. These properties are captured by the optimal gaits with frequency and amplitude values close to observations (figure 3.6). The linearly increasing frequency can be explained in terms of optimality, together with resonance mechanisms. The constancy of the amplitude then follows from the constancy of the Strouhal number. Because these numerical results match tendencies observed in live fish swimming, and the optimal body shape is close to the observed gait, we stipulate that the optimal gait which minimizes muscle tension can explain carangiform locomotion.

3.5.4 Resonance Mechanisms Underlying Swimming

An essential question in animal locomotion is how animals choose a specific oscillation frequency to achieve a desired steady-state velocity. Most biological observations hint at the exploitation of the natural dynamics associated with the interaction of the (flexible) body and environment in order to reduce energy consumption [80]. Additionally, experimental data from wake production of oscillating foils have demonstrated the existence of a “wake

resonance," which maximizes thrust production [30]. Based on these results we predicted that natural fish swimming is exploiting some type of resonance, which is due to a combination of natural body frequency and hydrodynamic resonance. Our results confirmed this prediction. We found that the natural gait is optimal with respect to minimum bending moment, and the optimal gait exploits resonance to maximize the tail-tip velocity. Therefore, we conclude that there are resonance mechanisms underlying natural gait of swimming.

The results demonstrated that fish swims faster by increasing its oscillation frequency. Because the tail oscillation is exploiting resonance, the body adjusts its stiffness so that the resonance frequency matches the frequency required to achieve a desired speed. This result agrees with the frequency tuning theory observed in animals [26, 29, 80]. The model analytically predicts that the optimal tail beat frequency ω and tail stiffness K are proportional to v and v^2, respectively, and the optimal tail beat amplitude stays constant over a range of swimming speeds. Many fish exhibit the proportionality and constancy properties [30], and hence our result may suggest resonance exploitation in general fish swimming.

A remaining question is: what is the origin of the resonance? Consider a virtual experiment where the fish body is fixed in a flow tank to experience fluid flow at velocity v. If a sinusoidal muscle bending moment of a fixed amplitude is applied to flip the tail, there is a frequency at which the amplitude of the lateral tail velocity is maximum; this is the resonance observed in figure 3.9. In Section 3.4.2.3, we found that this resonance is still observed when we remove the body mass and stiffness. Thus, the origin of the overall resonance may be traced to the dynamics without body. Because this peak is purely due to the fluid effects, we call it a hydrodynamic resonance. However, its relation to the so-called wake resonance [34] is not immediately clear since the latter is unrelated to the muscle bending moment.

The hydrodynamic resonance found in Section 3.4.2.3 may be explained in terms of the natural oscillation resulting under no muscle moment input, thereby making a possible connection to the wake resonance. With no input or body inertia/stiffness, the tail motion is governed by

$$J_F\ddot{\theta} + 2vG\dot{\theta} = 0.$$

The natural dynamics are described by the eigenvalues of $2vJ_F^{-1}G$, which turn out to be complex, and therefore an ideal fish body with no mass/stiffness can naturally oscillate in a flow without muscle input. The natural oscillation could be exploited to resonate the tail motion with the input excitation. The period of the natural oscillation can also be analytically derived for the simplified case, where the precaudal and caudal panels are assumed equal ($l_1 = l_2$, $A_1 = A_2$), as follows:

$$\tau_{\text{nat}} = \left(\frac{14\pi}{12\sqrt{3}}\right)\left(\frac{l_t}{v}\right) \cong 2\left(\frac{l_t}{v}\right), \tag{3.11}$$

where l_t is the total tail length. As expected, the natural frequency $\omega_{\text{nat}} := 2\pi/\tau_{\text{nat}}$ is close to the resonance frequency; for instance, $\omega_{\text{nat}} = 2.84$ Hz for $v = 1.2$ m/s and $l_t = 0.2$ m. The analytical formula in (3.11) shows that the natural oscillation is most likely related to how water travels across the tail. The tail flips from left to right in roughly l_t/v seconds, equal to the time it takes for water to flow through the length of the tail. Thus, the caudal tail may take advantage of the water accelerated by the precaudal section. Consistently with these observations, it can be shown in the general case that the resonance frequency is proportional to v/l_t, and the proportionality constant is a function of the added-mass coefficients and the number of tail panel divisions.

We have found that both hydrodynamic resonance and body resonance exist separately, and they are reasonably close to the overall resonance and hence to the cycle frequency of natural swimming. While the body resonance frequency can be adjusted by active muscle stiffness, the hydrodynamic resonance frequency is determined essentially by the ratio of the swimming speed to the total tail length. Therefore, our results suggest the following mechanisms underlying natural swimming: the body geometry determines the hydrodynamic resonance to be exploited for swimming at a desired speed, the muscle stiffness is actively adjusted in proportion to the speed squared so that the body resonance is roughly aligned with the hydrodynamic resonance, and then the muscle bending moment drives the tail to excite the overall body-fluid resonance.

CHAPTER 4

Chaos Generation in Coupled Andronov-Hopf Oscillators

4.1 Overview

The purpose of this chapter is to determine conditions on the coupling between a set of oscillators or neurons such that their collective behavior is characterized as chaotic, with a desired unstable limit cycle embedded in a chaotic strange attractor. Due to their ability to capture complex dynamic behavior with a fairly simple structure, Andronov-Hopf oscillators are widely used to model networks of neurons in biological systems [83, 84]. Consequently, we also model our system using a network of two-dimensional coupled Andronov-Hopf oscillators, and set out to design their interconnections such that desired behavior is achieved.

In this study, we consider the characterization of a chaotic strange attractor given by [85]. A strange attractor is an attractor that is not a finite set of points, is not piecewise differentiable, and has a non-integer fractal dimension. A strange attractor is chaotic if it exhibits sensitivity to initial conditions. This property exists if all trajectories with initial conditions on the basin of attraction have a positive maximum Lyapunov exponent.

In order to achieve the objective, we first use a coordinate transformation to describe the dynamics of the oscillators using their amplitudes and phases. We then determine sufficient conditions to ensure the phase instability of a desired limit cycle, with a designable instability magnitude and direction. We then consider a special case of symmetric weak coupling and determine sufficient conditions to guarantee that all harmonic periodic orbits are unstable. Finally, using numerical evidence, we consider several additional conditions,

including symmetry breaking, that increase disorder and contribute to chaos. Numerical examples are then given in the last section to demonstrate the effectiveness and shortcomings of this method.

4.2 Coupled Oscillators Model and Control Objective

Consider a network of n coupled two-dimensional Andronov-Hopf oscillators, modeled by

$$\dot{x} = \begin{bmatrix} \mathcal{E}(x) & -I \\ I & \mathcal{E}(x) \end{bmatrix} x + u(x), \tag{4.1}$$

$$\mathcal{E}_{ii}(x) := 1 - (q_i^2 + p_i^2), \qquad x = \begin{bmatrix} q \\ p \end{bmatrix},$$

where $x \in \mathbb{R}^{2n}$, and the coupling enters through the control input $u(x) \in \mathbb{R}^{2n}$. Without a coupling term, the system has the general τ-periodic solution $x(t) = \xi(t)$, where

$$\xi(t+\tau) = \begin{bmatrix} C_\eta \mathbb{1} \\ S_\eta \mathbb{1} \end{bmatrix}, \qquad \eta := t + \varphi, \qquad \mathbb{1} := \mathrm{col}(1, ..., 1), \tag{4.2}$$

and

$$C_z := \cos(\mathrm{diag}(z)), \qquad S_z := \sin(\mathrm{diag}(z)),$$

for an arbitrary vector z.

Because the plant can be separated into a skew-symmetric section and a nonlinear section, coming from the $\mathcal{E}(x)$ term, $\xi(t)$ is amplitude and period locked at $\mathbb{1}$ and 2π seconds, respectively. However, the phase $\varphi \in \mathbb{R}^n$ remains arbitrary and a function of the initial conditions.

Our objective is to design the controller $u(x)$ such that the system has a chaotic strange attractor, with a desired limit cycle embedded in the attractor. Hypothetically, the controller would add weak coupling between the oscillators, such that the amplitudes remain stable at approximately $\mathbb{1}$, while the phase dynamics destabilize such that the trajectory never settles at a stable limit cycle.

It is well understood that chaotic behavior is only feasible in a nonlinear system. Since the plant, without controller input $u(x)$ is already nonlinear, it is possible to generate chaos and achieve our goal with a linear controller, given by

$$u = \varepsilon H x. \tag{4.3}$$

With the form in (4.3), the controller represents the linear coupling between the oscillators. In order to maintain the stability of the oscillators' amplitudes, we only consider weak coupling, where the order of the coupling is denoted by a sufficiently small $\varepsilon > 0$. We will now begin to design H such that a desired limit cycle remains unstable, while being embedded in a strange attractor.

4.2.1 Coordinate Transformation

Our goal is to design the weak linear interconnections between a network of Andronov-Hopf oscillators (4.1) such that their amplitudes remain stable, while their phases never stabilize, resulting in a chaotic collective behavior. To this end, we consider the following coordinate transformation $(q,p) \leftrightarrow (r,\theta)$, defined by

$$q = C_\theta r, \qquad p = S_\theta r.$$

This coordinate transformation is useful because it more clearly shows how the dynamics and the coupling affect the amplitudes and the phases of the oscillators.

With the new state variables (r,θ), system (4.1) can be expressed as

$$\begin{bmatrix} \dot{r} \\ R\dot{\theta} \end{bmatrix} = \begin{bmatrix} C_\theta \mathcal{E}(C_\theta r, S_\theta r) C_\theta + S_\theta \mathcal{E}(C_\theta r, S_\theta r) S_\theta \\ I - S_\theta \mathcal{E}(C_\theta r, S_\theta r) C_\theta + C_\theta \mathcal{E}(C_\theta r, S_\theta r) S_\theta \end{bmatrix} r + \begin{bmatrix} C_\theta & S_\theta \\ -S_\theta & C_\theta \end{bmatrix} H \begin{bmatrix} C_\theta \\ S_\theta \end{bmatrix} r, \tag{4.4}$$

where $R := \mathrm{diag}(r)$.

One of our goals is to design the coupling such that a desired limit cycle becomes an unstable solution of the system. We choose the periodic orbit given by

$$\hat{\xi}(t+\tau) = \begin{bmatrix} C_{\hat{\eta}} \mathbb{1} \\ S_{\hat{\eta}} \mathbb{1} \end{bmatrix}, \qquad \hat{\eta} := t + \hat{\varphi}, \tag{4.5}$$

with a frequency at 1 Hz, amplitudes at $\mathbb{1}$, and some particular phase $\hat{\varphi}$. Note that for sinusoidal orbits with different amplitudes and frequencies, the developing procedures will still apply and lead to similar conditions. We now require a sufficiency condition on the weak coupling εH that analytically guarantees the instability of the periodic orbit in (4.5).

4.3 Conditions for Orbital Instability

In the study of system stability, Lyapunov exponents are defined for trajectories and are used to quantify the system's sensitivity to initial conditions. The Lyapunov spectrum of a trajectory is primarily measured numerically with system simulation and a practical algorithm. In general, all trajectories that start on the basin of a chaotic strange attractor have both positive and negative Lyapunov exponents [86, 87]. While the positive maximum Lyapunov exponents ensure the instability of the trajectories, the negative Lyapunov exponents allow the stability of the chaotic attractor.

In this study, we do not want to use numerical simulations and measurements in order to enforce the instability of a trajectory. Instead, we use the definition of the maximum Lyapunov exponent to analytically analyze and design the instability of a known solution of the system.

4.3.1 Maximum Lyapunov Exponent Definition

The mathematical definition of the maximum Lyapunov exponent is given as follows:

Definition 1. *Consider a general system*

$$\dot{x} = f(x),$$

where $x(t) \in \mathbb{R}^{2n}$. *Suppose* $\bar{x}(t)$ *is a trajectory of the system. Let* $\Phi(t, t_o) \in \mathbb{R}^{2n \times 2n}$ *be the state transition matrix for the system linearized about* $\bar{x}(t)$, *given by*

$$\dot{w} = A(t)w, \qquad A(t) := \left(\frac{\partial f(\bar{x})}{\partial x} \right)^{\tau}. \tag{4.6}$$

Φ *satisfies*

$$w(t) = \Phi(t, t_o) w_o, \qquad \Phi(t_o, t_o) = I.$$

Define the maximum singular value of the solution, $\sigma(t) = \bar{\sigma}(\Phi(t, t_o))$*. Then, the maximum Lyapunov exponent is defined as [88]*

$$\lambda = \lim_{t \to \infty} \frac{1}{t - t_o} \ln \sigma.$$

When $\bar{x}(t)$ is a bounded numerical trajectory of the system, then a positive maximum Lyapunov exponent is a sufficient condition for the trajectory being chaotic [89]. This condition results from inaccuracies in numerical simulations, which prevent a trajectory from settling on an unstable limit cycle, even with exact initial conditions on the limit cycle. Conversely, when $\bar{x}(t)$ is a possible analytical solution of the system, then $\lambda > 0$ is only a sufficient condition for $\bar{x}(t)$ being unstable. The Lyapunov exponent does not indicate whether or not there is a different stable limit cycle or equilibrium point nearby for the trajectory to settle to. Thus, if for *all* possible solutions of the system, the maximum Lyapunov exponents are positive and the trajectories are bounded, then the system is chaotic. However, checking or designing such a condition is extremely challenging, if not impossible.

4.3.2 Sufficient Condition for a Positive Maximum Lyapunov Exponent

Although the maximum Lyapunov exponent is a practical and effective tool in the numerical analysis of chaotic systems, it is difficult for use in analytical analysis. Thus, we consider an exponentially weighted state transition matrix given by

$$\Psi(t, t_o) := e^{-\mu t} \Phi(t, t_o), \qquad \dot{\Psi}(t, t_o) = (A(t) - \mu I) \Psi(t, t_o), \qquad \Psi(t_o, t_o) = I, \tag{4.7}$$

for some constant $\mu \in \mathbb{R}$. Note that with Ψ, the maximum Lyapunov exponent is given by

$$\lambda = \mu + \lim_{t \to \infty} \frac{1}{t - t_o} \ln ||\Psi(t, t_o)||.$$

We now see that

$$\lambda < \mu \qquad \Rightarrow \qquad \lim_{t \to \infty} ||\Psi(t, t_o)|| \to 0,$$

$$\lambda > \mu \qquad \Rightarrow \qquad \lim_{t \to \infty} ||\Psi(t, t_o)|| \to \infty.$$

Thus, a lower bound can now be derived from the following characterization of the maximum Lyapunov exponent:

$$\lambda = \sup \mu \qquad \text{subject to} \qquad \lim_{t\to\infty} ||\Psi(t,t_o)|| \to \infty. \tag{4.8}$$

Using this lower bound, as well as matrix norm and trace properties, we can formulate a sufficiency condition for the positivity of the maximum Lyapunov exponent. First, we prove a few preliminary results in Lemmas 5 and 6.

Lemma 5. *For some bounded matrix $P(t) \geq 0$, if $\lim_{t\to\infty} trace\Big(\Psi(t,t_o)^T P(t)\Psi(t,t_o)\Big) \to \infty$, then $\lim_{t\to\infty} ||\Psi(t,t_o)|| \to \infty$.*

Proof. Recall that for an arbitrary matrix $X \in \mathbb{R}^{\mathrm{m}\times\mathrm{n}}$, with rank r, the matrix norms satisfy the inequality

$$||X||_2^2 \leq ||X||_F^2 \leq r||X||_2^2 \leq \ell||X||_2^2, \qquad \ell \triangleq \max(\mathrm{m},\mathrm{n}).$$

Therefore, the following are equivalent:

$$\begin{aligned}
\lim_{t\to\infty} ||\Psi(t,t_o)|| \to \infty \qquad &\Leftrightarrow \qquad \lim_{t\to\infty} ||\Psi(t,t_o)||^2 \to \infty, \\
&\Leftrightarrow \qquad \lim_{t\to\infty} ||\Psi(t,t_o)||_F^2 \to \infty, \\
&\Leftrightarrow \qquad \lim_{t\to\infty} \mathrm{trace}\Big(\Psi(t,t_o)^{\mathsf{T}}\Psi(t,t_o)\Big) \to \infty.
\end{aligned}$$

Note that

$$\begin{aligned}
\underline{\mathrm{eig}}(P(t))\mathrm{trace}\Big(\Psi(t,t_o)^{\mathsf{T}}\Psi(t,t_o)\Big) &\leq \mathrm{trace}\Big(\Psi(t,t_o)^{\mathsf{T}}P(t)\Psi(t,t_o)\Big) \\
&\leq \overline{\mathrm{eig}}(P(t))\mathrm{trace}\Big(\Psi(t,t_o)^{\mathsf{T}}\Psi(t,t_o)\Big).
\end{aligned}$$

Since $P(t) \geq 0$ is bounded and nonzero, the largest eigenvalue is non-zero and positive, thus

$$\begin{aligned}
\lim_{t\to\infty} \mathrm{trace}\Big(\Psi(t,t_o)^{\mathsf{T}}P\Psi(t,t_o)\Big) \to \infty \quad &\Rightarrow \quad \lim_{t\to\infty} \mathrm{trace}\Big(\Psi(t,t_o)^{\mathsf{T}}\Psi(t,t_o)\Big) \to \infty, \\
&\Leftrightarrow \quad \lim_{t\to\infty} ||\Psi(t,t_o)|| \to \infty.
\end{aligned}$$

□

Lemma 6. *Let $\rho(t) \geq 0$ be a function such that trace$(\Phi(t,t_o)^\intercal P(t)\Phi(t,t_o)) \geq \rho(t)$ for some $P(t) \geq 0$ and all $t \geq 0$. Define $\tilde{\mu}$ and λ as*

$$\begin{aligned} \tilde{\mu} &:= \sup \mu \qquad \textit{such that} \qquad \lim_{t\to\infty} e^{-2\mu t}\rho(t) \to \infty, \\ \lambda &:= \sup \mu \qquad \textit{such that} \qquad \lim_{t\to\infty} e^{-2\mu t}||\Phi(t,t_o)||_2^2 \to \infty. \end{aligned}$$

Then, it always holds that $\lambda \geq \tilde{\mu}$. Thus, $\tilde{\mu} > 0$ is a sufficient condition for $\lambda > 0$.

Proof. Based on the matrix norm properties stated in Lemma 5, the following inequalities hold:

$$||\Phi(t,t_o)||_2^2 \geq \frac{1}{2n}||\Phi(t,t_o)||_F^2 \geq \frac{1}{2n\lambda_{max}(P(t))}\text{trace}(\Phi(t,t_o)^\intercal P(t)\Phi(t,t_o)) \geq \frac{\varsigma}{2n}\rho(t),$$

where ς is defined such that $||P(t)|| < \dfrac{1}{\varsigma}\forall t$. Because $\varsigma/(2n)$ is some constant for all time, it will not change the value of $\tilde{\mu}$. Let $\tilde{\mu}_\delta \triangleq \tilde{\mu} - \delta$. Then, for sufficiently small $\delta > 0$,

$$\lim_{t\to\infty} e^{-2\tilde{\mu}_\delta t}||\Phi(t,t_o)||_2^2 \geq \lim_{t\to\infty} \frac{\varsigma}{2n} e^{-2\tilde{\mu}_\delta t}\rho(t) \to \infty.$$

Since $\tilde{\mu}_\delta$ can make the left hand side go to ∞, $\lambda \geq \tilde{\mu}$. □

Using these Lemmas, we can now determine a sufficient condition that ensures the positivity of the maximum Lyapunov exponent for a system linearized about some trajectory $\bar{x}(t)$.

Lemma 7. *Consider a general system $\dot{x} = f(x)$, where the linearized system about some $\bar{x}(t)$ is given by (4.6). Suppose there exist a bounded matrix $P(t) > 0$, a scalar-valued function $\alpha(t) \in \mathbb{R}$, and scalars $t_1 \geq 0$ and $\epsilon > 0$, such that the following conditions are satisfied for all $t \geq t_1$:*

$$A(t)^\intercal P(t) + P(t)A(t) + \dot{P}(t) \geq \alpha(t)P(t), \qquad \int_{t_1}^{t} \alpha(t)dt \geq \epsilon(t - t_1),$$

then, it is guaranteed that $\lambda \geq \epsilon/2$, where λ is the maximum Lyapunov exponent.

Proof. We're going to prove this using the lower bound i.e. show that $\lim_{t\to\infty}||\Psi(t,t_o)|| \to \infty$ for $\mu > 0$. Using Lemmas 5 and 6 above, this is sufficient to proving that $\lim_{t\to\infty}\text{trace}\Big(\Psi(t,t_o)^\intercal P(t)\Psi(t,t_o)\Big) \to \infty$ for $\mu > 0$.

Using the dynamics,

$$\begin{aligned}
\frac{d}{dt}\text{trace}\Big(\Psi(t,t_o)^\intercal P(t)\Psi(t,t_o)\Big) &= \text{trace}\Big(\Psi(t,t_o)^\intercal(A(t)^\intercal P(t)+P(t)A(t)-2\mu P+\dot{P}(t))\Psi(t,t_o)\Big),\\
&= -2\mu\text{trace}\Big(\Psi(t,t_o)^\intercal P(t)\Psi(t,t_o)\Big)\\
&\qquad +\text{trace}\Big(\Psi(t,t_o)^\intercal(A(t)^\intercal P(t)+P(t)A(t)+\dot{P}(t))\Psi(t,t_o)\Big),\\
&\geq -2\mu\text{trace}\Big(\Psi(t,t_o)^\intercal P(t)\Psi(t,t_o)\Big)\\
&\qquad +\text{trace}\Big(\alpha(t))\Psi(t,t_o)^\intercal P(t)\Psi(t,t_o)\Big),\\
&=\Big(-2\mu+\alpha(t)\Big)\text{trace}\Big(\Psi(t,t_o)^\intercal P(t)\Psi(t,t_o)\Big).
\end{aligned}$$

Then,

$$\begin{aligned}
\text{trace}\Big(\Psi(t,t_o)^\intercal P(t)\Psi(t,t_o)\Big) &\geq e^{-2\mu t+\int_0^t \alpha(\text{t})d\text{t}}\text{trace}(P(0)),\\
&\geq e^{(-2\mu t+\epsilon t)}e^{(-\epsilon t_1+\int_0^{t_1}\alpha(\text{t})d\text{t})}\text{trace}(P(0)),
\end{aligned}$$

for some $\epsilon > 0$. Because ϵ is positive, for a small enough positive μ, $\lim_{t\to\infty}\text{trace}\Big(\Psi(t,t_o)^\intercal P(t)\Psi(t,t_o)\Big) \to \infty$. Since μ is a lower bound for λ, it is a sufficient condition for $\lambda > 0$. Given the definition of λ in Lemma 6, it is easy to verify that $\lambda \geq \epsilon/2$. □

In the Lemma above, $\epsilon/2$ represents the lower bound of the magnitude of instability for the trajectory $\bar{x}$. Furthermore, $P(t)$ contains the direction of the instability. For this reason, it can be shown that the sufficiency condition is invariant under a similarity transformation.

Lemma 8. *Suppose the conditions in Lemma 7 hold for matrices* $(A(t), P(t), \dot{P}(t))$. *Then, if* $A(t) = R^{-1}\tilde{A}(t)R$ *for a constant nonsingular matrix* R, *the conditions still hold for matrices* $(\tilde{A}(t), \tilde{P}(t), \dot{\tilde{P}}(t))$, *where*

$$\tilde{P}(t) := R^{-\intercal}P(t)R^{-1}, \qquad \dot{\tilde{P}}(t) := R^{-\intercal}\dot{P}(t)R^{-1}.$$

Proof. The first condition says

$$\begin{aligned}
A(t)^\intercal P(t) + P(t)A(t) + \dot{P}(t) &\geq \alpha(t)P(t), \\
R^{-\intercal}\Big(R^\intercal \tilde{A}(t)^\intercal R^{-\intercal} P(t) + P(t)R^{-1}\tilde{A}(t)R + \dot{P}(t) &\geq \alpha(t)P(t)\Big)R^{-1}, \\
\tilde{A}(t)^\intercal R^{-\intercal} P(t)R^{-1} + R^{-\intercal}P(t)R^{-1}\tilde{A}(t) + R^{-\intercal}\dot{P}(t)P^{-1} &\geq \alpha(t)R^{-\intercal}P(t)R^{-1}, \\
\tilde{A}(t)^\intercal \tilde{P}(t) + \tilde{P}(t)\tilde{A}(t) + \dot{\tilde{P}}(t) &\geq \alpha(t)\tilde{P}(t).
\end{aligned}$$

And the second condition is unchanged. □

We will now use this condition to design a controller $u(x)$ of the form in (4.3) to ensure that a desired solution of system (4.4) with the form in (4.5) is unstable.

4.3.3 Controller Design for Instability of a Desired Orbit

In order to use the conditions in Lemmas 7 and 8, we first linearize equation (4.4) about the orbit $(r, \theta) = (\mathbb{1}, \hat{\eta})$. Define

$$\rho := r - \mathbb{1}, \qquad \vartheta := \theta - \hat{\eta}, \qquad \hat{\eta} := t + \hat{\varphi}.$$

Linearizing the system around the solution $(\mathbb{1}, \hat{\eta})$, we obtain

$$\dot{w} = A(t)w, \qquad w := \begin{bmatrix} \rho \\ \vartheta \end{bmatrix}, \tag{4.9}$$

where

$$A(t) = \left(\begin{bmatrix} -2I & 0 \\ 0 & 0 \end{bmatrix} + \varepsilon \Omega_{\hat{\eta}}^\intercal H \Omega_{\hat{\eta}} \right), \qquad \Omega_z(t) := \begin{bmatrix} C_z & -S_z \\ S_z & C_z \end{bmatrix}.$$

Since the choice of $(r, \theta) = (\mathbb{1}, \hat{\eta})$ is a solution of system (4.1) when $u(x) = 0$, the coupling has to vanish on the target orbit for $(\mathbb{1}, \hat{\eta})$ to remain a solution of the coupled system. In that case, εH has to satisfy the following:

$$H\Omega_\varphi \begin{bmatrix} c_t \mathbb{1} \\ s_t \mathbb{1} \end{bmatrix} = 0, \qquad c_z := \cos(z), \qquad s_z := \sin(z). \tag{4.10}$$

Because the above has to hold true for all time t, the condition reduces to

$$\varepsilon H \Omega_\varphi \mathbb{1}_1 = 0, \qquad \varepsilon H \Omega_\varphi \mathbb{1}_2 = 0, \tag{4.11}$$

where $\mathbb{1}_1 := \mathrm{col}(0, \mathbb{1})$ and $\mathbb{1}_2 := \mathrm{col}(\mathbb{1}, 0)$. For an orbit with different amplitudes and oscillation frequency, similar but slightly more complicated conditions can be derived for εH to force the orbit to be a solution of the system.

Consider the linearized system in (4.9). We now design the coupling εH to ensure that a desired limit cycle at $(r, \theta) = (\mathbb{1}, \hat{\varphi} + t)$ will be an unstable solution of the system. The linearization about this orbit is given by (4.9) with $A(t)$ equal to

$$A(t) = \begin{bmatrix} -2I & 0 \\ 0 & 0 \end{bmatrix} + \varepsilon \Omega_t^\intercal \tilde{H} \Omega_t, \qquad \tilde{H} := \Omega_{\hat{\varphi}}^\intercal H \Omega_{\hat{\varphi}},$$

$$\Omega_t := \begin{bmatrix} c_t I & -s_t I \\ s_t I & c_t I \end{bmatrix}.$$

Let $\tilde{H}$ be described by the following block form:

$$\tilde{H} = \begin{bmatrix} \tilde{H}_{11} & \tilde{H}_{12} \\ \tilde{H}_{21} & \tilde{H}_{22} \end{bmatrix}.$$

Then, using Lemma 7, we can formulate conditions that ensure the instability of the limit cycle. This is summarized in the following Theorem.

Theorem 2. *If for some $v \in \mathbb{C}^n$ and $a \in \mathbb{C}$ with positive real part, the following conditions are satisfied,*

$$\begin{aligned} &\varepsilon \tilde{H} \mathbb{1}_1 = 0, \qquad && \varepsilon \tilde{H}_{11}^\intercal v = av, \qquad && \varepsilon \tilde{H}_{12}^\intercal v = 0, \\ &\varepsilon \tilde{H} \mathbb{1}_2 = 0, \qquad && \varepsilon \tilde{H}_{22}^\intercal v = av, \qquad && \varepsilon \tilde{H}_{21}^\intercal v = 0, \end{aligned}$$

then, for any controller of the form $u = \varepsilon H x$, with $H = \Omega_{\hat{\varphi}} \tilde{H} \Omega_{\hat{\varphi}}^\intercal$, the limit cycle described by $(r, \theta) = (\mathbb{1}, \hat{\varphi} + t)$ will be an unstable solution of system (4.4).

Proof. The first two conditions on the left correspond to the conditions in (4.11), which ensure that the desired limit cycle is a solution of the system. Define $\nu := \mathrm{col}(0, v)$, and set $P = \nu\nu^*$. Then, it can be shown that

$$A(t)^\intercal P + P A(t) \geq 2\Re(a) P.$$

According to Lemma 7, the above is a sufficient condition for $\lambda > \Re(a) > 0$. Therefore, the prescribed limit cycle will be an unstable solution of the system. $\square$

The conditions in Theorem 2 state that there exists a direction $\mathrm{col}(0, v)$ in which the desired orbit is unstable, with the magnitude of the instability described by the real part of a. While satisfying the conditions in Theorem 2 ensures the instability of the desired limit cycle, it does not guarantee that the limit cycle will be embedded in a strange attractor, and that the system will be chaotic. It is likely that the states will merely reach a different stable limit cycle. Thus, further conditions are needed to guarantee the instability of any other periodic orbit that is a solution of the system for a given coupling εH.

4.4 Coupling Design for Chaos Generation

In the previous section, we determined sufficient conditions that guaranteed the instability of a desired orbit with designable magnitudes and direction of instability. We now need to find additional conditions on the interconnections between the oscillators that will generate chaotic behavior, and guarantee that the trajectory will not reach a different stable periodic orbit. This is a very difficult problem, particularly since the system is very sensitive to the smallest variations in coupling. It turns out that a particular symmetric form of the coupling matrix εH can greatly simplify analytical study of the system. However, numerical analyses generally indicate that the symmetric form lacks the disorderliness that leads to chaos, and breaking the symmetry is suitable for generating chaotic behavior. We now look at these results.

4.4.1 Special Case of Symmetric Coupling

If the coupling matrix H can be expressed as H_S with the following symmetric structure:

$$H_S = \begin{bmatrix} H_{11} & H_{12} \\ -H_{12} & H_{11} \end{bmatrix}, \tag{4.12}$$

then, it is a special case where linearizing about any general sinusoidal solution $(r, \theta) = (\gamma, \omega t + \varphi)$, for $(\gamma, \omega, \varphi) \in \mathbb{R}^n \times \mathbb{R}^n \times \mathbb{R}^n$, will result in (4.9) with a time-invariant Jacobian

matrix A, given by

$$A = T^{-1}\hat{A}T, \qquad \hat{A} := \left(\begin{bmatrix} I - 3\Gamma^2 & -I + \mathcal{W} \\ I - \mathcal{W} & I - \Gamma^2 \end{bmatrix} + \varepsilon \hat{H} \right),$$

where

$$\hat{H} := \Omega_\varphi^\intercal H \Omega_\varphi, \qquad \Gamma := \mathrm{diag}(\gamma),$$
$$T := \mathrm{diag}(I, \Gamma), \qquad \mathcal{W} := \mathrm{diag}(\omega).$$

Since A is time invariant and is related to $\hat{A}$ through a similarity transform, the stability of the limit cycle is equivalent to $\hat{A}$ having one eigenvalue at the origin, and the rest in the open left half plane.

Conjecture 1. *Consider system (4.1) with $u(x)$ given by (4.3). For a sufficiently small ε, all possible stable sinusoidal solutions of the form $(r, \theta) = (\gamma, \omega t + \varphi)$ will have amplitudes and frequencies close to the nominal value of 1. Let $\mathcal{W}$ and Γ denote diagonal matrices of ω and γ, respectively. Then, matrices $(I - \mathcal{W})$ and $(I - \Gamma^2)$, will be small and of order ε.*

The argument behind this conjecture is as follows. Let $\xi(t) := \mathrm{col}(C_\theta \gamma, S_\theta \gamma)$ be a sinusoidal solution of (4.1) with $u(x) = \varepsilon H x$. Then, plugging $\xi(t)$ into (4.1) gives

$$(\mathcal{M}(\omega, \gamma) + \varepsilon H)\xi(t) = 0, \qquad \mathcal{M}(\omega, \gamma) := \begin{bmatrix} I - \Gamma^2 & -I + \mathcal{W} \\ I - \mathcal{W} & I - \Gamma^2 \end{bmatrix}.$$

Suppose there exists a solution $\xi(t)$ with some γ_k not close to 1. Let e_k be the k^{th} element of the identity matrix. Then, multiplying the equality above from the left by $\mathrm{col}(\gamma_k c_{\theta_k} e_k, \gamma_k s_{\theta_k} e_k)^\intercal$ simplifies to

$$\gamma_k^2(1 - \gamma_k^2) + \mathcal{O}(\varepsilon) = 0$$

Taking the limit of the above as $\varepsilon \to 0$ gives

$$\lim_{\varepsilon \to 0} \gamma_k^2(1 - \gamma_k^2) = 0.$$

Both $\gamma_k = 0$ and $\gamma_k = 1$ are solutions of the system when $\varepsilon = 0$. However, the former solution is an unstable equilibrium point. Based on continuity, we reason that all sinusoidal solutions

with amplitudes close to zero will remain unstable. Thus, the limit equality is only possible if $(1-\gamma_k^2)$ is of order ε. Because this contradicts the original assumption, $(I-\Gamma^2) \sim \mathcal{O}(\varepsilon)$ must hold. A similar argument can be made for ω_k by multiplying the initial equality from the left by $\text{col}(-\gamma_k s_{\theta_k} e_k, \gamma_k c_{\theta_k} e_k)^\intercal$.

Lemma 9. *For a small enough ε, if trace$(I-\Gamma^2+\varepsilon H/2) > 0$, then $\hat{A}$ will have at least one eigenvalue with a positive real part.*

Proof. According to Conjecture 1, $\varepsilon\hat{H}$, $(I-\mathcal{W})$ and $(I-\Gamma^2)$ are all of order ε. As a result, $\hat{A}$ can be represented by

$$\hat{A} = \begin{bmatrix} \hat{A}_{11} & \varepsilon\hat{A}_{12} \\ -\varepsilon\hat{A}_{12} & \varepsilon\hat{A}_{22} \end{bmatrix},$$

which is similar to

$$\begin{bmatrix} \hat{A}_{11}+\varepsilon\hat{A}_{12}X & \varepsilon\hat{A}_{12} \\ 0 & \varepsilon\hat{A}_{22}-\epsilon X\hat{A}_{12} \end{bmatrix},$$

where X is the solution to the following matrix Riccati equation [90]

$$-\varepsilon\hat{A}_{12} - X\hat{A}_{11} + \varepsilon\hat{A}_{22}X - \varepsilon X\hat{A}_{12}X = 0.$$

We would like to see if there is a relationship between X and ϵ. Since $(I-\Gamma^2)$ is small and of order ε, $\hat{A}_{11}$ is clearly invertible. If we take the limit of the norm of the above as $\varepsilon \to 0$, we get

$$\lim_{\varepsilon\to 0} ||-\varepsilon\hat{A}_{12} - X\hat{A}_{11} + \varepsilon\hat{A}_{22}X - \varepsilon X\hat{A}_{12}X|| = \lim_{\varepsilon\to 0} ||X\hat{A}_{11}|| = 0.$$

Since $\hat{A}_{11}$ is invertible, and X is non-zero in general, we can conclude that

$$\lim_{\varepsilon\to 0} ||X|| \to 0.$$

Then, for small enough ε, the eigenvalues of $\hat{A}$ can be approximated by the eigenvalues of $\hat{A}_{11}$ and $\varepsilon\hat{A}_{22}$. Then, trace$(\hat{A}_{22}) > 0$ is a sufficient condition for $\hat{A}$ having an eigenvalue in the right half plane. Using simple trace properties, it can be shown that trace$(\hat{A}_{22}) =$ trace$(I-\Gamma^2+\varepsilon H/2)$. □

The periodic orbit $(r,\theta)=(\gamma,\omega t+\varphi)$ is a solution of the system if and only if

$$\left(\begin{bmatrix} I-\Gamma^2 & -I+\mathcal{W} \\ I-\mathcal{W} & I-\Gamma^2 \end{bmatrix}+\varepsilon H\right)\begin{bmatrix}\Gamma & 0\\ 0 & \Gamma\end{bmatrix}\begin{bmatrix}C_\varphi \mathbb{1}\\ S_\varphi \mathbb{1}\end{bmatrix}=0. \tag{4.13}$$

If we define $\mathfrak{x}:=\mathrm{col}(C_\varphi\gamma, S_\varphi\gamma)$, then (4.13) can be expressed as

$$F(\mathfrak{x},w)\mathfrak{x}=0, \tag{4.14}$$

where

$$w:=-\mathbb{1}+\omega,\qquad \Gamma_{ii}^2=\mathfrak{x}_i^2+\mathfrak{x}_{n+i}^2,\qquad F(\mathfrak{x},w):=\left(\begin{bmatrix} I-\Gamma^2 & \mathrm{diag}(w)\\ -\mathrm{diag}(w) & I-\Gamma^2\end{bmatrix}+\varepsilon H\right).$$

We would like to set a condition that ensures that for a given H, there is no stable sinusoidal solution of the form $(r,\theta)=(\gamma,\omega t+\varphi)$. This means that if a choice of (γ,ω,φ) satisfies (4.13), then the Jacobian A matrix will have at least one eigenvalue with a positive real part. For sufficiently small ε, we can approximate the eigenvalues of A by the eigenvalues of $\hat{A}_{11}$ and $\epsilon\hat{A}_{22}$. A suitable sufficient condition to ensure the instability of the linearized system, is $\mathrm{trace}(\epsilon\hat{A}_{22})>0$. In the original variables, this condition is equivalent to

$$\mathrm{trace}\Big(I-\Gamma^2+\varepsilon(S_\varphi H_{11}S_\varphi+C_\varphi H_{11}C_\varphi+C_\varphi H_{12}S_\varphi-S_\varphi H_{12}C_\varphi)\Big)>0,$$

which simplifies to

$$n-\mathfrak{x}^\intercal\mathfrak{x}+\varepsilon\mathrm{trace}(H/2)>0. \tag{4.15}$$

The condition above guarantees the instability of a specific harmonic form where each oscillator has the same amplitude, frequency and phase for both of its states. It can be shown that this form of $x(t)=\mathrm{col}(C_\theta\gamma, S_\theta\gamma)$ is the only possible sinusoidal solution.

Lemma 10. *Consider system (4.1) with $u(x)$ given by (4.3). Then, all possible sinusoidal solutions, with constant frequencies, phases, and amplitudes, are of the form*

$$x(t)=\begin{bmatrix}C_\theta\gamma\\ S_\theta\gamma\end{bmatrix},\qquad \theta:=\omega t+\varphi. \tag{4.16}$$

Proof. Suppose a solution is given of the form $x(t) = \text{col}(q(t), p(t))$, where $q(t)$ and $p(t)$ are arbitrary sinusoidal functions with frequency ω. Define the vector $\hat{x}_i := \text{col}(q_i e_i, p_i e_i)$, where e_i is the i^{th} column of the n dimensional identity matrix. Then, multiplying (4.1) by $\hat{x}_i^{\mathsf{T}}$ from the left gives

$$\frac{1}{2}\frac{d}{dt}(p_i^2 + q_i^2) = p_i^2 + q_i^2 - (p_i^2 + q_i^2)^2 + \hat{x}_i^{\mathsf{T}} H x.$$

If $(q_i^2 + p_i^2)$ is not equal to a constant, but is a sinusoidal function with frequency 2ω, then the right hand side will have a harmonic term with frequency 4ω coming from the $(p_i^2 + q_i^2)^2$ term. However, this term cannot cancel any term from the left side, resulting in an inconsistency. □

We will now summarize the conditions on εH that guarantee the nonexistence of any stable sinusoidal solution in the following Theorem.

Theorem 3. *Consider system (4.1) with $u(x)$ given by (4.3), where the coupling matrix H has the structure in (4.12). Suppose general multipliers $\mathfrak{y} \in \mathbb{R}^{2n}$ and $\mathcal{Z} \in \mathbb{R}^{2n \times 2n}$ exist such that the following condition is satisfied for all $\mathfrak{x}$ and w:*

$$n - \mathfrak{x}^{\mathsf{T}}\mathfrak{x} + \varepsilon \, trace(H/2) > (\mathfrak{y} + \mathcal{Z}\mathfrak{x})^{\mathsf{T}} F(\mathfrak{x}, w)\mathfrak{x}. \tag{4.17}$$

Then, for a small enough ε, no trajectory of system (4.1) will reach a stable sinusoidal solution of the form in (4.16) with $(\omega_i - 1)$ and $(\gamma_i - 1)$ of order ε for $i = 1, ..., n$.

Proof. $(r, \theta) = (\gamma, \omega t + \varphi)$ is a stable solution of the system if it satisfies (4.14) and all the eigenvalues of $\hat{A}$ are on the closed left half plane. Thus, if all $(\mathfrak{x}, w)$ that satisfy (4.14) also satisfy (4.15), then that's a sufficient condition that they are unstable solutions of the system. (Note that (4.15) is only a sufficient condition under Conjecture 1, when $(\omega_i - 1)$ and $(\gamma_i - 1)$ are of order ε for $i = 1, ..., n$.) This is captured in the following statement:

$$n - \mathfrak{x}^{\mathsf{T}}\mathfrak{x} + \varepsilon \text{trace}(H/2) > 0 \qquad \forall (\mathfrak{x}, w) \qquad \text{s.t.} \qquad F(\mathfrak{x}, w)\mathfrak{x} = 0.$$

Finally, the S-procedure is used to convert the above to one sufficient condition using multipliers $\mathfrak{y}$ and $\mathcal{Z}$. □

We can now use the specifications in Theorems 2 and 3 to find a coupling matrix εH that guarantees the instability of a desired limit cycle with a designable instability magnitude and direction, as well as the nonexistence of any other stable sinusoidal solution. However, if H has been chosen to satisfy the properties in Theorem 2, then an unstable solution described by $\hat{\mathfrak{x}} := \mathrm{col}(C_{\hat{\varphi}}\mathbb{1}, S_{\hat{\varphi}}\mathbb{1})$ exists that may not satisfy the sufficient condition in (4.15). Therefore, another condition needs to be added to eliminate $\mathfrak{x} = \hat{\mathfrak{x}}$. Furthermore, an upper bound on the absolute values of the elements of w, which are assumed to be of order ε, can improve the numerical feasibility of the condition. With these additional constraints, we can reformat (4.17) to the following condition

$$n - \mathfrak{x}^{\mathsf{T}}\mathfrak{x} + \varepsilon \mathrm{trace}(H/2) > (\mathfrak{y} + \mathcal{Z}\mathfrak{x})^{\mathsf{T}} F(\mathfrak{x}, w)\mathfrak{x} + \sum_{i=1}^{n} \zeta_i (c\varepsilon - w_i^2) + \varrho(||\mathfrak{x} - \hat{\mathfrak{x}}||^2 - \delta), \qquad (4.18)$$

where $\zeta \in \mathbb{R}^n$ and $\varrho \in \mathbb{R}$ are positive multipliers, $\delta \ll \varepsilon$ is a small, positive number close to zero, and c is some constant that enforces the elements of w to be of order ε.

The conditions in Theorem 2 are linear and easy to solve numerically. However, the one in Theorem 3, or (4.18), is nonlinear and involves the multiplication of multipliers $\mathfrak{y}$ and $\mathcal{Z}$ with εH. To circumvent this complexity, an iterative algorithm can be used in order to find numerical solutions. A summary of this iteration technique will be discussed in the next section.

4.4.2 Symmetry Breaking and Additional Conditions for Chaos Generation

In the previous sections we determined specifications on the coupling εH that ensured that no stable sinusoidal orbit was a solution of the system. However, these conditions are not sufficient for chaos generation, as they do not eliminate the existence of more complex harmonic orbits. In particular, when H has the symmetric form of H_S, it could create undesired order amongst the oscillators. Based on considerable numerical examples, we speculate that system (4.1) can rarely generate chaotic behavior when the interconnections have the symmetric form in (4.12), and symmetry breaking is significant for increased disorder.

To maintain the specifications that have been satisfied in Theorems 2 and 3, we break

symmetry by choosing the following form for the coupling matrix H:

$$H = \Omega_{\hat{\varphi}} \begin{bmatrix} \tilde{H}_{11} & (1+e)\tilde{H}_{12} \\ (-1+e)\tilde{H}_{12} & \tilde{H}_{11} \end{bmatrix} \Omega_{\hat{\varphi}}^{\intercal}, \tag{4.19}$$

where the conditions in Theorems 2 and 3 have been satisfied for $e = 0$. It is clear that for any value of e, the specifications in Theorem 2 still hold; however, this is not necessarily true for the latter theorem. Therefore, we make the following assumption:

Assumption 2. *Consider system (4.1) with $u(x)$ given by (4.3) and H given by (4.19). If for $e = 0$, the coupling εH satisfies the conditions in Theorem (3), then for sufficiently small e, all possible harmonic solutions of system (4.1) will remain unstable.*

Although the variation of the coupling matrix with a nonzero e can increase disorder, it is still not a sufficient condition for the existence of a chaotic strange attractor. Unfortunately, determining an analytical sufficiency condition for chaos generation, without the need for numerical simulations and tuning, is extremely difficult. It is especially challenging when the controller is linear and does not contain particular nonlinearities, such as nonlinear delay feedback or sawtooth functions. Hence, we progress this study by finding additional properties that are generally satisfied in chaotic numerical examples, and can be formulated as an analytical condition on the controller.

In Section 4.3, we noted that chaotic systems generally have positive and negative Lyapunov exponents. While the positive Lyapunov exponent indicates sensitivity to initial conditions, the negative exponent indicates that the trajectory returns to a previous vicinity, resulting in a stable strange attractor. In fact, the strangeness of an attractor can generally be classified by a non-integer Kaplan-Yorke dimension, which can only occur with the existence of a negative Lyapunov exponent [91].

In our system, we expect that with weak coupling, all n amplitude states of a general trajectory will remain stable and lead to n negative Lyapunov exponents. However, we want one Lyapunov exponent, corresponding to the oscillators' phases, to be positive, one to be zero, and for all others to be negative. Numerical evidence indicates that this is more achievable when the trajectories in the strange attractor continuously approach and leave the

vicinity of the desired unstable orbit $\hat{\xi}(t)$. Because we do not want to rely on any conditions that involve numerical simulations, we require a simple, linear property that would indicate the above. We hypothesize that the time-invariant Jacobian A matrix, linearized about $\hat{\xi}(t)$ in (4.9) with symmetric H, should have only one eigenvalue in the right half plane, one at the origin, and all others on the open left half plane. Based on the proof of Lemma 9, n eigenvalues of A are approximately equal to the eigenvalues of $\varepsilon\tilde{H}_{11}$. As a result, $\tilde{H}_{11}$ should have only one positive eigenvalue. This can be converted to a restriction on the trace of the coupling matrix H.

Numerical case studies have also indicated that it is easier to generate chaotic behavior when the off diagonal block $\tilde{H}_{12}$ is large. However, because our specifications in Theorem 3 are made for small εH, there is a limit on how strong $\tilde{H}_{12}$ can be before our assumptions are broken. We will now summarize the steps in the iteration algorithm that can be used to numerically solve the conditions in Theorems 2 and 3.

Iteration Algorithm: Consider the condition given in (4.18), with the additional positive multipliers multiplying constraints on the $c\varepsilon$ bound of $||w_i||$ and $||\mathfrak{x}-\hat{\mathfrak{x}}|| > 0$. Define a variable $\beta \in \mathbb{R}$ and add it to the right hand side of (4.18) to get

$$n - \mathfrak{x}^{\intercal}\mathfrak{x} + \varepsilon \text{trace}(H/2) > (\mathfrak{y} + \mathcal{Z}\mathfrak{x})^{\intercal} F(\mathfrak{x}, w)\mathfrak{x} + \sum_{i=1}^{n} \zeta_i (c\varepsilon - w_i^2) + \varrho(||\mathfrak{x}-\hat{\mathfrak{x}}||^2 - \delta) + \beta, \quad (4.20)$$

Select desired values of $(\hat{\varphi}, v, a)$ for the conditions in Theorem 2. Note that it is also possible to allow a to vary within a small range of positive values in order to increase the numerical feasibility and speed of the algorithm. Finally, choose a suitable starting value for the coupling matrix $\varepsilon_o H_o$, an upper bound for its trace h_f, and an initial $\beta_o < 0$. The pseudocode of the two-step decay algorithm is then given as follows:

- while $(\beta_o \leq 0)$ or $(\text{trace}(\varepsilon_o H_o) > h_f)$
  - maximize β over $(\mathfrak{y}, \mathcal{Z}, \zeta, \varrho, \beta)$ subject to condition (4.20) for all $\mathfrak{x} \in \mathbb{R}^{2n}$ and $w \in \mathbb{R}^n$, and positivity of ϱ and all elements of ζ, with $\varepsilon H = \varepsilon_o H_o$
  - define $(\mathfrak{y}_o, \mathcal{Z}_o, \zeta_o, \varrho_o, \beta_o)$ as $(\mathfrak{y}, \mathcal{Z}, \zeta, \varrho, \beta)$ from the previous step

- minimize trace(εH) over $(\varepsilon H, a)$ subject to the conditions in Theorem 2, condition (4.20) for all $\mathfrak{x} \in \mathbb{R}^{2n}$ and $w \in \mathbb{R}^n$, desired bounds on a, and bounds on the elements of εH being small, with $(\mathfrak{y}, \mathcal{Z}, \zeta, \varrho, \beta) = (\mathfrak{y}_o, \mathcal{Z}_o, \zeta_o, \varrho_o, \beta_o)$
- redefine $\varepsilon_o H_o$ as the new εH from the previous step

• end

For the examples given in Section 4.5, each optimization step was formulated with SOSTOOLS, a free MATLAB toolbox for formatting sum of squares optimization problems. The problems were then solved using SeDuMi, a well-known program that solves optimizations over linear, quadratic, and semidefinite constraints.

4.5 Numerical Examples

In the following numerical analyses, a set of three coupled Andronov-Hopf oscillators, with their dynamics described by (4.1), are considered. For each example, the controller has the linear form in (4.3), where the coupling matrix εH satisfies all the conditions in Theorems 2 and 3, as well as the additional conditions from Section 4.4.2. However, each case considers a different desired unstable limit cycle, of the form in (4.5), to be embedded in a strange attractor, with a different instability direction v. The results of these examples demonstrate both the effectiveness and the deficiencies of the theory presented in this chapter. Notably, we witness the sensitivity of the oscillators' dynamics to the slightest variations in their interconnections. This sensitivity is particularly disadvantageous as we lack a complete analytical condition that guarantees chaos generation.

4.5.1 Example I

In this example, we first find a numerical coupling matrix εH, with the symmetric form in (4.12), that satisfies the conditions in Theorems 2 and 3, for the following specifications:

$$\hat{\varphi} = \mathrm{col}(0, \pi/2, \pi), \qquad 0.05 \leq a \leq 0.15, \qquad v = \mathrm{col}(1, -2, 1)/\sqrt{6}.$$

We allow the magnitude of instability a to be within a range of small values in order to improve feasibility and speed of convergence in the decay iteration process. Using the form in (4.19), a possible interconnection matrix εH is found, with the following eigenvalues:

$$\text{eig}(\varepsilon H) = (0.12, 0.12, 0, 0, -0.08 \pm 0.39).$$

Note that because of the structure of H, all eigenvalues are either repeated or complex conjugates. Furthermore, there is only one pair of positive eigenvalues. One eigenvalue of

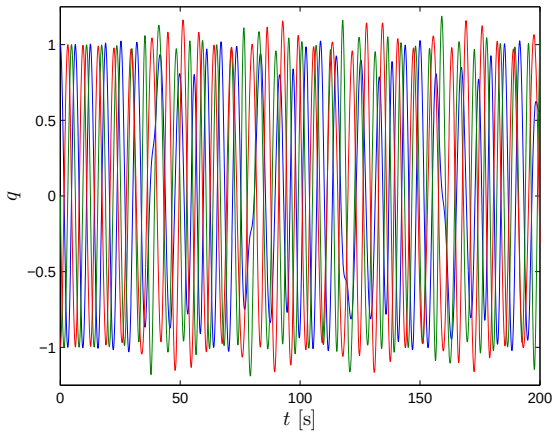

(a) Time plot of the oscillators' first states

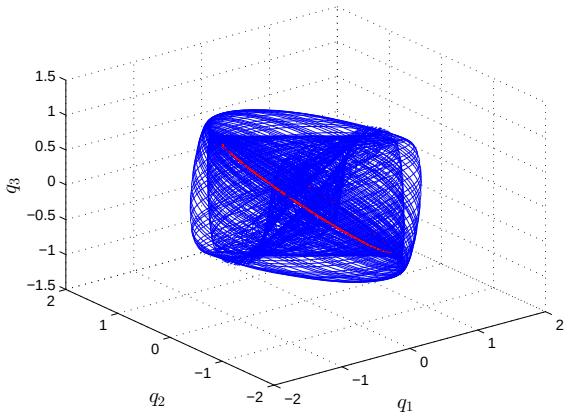

(b) Phase plot of the oscillators' first states

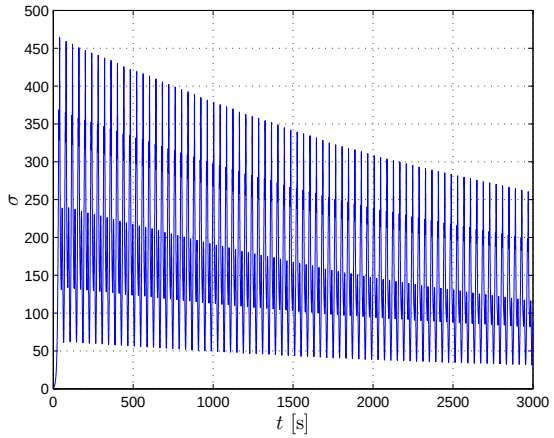

(c) Plot of the maximum singular value of the state transition matrix of system 4.6

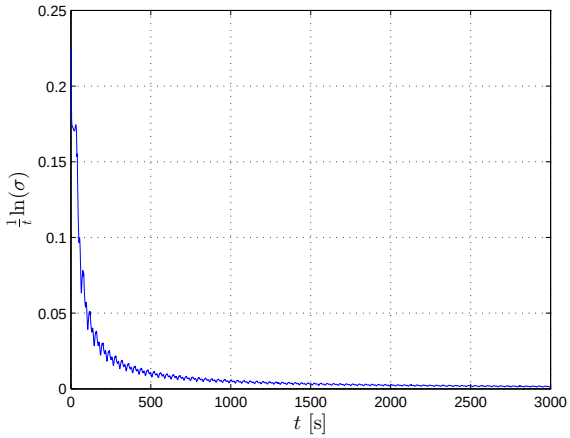

(d) Plot of the maximum Lyapunov exponent

Figure 4.1: Simulation results of Example I for $e = 0$

the pair corresponds to the desired a value, while the other becomes a negative eigenvalue of the Jacobian A matrix due to the $-2I$ term. This also occurs with the other pairs of eigenvalues, such that A will contain one positive eigenvalue, one zero eigenvalue, and all others in the open left half plane.

Figure 4.1 shows the results of the system simulation for $e = 0$, with the initial conditions close to the desired unstable orbit. Note that we only plot the first state of the oscillators, represented by $q(t)$. As expected, the trajectory continuously leaves and returns to the

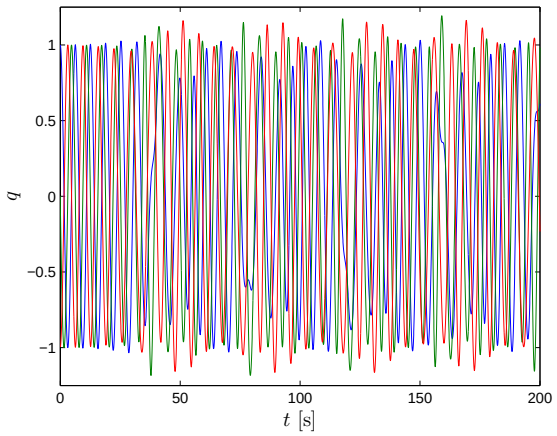

(a) Time plot of the oscillators' first states

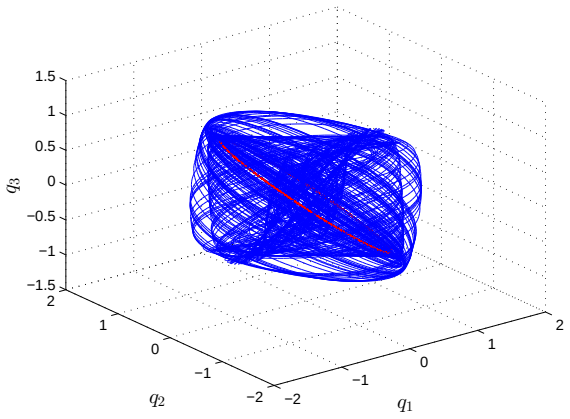

(b) Phase plot of the oscillators' first states

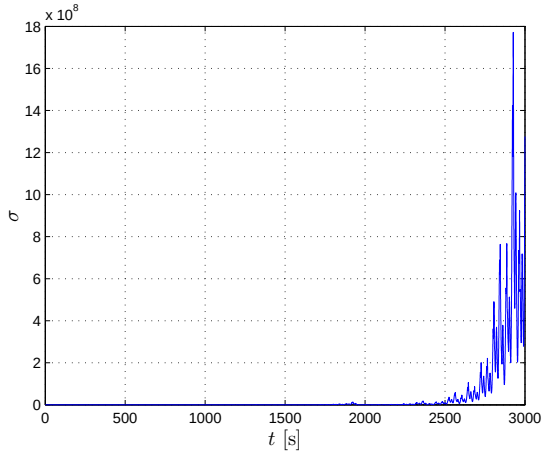

(c) Plot of the maximum singular value of the state transition matrix of system 4.6

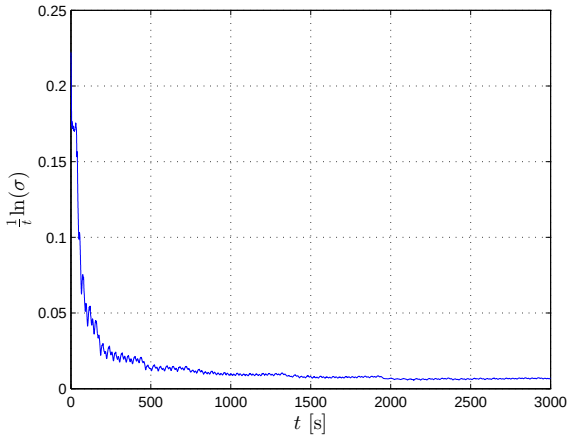

(d) Plot of the maximum Lyapunov exponent

Figure 4.2: Simulation results of Example I for $e = 0.15$

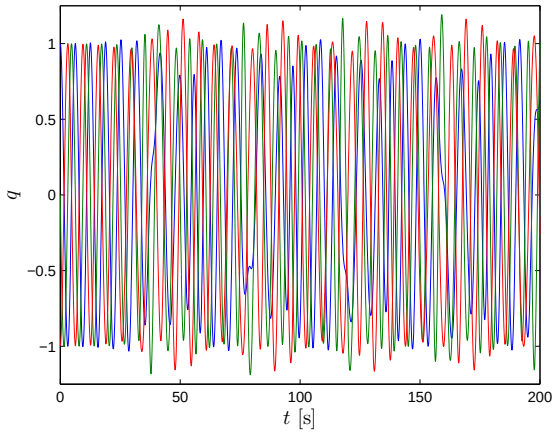

(a) Time plot of the oscillators' first states

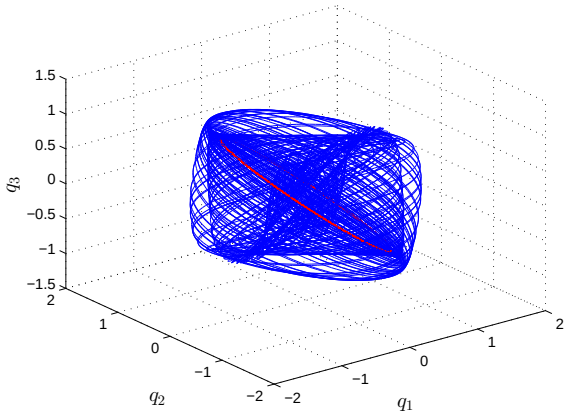

(b) Phase plot of the oscillators' first states

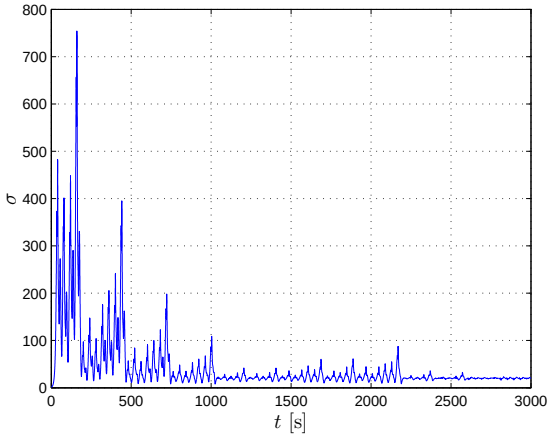

(c) Plot of the maximum singular value of the state transition matrix of system 4.6

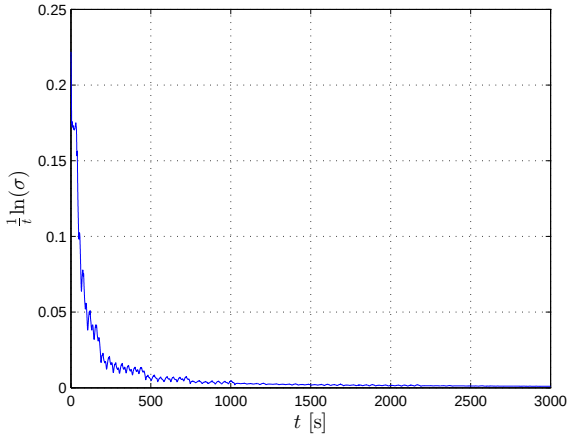

(d) Plot of the maximum Lyapunov exponent

Figure 4.3: Simulation results of Example I for $e = 0.1$

unstable orbit, but never settles at a stable harmonic limit cycle. This is shown in Figure 4.1a in the time domain, and in Figure 4.1b in the phase plane, with the red orbit indicating $(r, \theta) = (\mathbb{1}, t + \hat{\varphi})$. However, the resulting attractor is not chaotic and is not sensitive to initial conditions. Figure 4.1c shows the plot of the maximum singular value of the state transition matrix of the linearized system (4.6). Because σ is not exponentially growing, the maximum Lyapunov exponent, or the limit of the plot in Figure 4.1d, is zero.

Figure 4.2 shows the simulation results when symmetry is broken by setting $e = 0.15$.

The symmetry breaking increases the disorder such that the trajectory becomes chaotic and sensitive to initial conditions. In this case, σ is exponentially growing, as seen in Figure 4.2c, and the maximum Lyapunov exponent is approximately 0.007. The significant difference in the behaviors of these two trajectories, with $e = 0$ versus $e = 0.15$, is not particularly visible in the time domain. A comparison of the phase plots of $q(t)$, given in Figures 4.1b and 4.2b, indicates that a chaotic strange attractor possibly occupies a smaller volume of space. However, we still lack a complete condition to help us determine a value of e. For instance, when e is decreased to $e = 0.1$, chaotic behavior disappears and the maximum Lyapunov exponent again reaches zero. This is seen in Figures 4.3c and 4.3d. But again, the time and phase plots of $q(t)$, shown in Figures 4.3c and 4.3d, look almost identical to the case with $e = 0.15$. As a result, it is still impossible to classify the system's behavior without calculating the maximum Lyapunov exponent.

4.5.2 Example II

In this example, we again find a numerical coupling matrix εH, with the symmetric form in (4.12), that satisfied the conditions in Theorems 2 and 3, for the following specifications:

$$\hat{\varphi} = \text{col}(0, \pi/2, \pi/4), \qquad 0.05 \leq a \leq 0.15, \qquad v = \text{col}(1, 1, -2)/\sqrt{6}.$$

Using the form in (4.19), a possible interconnection matrix εH is found, with the following eigenvalues:

$$\text{eig}(\varepsilon H) = (0.079, 0.079, 0, 0, -0.063 \pm 0.39).$$

The results of the system simulation for $e = 0$ are shown in Figure 4.4, with the initial conditions close to the desired unstable orbit. Similar to Example I, the trajectory continuously leaves and returns to the unstable orbit, but never settles at a stable harmonic limit cycle. This is shown in Figures 4.1a and 4.1b for $q(t)$. Like the previous example, the strange attractor is not chaotic in the symmetric case when $e = 0$. Figure 4.1c shows the plot of σ, which is not exponentially growing; thus, the maximum Lyapunov exponent, or the limit of the plot in Figure 4.1d,is zero.

Figure 4.5 shows that the disorder and the maximum Lyapunov exponent can be increased

when symmetry is broken by setting $e = 0.15$. In this case, the maximum Lyapunov exponent increases to 0.013, Figure 4.5d. A comparison of the phase plots of $q(t)$, given in Figures 4.5b and 4.4b, indicates again that a chaotic strange attractor, with a larger maximum Lyapunov exponent, occupies a smaller volume of space.

While this system is not quite as sensitive to small perturbations in e as the system in Example I, it is sensitive to small perturbations in the norm of the coupling matrix εH. For example, when we decrease the norm by 8%, with $e = 0.15$, the exponential growth of σ

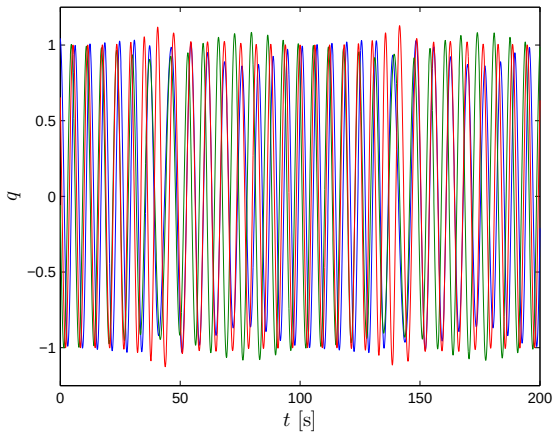

(a) Time plot of the oscillators' first states

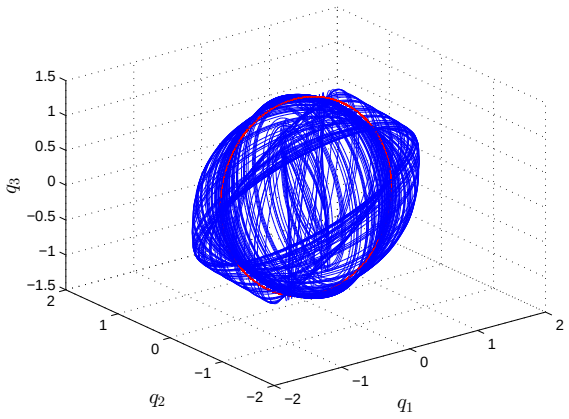

(b) Phase plot of the oscillators' first states

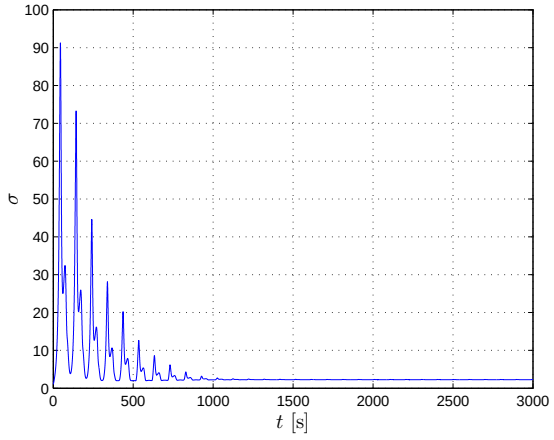

(c) Plot of the maximum singular value of the state transition matrix of system 4.6

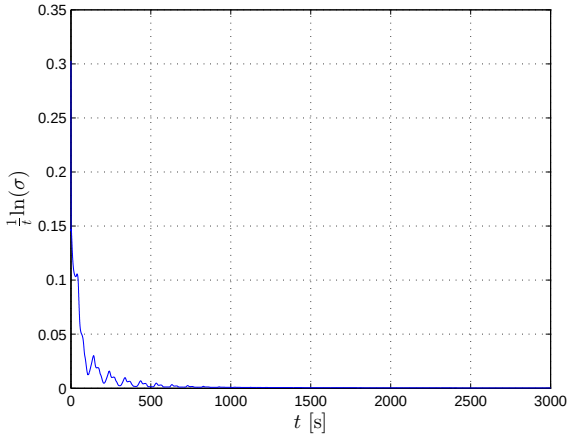

(d) Plot of the maximum Lyapunov exponent

Figure 4.4: Simulation results of Example II for $e = 0$

disappears and the maximum Lyapunov exponent becomes zero. This is seen in Figure 4.6.

While this section has only presented two numerical examples, we believe that these cases have demonstrated the effectiveness of our developments, as well as the difficulties of satisfying the objective. For both examples, we were able to generate desired chaotic behavior with variations in a small parameter. However, while the shape of the strange attractor remained fairly similar, sensitivity to initial conditions was not robust, such that parameter tuning became reliant on numerical simulations.

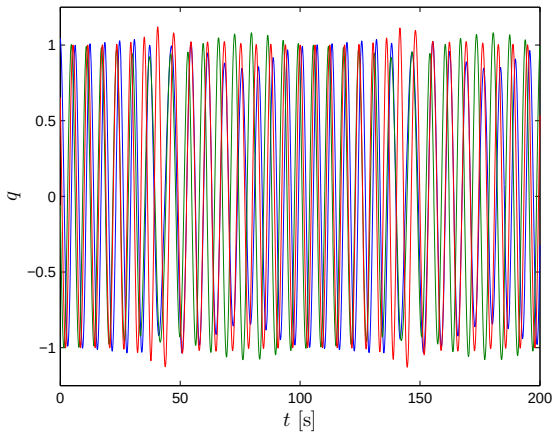

(a) Time plot of the oscillators' first states

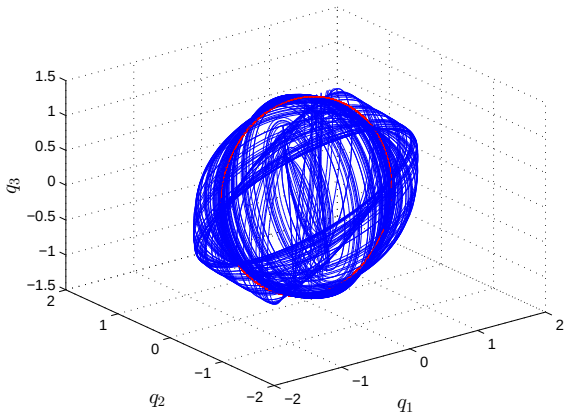

(b) Phase plot of the oscillators' first states

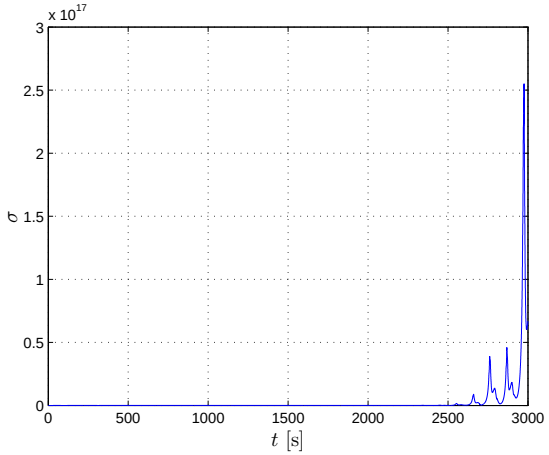

(c) Plot of the maximum singular value of the state transition matrix of system 4.6

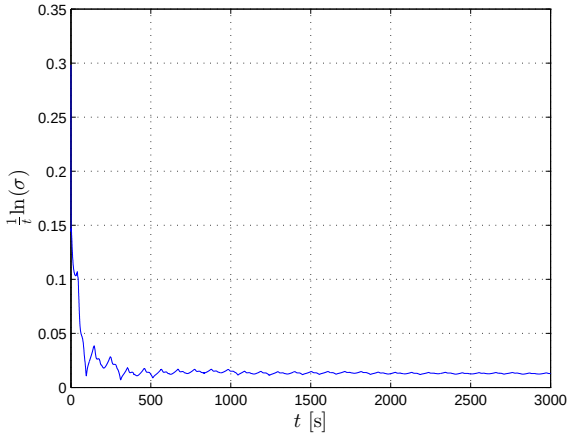

(d) Plot of the maximum Lyapunov exponent

Figure 4.5: Simulation results of Example II for $e = 0.15$

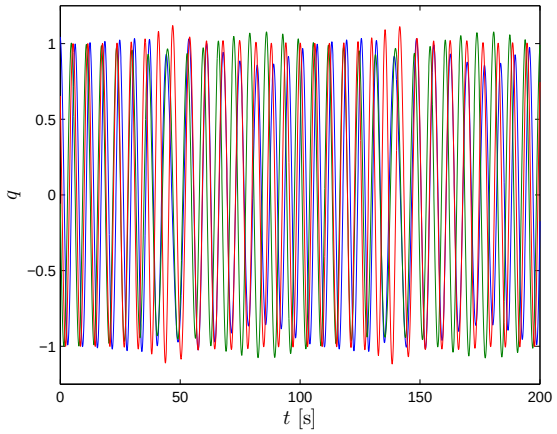

(a) Time plot of the oscillators' first states

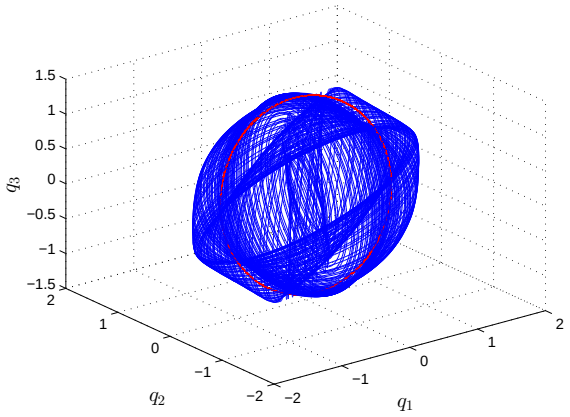

(b) Phase plot of the oscillators' first states

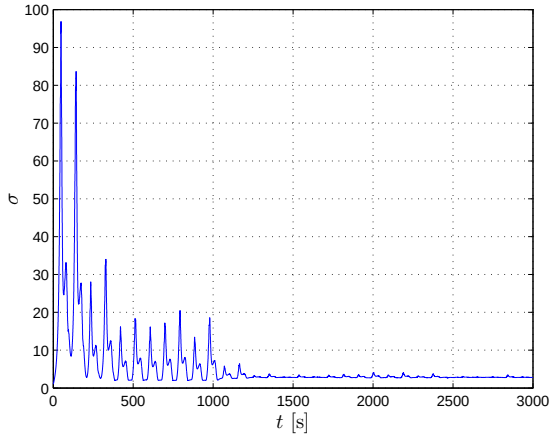

(c) Plot of the maximum singular value of the state transition matrix of system 4.6

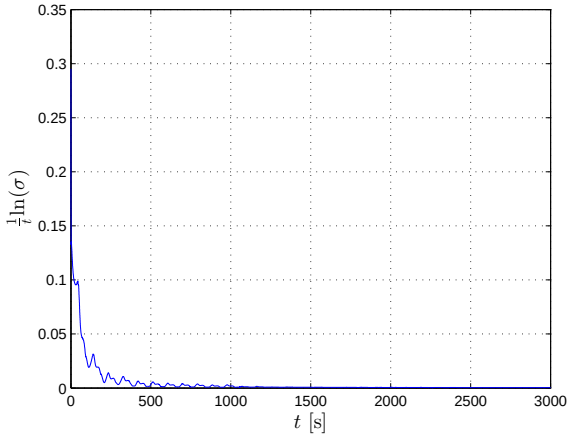

(d) Plot of the maximum Lyapunov exponent

Figure 4.6: Simulation results of Example II for $e = 0.15$ with ε reduced by 8%

4.6 Discussion

The design of a network of coupled oscillators, whose collective behavior is characterized by a chaotic strange attractor, is a challenging problem. Previous efforts have either included complex nonlinearities, such as time delays, or parameter tuning using numerical simulations. Our objective in this chapter was to determine sufficiency conditions on the oscillators' interconnections that would accomplish the objective without the need for numerical simulations and calculating Lyapunov exponents. For this task, we considered a set of

two dimensional Andronov-Hopf oscillators, where the internal structure, without coupling, stabilizes the oscillators' frequency and amplitude. We then set out to design weak, linear coupling between the oscillators such that the system dynamics would characterize a chaotic strange attractor, with a desired unstable orbit embedded in the attractor.

The first main contributions of this chapter was developing simple eigenvalue/eigenvector conditions on the coupling matrix that forced a desired harmonic orbit to be an unstable solution of the system with a specified magnitude and direction of instability. The second main contribution was determining a specific symmetric structure for the coupling matrix that greatly simplified system analysis. Specifically, with the particular symmetric coupling, linearizing the system about all simple harmonic solutions resulted in a time-invariant Jacobian matrix. Using this property and the S-procedure, we developed a condition that ensured no harmonic orbit would be a stable solution of the system. Finally, using numerical analyses of chaotic systems, we determined several additional factors that we hypothesize can assist in stabilizing a strange attractor and increasing disorder and sensitivity to initial conditions.

Our numerical examples demonstrated that satisfying the conditions can lead to a system which generates the desired behavior; however, it still requires parameter tuning. In particular, we witnessed that the chaotic strange attractors are not robust and are sensitive to small parameter changes. Although the work of this chapter did not conclude with a completed sufficiency condition that solved the objective, we believe our results have set the groundwork for a final solution.

CHAPTER 5

Conclusion

This research has centered on the design and analysis of complex dynamic behaviors inspired by those observed in biological systems. Specifically, this study has focused on the generation of period oscillations in animal locomotion and chaotic behavior in neural networks, such as those located within the central pattern generator (CPG). It has been shown in the literature that animal locomotion is energy efficient and adaptable to environmental changes. This adaptability is likely related to the flexibility of the intrinsic chaotic behavior in the CPG. Broadly speaking, the motivation of this research is to be able to create robotic locomotors that posses the same desirable properties as their biological counterparts.

In Chapter 2 of this dissertation, we considered a general multi-body mechanical rectifier traveling in three dimensional space, subject to continuous environmental forces. We developed a functional model for the locomotor in the body frame, and formulated and solved an optimal turning gait problem that minimizes a quadratic cost function while satisfying desired translational and angular velocities. Our results showed that the problem can be reduced to two simpler minimization problems, where the body shape offset for turning can be found independently from the periodic body motion resulting in straight locomotion. A numerical case study of an H-swimmer was then presented to demonstrate the functionality of the optimal turning gait theory. The results showed that the simplified model and the optimal gait theory are practical in finding gaits that can achieve desired trajectory and speed for the fully nonlinear model.

The purpose of Chapter 3 was to utilize the optimal gait theory in order to investigate essential questions in biological locomotion. In particular, the study focused on the questions of why Carangiform fish swim at a particular frequency and why the Strouhal number remains

approximately constant over all speeds. In order to answer these questions, we developed a simplified model for saithe fish that captured the essential dynamics of locomotion. Our results indicated that the optimal periodic motion which minimizes muscle tension or bending moment closely matches observed swimming, and can explain the observed tendency of increasing tail-beat frequency and stiffness to achieve higher velocities, while maintaining constant tail amplitude. This also answers why the Strouhal number remains constant over all swim speeds and frequencies. Furthermore, the optimal frequency is equivalent to the resonance which maximizes the ratio of tail-tip velocity to bending moment; this resonance results from both the body resonance and the fluid resonance.

The purpose of Chapter 4 was to determine conditions on the interconnections within a neural network in order to generate desired chaotic behavior. To achieve this goal, we required a neural model that was simple enough for analytical study, but could capture a wide variety of complex behaviors. To that end, we decided to model the neural network as a set of two dimensional Andronov-Hopf oscillators with linear coupling. In particular, we considered the case where the coupling between the oscillators is weak enough to maintain amplitude stability, while destabilizing the phase differences. First, we found properties that guaranteed the instability of a desired limit cycle with the ability to design the instability direction and magnitude. We then considered a special case of symmetric coupling and determined a condition that ensured no other harmonic limit cycle would be a solution of the system. Through considerable numerical evidence, we noted a few suppositions, including symmetry breaking, that appear to increase disorder and sensitivity to initial conditions. Finally, we presented two numerical case studies that demonstrated the utility and shortcomings of our results.

The results of this research can be expanded in several different directions. One major project is to use the coupled oscillators for feedback control of a mechanical rectifier, in order to drive the locomotor to the desired oscillation profile(s). We anticipate that the chaotic nature of the neural network will have the adaptability and flexibility to readily switch between multiple gaits through environmental changes. Achieving this task requires solving several major steps. First, the independent chaotic neural network needs to be designed such

that the desired oscillation profiles are embedded in the strange attractor. This research only considered the case for one desired orbit; however, this needs to be expanded to multiple orbits in order to achieve flexible gait switching. Then, the input and output gains for the plant and the controller need to be designed such that the closed loop system trajectory will reach the desired stable oscillation.

Other directions for the continuation of this research include applying the theoretical results for the study of biological systems. One example of this was shown in Chapter 3, where the optimal gait theory was used to analyze observed swimming of saith fish. However, this can be be expanded further. For example, the mathematical tools developed in Chapter 4 on chaos generation in neural networks can be used to analyze the central pattern generators of healthy individuals versus those suffering from Parkinson's disease or epileptic seizures. It may be possible to find analytical justifications for the hypothesis that chaotic behavior is necessary for healthy motor function, while regular rhythmic behavior can result in movement disorders. We hope that the results of this dissertation will provide effective stepping stones for these larger scientific endeavors.

APPENDIX A

Modeling Details for Mechanical Rectifiers

A.1 Modeling details and definitions of coefficient matrices in (2.4)

This section of the Appendix provides details on the rectifier modeling. The rectifier is formed by a set of κ rigid bodies connected to each other in three dimensional space. In the development of the equations of motion, subscript i for a quantity refers to that quantity with respect to body i, where the bodies i number from 1 to κ. For the i^{th} body, $m_i \in \mathbb{R}$ is the mass, $J_i \in \mathbb{R}^{3\times3}$ is the moment of inertia, $r_i \in \mathbb{R}^3$ is the position of the center of mass, $\psi_i \in \mathbb{R}^3$ is the orientation expressed by Euler angles, and $\varpi_i \in \mathbb{R}^3$ is the angular velocity. When referring to these quantities for an arbitrarily chosen reference body B, subscript i is dropped off from the variables, and $r, \psi, \varpi \in \mathbb{R}^3$ are used.

The generalized coordinates are chosen as $q := \mathrm{col}(w, \theta)$ where $w \in \mathbb{R}^3$ is the position of the rectifier's center of mass, and $\theta := \mathrm{col}(\psi, \phi)$ contains the orientation of the rectifier represented by $\psi \in \mathbb{R}^3$, and body shape $\phi \in \mathbb{R}^\ell$ describing the position and orientation of the κ rigid bodies with respect to the body frame. The position and velocity of body i can be expressed in terms of the generalized coordinates as

$$r_i = w + p_i(\theta), \quad \dot{r}_i = \dot{w} + \left(\frac{\partial p_i}{\partial \theta}\right)^{\mathsf{T}} \dot{\theta}, \tag{A.1}$$

where $p_i(\theta)$ is a function of θ depending on body i and the rectifier's geometry. The angular velocity is given by $\varpi_i = P(\psi_i)\dot{\psi}_i$ for a matrix-valued function $P(\psi_i)$, and can be expressed in terms of θ and $\dot{\theta}$.

Consider an arbitrary point c on body i, shown in Fig.2.1 where (X, Y, Z) is the inertial

frame with origin o, and (x, y, z) is the body frame with origin b at the center of mass. The position of point c with respect to origin o in the inertial frame is given by

$$\sigma_i(\mathrm{s}) = r_i + \Omega(\psi_i)^\intercal \mathrm{s},$$

where s is the vector from point o' to point c in the (x, y, z) frame, and $\Omega(\psi_i)$ is the rotation matrix. The velocity of point c can then be expressed as

$$\dot{\sigma}_i(\mathrm{s}) = \dot{r}_i + \Omega(\psi_i)^\intercal(\varpi_i \times \mathrm{s}) = \dot{r}_i + \Omega(\psi_i)^\intercal Q(\varpi_i)\mathrm{s},$$

where $\times$ denotes the cross product, and $\frac{d}{dt}\Omega(\psi_i) = Q(\varpi_i)^\intercal \Omega(\psi_i)$ for skew symmetric matrix $Q(z) \in \mathbb{R}^{3\times 3}$ built from the elements of z such that $z \times x = Q(z)x = Q(x)^\intercal z$.

The kinetic energy of an infinitesimal segment located at point c is

$$d\mathrm{T}_i = \frac{1}{2}\|\dot{\sigma}_i(\mathrm{s})\|^2 dm_i,$$

where dm_i is the mass of the segment. Integrating $d\mathrm{T}_i$ over body i and taking the summation over the κ bodies, the total kinetic energy is given by (2.2) with

$$\mathsf{J}(\theta) := \sum_{i=1}^{\kappa} \left(m_i \mathsf{Q}_i(\theta)\mathsf{Q}_i(\theta)^\intercal + \mathsf{P}_i(\theta) J_i \mathsf{P}_i(\theta)^\intercal \right),$$
$$\mathsf{Q}_i(\theta) := \left(\frac{\partial p_i}{\partial \theta}\right) \Omega(\psi_i)^\intercal, \qquad \mathsf{P}_i(\theta) := \left(\frac{\partial \psi_i}{\partial \theta}\right) P(\psi_i)^\intercal.$$

The generalized forces from the environment are given by (2.3) with

$$\mathsf{C}(\theta) := \sum_{i=1}^{\kappa} \Omega(\psi_i)^\intercal C_i \Omega(\psi_i), \qquad C_i := \int \Delta_i da_i,$$
$$\mathsf{E}(\theta) := \sum_{i=1}^{\kappa} \mathsf{Q}_i(\theta) C_i \Omega(\psi_i), \qquad D_i := \int Q(\mathrm{s})\Delta_i Q(\mathrm{s})^\intercal da_i,$$
$$\mathsf{D}(\theta) := \sum_{i=1}^{\kappa} \left(\mathsf{Q}_i(\theta) C_i \mathsf{Q}_i(\theta)^\intercal + \mathsf{P}_i(\theta) D_i \mathsf{P}_i(\theta)^\intercal \right),$$

where we assume that each body has a uniform density and shape such that $\int s\, da_i = 0$.

Using the Euler-Lagrange equation (2.1), the equations of motion for the general mechanical rectifier are derived and given by (2.4) with

$$\mathsf{G}(\theta, \dot{\theta}) := \left(\frac{\partial \mathsf{J}(\theta)\dot{\theta}}{\partial \theta}\right)^\intercal - \frac{1}{2}\left(\frac{\partial \mathsf{J}(\theta)\dot{\theta}}{\partial \theta}\right), \quad k(\theta) := \frac{\partial V(\theta)}{\partial \theta},$$

where $V(\theta)$ is the elastic potential energy due to body deformation.

A.2 Definitions of coefficient matrices in (2.5)

We now introduce a coordinate transformation to replace $\dot{\theta}$ and $\dot{w}$ by $\dot{\xi}$ and ν, respectively, where

$$\nu := \Omega(\psi)\dot{w}, \qquad \dot{\xi} = \Gamma(\psi)\dot{\theta}, \qquad \dot{\xi} := \begin{bmatrix} \varpi \\ \dot{\phi} \end{bmatrix}, \qquad \Gamma(\psi) := \begin{bmatrix} P(\psi) & 0 \\ 0 & I \end{bmatrix}.$$

Given the definitions above, the acceleration of the center of mass, seen in the body frame, is given by

$$\Omega(\psi)\ddot{w} = \dot{\nu} + Q(\varpi)\nu,$$

and the acceleration of the orientation/shape variable θ is expressed in the new coordinates as

$$\ddot{\theta} := \Gamma(\psi)^{-1}\ddot{\xi} + \frac{d}{dt}\Gamma(\psi)^{-1}\dot{\xi}.$$

Expressing the equations in (2.4) by the new variables $(\nu, \dot{\nu})$ and $(\dot{\xi}, \ddot{\xi})$, and multiplying the equations from the left by $\Gamma(\psi)^{-\intercal}$ and $\Omega(\psi)$, respectively, results in (2.5) with

$$\begin{aligned} \mathcal{J}(\phi) &:= \Gamma(\psi)^{-\intercal}\mathsf{J}(\theta)\Gamma(\psi)^{-1}, & \mathcal{E}(\phi) &:= \Gamma(\psi)^{-\intercal}\mathsf{E}(\theta)\Omega(\psi)^{\intercal}, \\ \mathcal{D}(\phi) &:= \Gamma(\psi)^{-\intercal}\mathsf{D}(\theta)\Gamma(\psi)^{-1}, & \mathcal{C}(\phi) &:= \Omega(\psi)\mathsf{C}(\theta)\Omega(\psi)^{\intercal} \\ g(\phi, \dot{\xi}) &:= -\mathcal{J}(\phi)\dot{\Gamma}(\psi, \dot{\psi})\dot{\theta} + \Gamma(\psi)^{-\intercal}\mathsf{G}(\theta, \dot{\theta})\dot{\theta}, \end{aligned}$$

where $\dot{\Gamma}(\psi, \dot{\psi}) := \frac{d}{dt}(\Gamma(\psi))$ and we note that $\Gamma(\psi)^{-\intercal}k(\theta) = k(\theta) =: \mathsf{k}(\phi)$ and $\Gamma(\psi)^{-\intercal}B = B$, as the first three rows of $k(\theta)$ and B are zero, and the potential $V(\theta)$ is a function of ϕ only. In the above equations, the right hand sides appear to depend on ψ, but they are actually independent of ψ as indicated by the left hand sides' notation. We will show this in the following.

First note that function $p_i(\theta)$ in (A.1) can be denoted by

$$p_i(\theta) = \Omega(\psi)^{\intercal} b_i(\phi),$$

where $b_i(\phi) \in \mathbb{R}^3$ is the position of the center of mass relative to the center of mass of the entire system, expressed in the reference body frame. Let variables ψ_i^* be the Euler angles of body i relative to body B that only depend on ϕ, and satisfy

$$\Omega(\psi_i) = \Omega(\psi_i^*)\Omega(\psi).$$

One can then verify the following identities:

$$\Gamma(\psi)^{-\mathsf{T}}\mathsf{Q}_i(\theta) = \mathcal{Q}_i(\phi), \qquad \mathcal{Q}_i(\phi) := \begin{bmatrix} Q(b_i) \\ \partial b_i/\partial\phi \end{bmatrix} \Omega(\psi_i^*)^{\mathsf{T}}.$$

$$\Gamma(\psi)^{-\mathsf{T}}\mathsf{P}_i(\theta) = \mathcal{P}(\phi), \qquad \mathcal{P}(\phi) := \begin{bmatrix} \Omega(\psi_i^*)^{\mathsf{T}} \\ (\partial\psi_i^*/\partial\phi)P(\psi_i^*)^{\mathsf{T}} \end{bmatrix}.$$

Using the above, the coefficient matrices can be written as

$$\begin{aligned}
\mathcal{J}(\phi) &= \sum_{i=1}^{\kappa} \Big(m_i \mathcal{Q}_i(\phi)\mathcal{Q}_i(\phi)^{\mathsf{T}} + \mathcal{P}_i(\phi) J_i \mathcal{P}_i(\phi)^{\mathsf{T}} \Big), \\
\mathcal{D}(\phi) &= \sum_{i=1}^{\kappa} \Big(\mathcal{Q}_i(\phi) C_i \mathcal{Q}_i(\phi)^{\mathsf{T}} + \mathcal{P}_i(\phi) D_i \mathcal{P}_i(\phi)^{\mathsf{T}} \Big), \\
\mathcal{C}(\phi) &= \sum_{i=1}^{\kappa} \Omega(\psi_i^*)^{\mathsf{T}} C_i \Omega(\psi_i^*), \qquad \mathcal{E}(\phi) = \sum_{i=1}^{\kappa} \mathcal{Q}_i(\phi) C_i \Omega(\psi_i^*), \\
g(\phi,\dot{\xi}) &= -\mathcal{J}(\phi)\dot{\Gamma}(\psi,\dot{\psi})\dot{\theta} + \Gamma(\psi)^{-\mathsf{T}}\mathsf{G}(\theta,\dot{\theta})\dot{\theta},
\end{aligned}$$

It is clear that $\mathcal{J}(\phi)$, $\mathcal{C}(\phi)$, $\mathcal{D}(\phi)$, $\mathcal{E}(\phi)$ are independent of body orientation ψ and only a function of the shape ϕ. Yet, it remains to show that the right hand side of the $g(\phi,\dot{\xi})$ equation can be expressed in terms of ϕ, $\dot{\phi}$, and ϖ, without involving ψ. This is formally stated and proven in the following lemma.

Lemma 11. *The function*

$$\mathrm{g}(\theta,\dot{\theta}) := -\mathcal{J}(\phi)\dot{\Gamma}(\psi,\dot{\psi})\dot{\theta} + \Gamma(\psi)^{-\mathsf{T}}\mathsf{G}(\theta,\dot{\theta})\dot{\theta}$$

can be written as $\mathrm{g}(\theta,\dot{\theta}) = g(\phi,\dot{\xi})$ *for some function* $g(\cdot,\cdot)$.

Proof. First note that the following identities hold for an arbitrary vector $a \in \mathbb{R}^3$:

$$\begin{aligned}
&\left(\frac{\partial \Omega(\psi)^{\mathsf{T}} a}{\partial \psi}\right)^{\mathsf{T}} = \Omega(\psi)^{\mathsf{T}} Q(a)^{\mathsf{T}} P(\psi), \\
&\left(\frac{\partial P(\psi) a}{\partial \psi}\right)^{\mathsf{T}} \dot{\psi} = \dot{P}(\psi,\dot{\psi})a, \qquad \dot{P}(\psi,\dot{\psi}) := \frac{dP(\psi)}{dt}, \\
&\left(\frac{\partial P(\psi)^{\mathsf{T}} a}{\partial \psi}\right) \dot{\psi} = \mathrm{Z}(\psi,\dot{\psi})a, \qquad \mathrm{Z}(\psi,\dot{\psi}) := \frac{\partial P(\psi)\dot{\psi}}{\partial \psi}.
\end{aligned}$$

The function $\mathrm{g}(\theta,\dot{\theta})$ can then be written as

$$\mathrm{g}(\theta,\dot{\theta}) = -\mathcal{J}(\phi)\begin{bmatrix}\dot{P}(\psi,\dot{\psi})\dot{\psi}\\ 0\end{bmatrix} + \Gamma(\psi)^{-\mathsf{T}}\left(\left(\frac{\partial \mathrm{J}(\theta)\dot{\theta}}{\partial\theta}\right)^{\mathsf{T}} - \frac{1}{2}\left(\frac{\partial \mathrm{J}(\theta)\dot{\theta}}{\partial\theta}\right)\right)\dot{\theta}.$$

The above partial derivative terms can be simplified by:

$$\left(\frac{\partial \mathrm{J}(\theta)\dot{\theta}}{\partial\theta}\right)^{\mathsf{T}}\dot{\theta} = \Gamma(\psi)^{\mathsf{T}}\left(\frac{\partial \mathcal{J}(\phi)\dot{\xi}}{\partial\phi}\right)^{\mathsf{T}}\dot{\phi} + \dot{\Gamma}(\psi,\dot{\psi})^{\mathsf{T}}\mathcal{J}(\phi)\dot{\xi} + \Gamma(\psi)^{\mathsf{T}}\mathcal{J}(\phi)\begin{bmatrix}\mathrm{Z}(\psi,\dot{\psi})^{\mathsf{T}}\dot{\psi}\\ 0\end{bmatrix},$$

$$\left(\frac{\partial \mathrm{J}(\theta)\dot{\theta}}{\partial\theta}\right)\dot{\theta} = \begin{bmatrix}2\begin{bmatrix}\mathrm{Z}(\psi,\dot{\psi}) & 0\end{bmatrix}\mathcal{J}(\phi)\dot{\xi}\\ \dfrac{\partial \mathcal{J}(\phi)\dot{\xi}}{\partial\phi}\dot{\xi}\end{bmatrix}.$$

Using these simplifications, $\mathrm{g}(\theta,\dot{\theta})$ becomes

$$\mathrm{g}(\theta,\dot{\theta}) = \left(\frac{\partial \mathcal{J}(\phi)\dot{\xi}}{\partial\phi}\right)^{\mathsf{T}}\dot{\phi} + \begin{bmatrix}\begin{bmatrix}\mathrm{R}(\psi,\dot{\psi}) & 0\end{bmatrix}\mathcal{J}(\phi)\dot{\xi}\\ -\dfrac{\partial \mathcal{J}(\phi)\dot{\xi}}{2\partial\phi}\dot{\xi}\end{bmatrix},$$

where $\mathrm{R}(\psi,\dot{\psi}) := P(\psi)^{-\mathsf{T}}\left(\dot{P}(\psi,\dot{\psi})^{\mathsf{T}} - \mathrm{Z}(\psi,\dot{\psi})\right)$. Finally, it can be shown that $\mathrm{R}(\psi,\dot{\psi}) = Q(\varpi)$ using the commutative property and the Jacobi identity:

$$\frac{\partial}{\partial\psi}\left(\frac{d\Omega(\psi)^{\mathsf{T}}a}{dt}\right) = \frac{d}{dt}\left(\frac{\partial\Omega(\psi)^{\mathsf{T}}a}{\partial\psi}\right),$$

$$Q(a)Q(\varpi)^{\mathsf{T}} + Q(\varpi)Q(a) = Q(Q(a)^{\mathsf{T}}\varpi).$$

Thus, $\mathrm{R}(\psi,\dot{\psi})$ is a function of ϖ, and hence $\mathrm{g}(\theta,\dot{\theta})$ is a function of ϕ and $\dot{\xi}$. □

A.3 Some details of approximations leading to (2.7)

Approximate equations of motion in (2.7) are derived from (2.5), assuming that body deformation φ, angular acceleration $\dot{\varpi}$, and velocity components δ normal to the direction of locomotion $\mathbb{V}$ are small and of order ϵ, where $\varphi := \phi - \eta$, $\delta := \mathrm{N}^{\mathsf{T}}\boldsymbol{\nu}$, $\mathrm{N} := [\,e_1\ e_3\,]$, and e_i is the i^{th} column of the 3×3 identity matrix.

The terms in (2.5) can be approximated by Taylor series expansion and truncation as

follows:

$$
\begin{aligned}
&\mathcal{J}(\phi)\ddot{\xi} = \mathcal{J}(\eta)\ddot{\zeta} + \mathcal{O}(\epsilon^2),\\
&g(\phi,\dot{\xi}) = \mathrm{G}(\varpi)\dot{\zeta} + \mathrm{G}_1(\varpi\varpi^\intercal)\varphi + \mathcal{O}(\epsilon^2),\\
&\mathcal{D}(\phi)\dot{\xi} = \mathcal{D}(\eta)\dot{\zeta} + \mathrm{D}_1(\varpi)\varphi + \mathcal{O}(\epsilon^2),\\
&\mathcal{E}(\phi)\nu = \cancel{\mathcal{E}(\eta)e_2 v} + \mathcal{E}(\eta)\mathrm{N}\delta + v\Lambda\varphi + \mathcal{O}(\epsilon^2),\\
&\mathrm{k}(\phi) = \cancel{\mathrm{k}(\eta)} + \mathrm{K}\varphi + \mathcal{O}(\epsilon^2),\\
&\mathrm{N}^\intercal Q(\varpi)\nu = v\mathcal{R}\varpi + \mathrm{N}^\intercal Q(\varpi)\mathrm{N}\delta,\\
&e_2^\intercal Q(\varpi)\nu = -(\mathcal{R}\varpi)^\intercal\delta,\\
&\mathrm{N}^\intercal\mathcal{C}(\phi)\nu = \cancel{\mathrm{N}^\intercal\mathcal{C}(\eta)e_2 v} + \mathrm{N}^\intercal\mathcal{C}(\eta)\mathrm{N}\delta + v\mathcal{Q}\varphi + \mathcal{O}(\epsilon^2),\\
&e_2^\intercal\mathcal{C}(\phi)\nu = \cancel{e_2^\intercal\mathcal{C}(\eta)\mathrm{N}\delta} + c(\varphi)v + (\mathcal{Q}\varphi)^\intercal\delta + \mathcal{O}(\epsilon^3),\\
&\mathrm{N}^\intercal\mathcal{E}(\phi)^\intercal\dot{\xi} = \mathrm{N}^\intercal\mathcal{E}(\eta)^\intercal\dot{\zeta} + \mathrm{E}(\varpi)\varphi + \mathcal{O}(\epsilon^2),\\
&e_2^\intercal\mathcal{E}(\phi)^\intercal\dot{\xi} = \cancel{e_2^\intercal\mathcal{E}(\eta)^\intercal\dot{\zeta}} + (\Lambda\varphi)^\intercal\dot{\zeta} + \varphi^\intercal\mathrm{F}(\varpi)\varphi + \mathcal{O}(\epsilon^3),
\end{aligned}
$$

where $\dot{\zeta} := \mathrm{col}(\varpi, \dot{\varphi})$ and $v := e_2^\intercal\nu$. Functions G, G_1, D_1, E, and F are linear (without constant terms) and function $c(\varphi)$ is the quadratic approximation of $e_2^\intercal\mathcal{C}(\phi)e_2$. All the terms depend on η and the canceled terms are zero due to the nominal shape properties. Thus, (2.5) approximates to

$$
\begin{aligned}
&J\ddot{\zeta} + D(\varpi)\dot{\zeta} + K(\varpi, v)\varphi + E\delta = Bu,\\
&m\dot{\delta} + C(\varpi)\delta + m\mathcal{R}\varpi v + E^\intercal\dot{\zeta} + \mathrm{L}(\varpi, v)\varphi = 0,\\
&m\dot{v} + c(\varphi)v + (\mathcal{Q}\varphi - m\mathcal{R}\varpi)^\intercal\delta + (\Lambda\varphi)^\intercal\dot{\zeta} + \varphi^\intercal\mathrm{F}(\varpi)\varphi = 0,
\end{aligned}
$$

where $\mathcal{O}(\epsilon^2)$ and $\mathcal{O}(\epsilon^3)$ terms are neglected in the first two and the last equations, respectively, and

$$
\begin{aligned}
&J := \mathcal{J}(\eta), \quad E := \mathcal{E}(\eta)\mathrm{N}, \quad D(\varpi) := \mathcal{D}(\eta) + \mathrm{G}(\varpi),\\
&\mathrm{L}(\varpi, v) := v\mathcal{Q} + \mathrm{E}(\varpi), \qquad C(\varpi) := \mathrm{N}^\intercal(mQ(\varpi) + \mathcal{C}(\eta))\mathrm{N},\\
&K(\varpi, v) := \mathrm{G}_1(\varpi\varpi^\intercal) + \mathrm{D}_1(\varpi) + v\Lambda + \mathrm{K},
\end{aligned}
$$

Finally, it can readily be seen that the approximate equations can be expressed in a more compact form as (2.7).

APPENDIX B

Modeling Details for Saithe Fish

The saithe fish is modeled with a main body and two undulating panels with two rotating joints, as described in Section 3.2. This section provides details for the derivation of the equations of motion. The variables are summarized in Table B.1. Consider an external force $\xi(t)$ acting on the main body to regulate the swim speed such that $\dot{x}_o(t) = -v$ with a constant $v > 0$. We will write down the nonlinear equations of motion and obtain the linearization assuming θ is small. Further assuming periodic motion $\theta(t)$, we will write down the thrust-drag balance equation by setting the average value of $\xi(t)$ over a cycle to zero.

Table B.1: List of model variables ($i = 1, 2$)

x_o	x-position of the center of mass (C.M.) of the main body
x_i	x-position of the C.M. of the ith panel
y_i	y-position of the C.M. of the ith panel
θ_i	angle between the ith panel and the x-axis
u_i	bending moment applied at joint i
w_i	velocity of fluid pushed by the ith panel in y direction
a_i	acceleration of fluid pushed by the ith panel

The hydrodynamic forces and torques acting on the body are given by:

$$f_o = -\text{sgn}(\dot{x}_o) c \dot{x}_o^2, \qquad f_i = m_{A_i} a_i / \cos\,\theta_i, \qquad \tau_i = -(m_{A_i} l_i^2/3)\ddot{\theta}_i,$$

for $i = 1, 2$, where

$$m_{A_i} := \rho V_i c_{A_i}, \qquad V_i := \pi (d_i/2)^2 (2l_i).$$

The kinematic and dynamic equations are given by:

$$
\begin{aligned}
x_1 &= x_o + l_o + l_1\cos\theta_1, & m_o\ddot{x}_o &= g_{x_1} + f_o + \xi,\\
x_2 &= x_1 + l_1\cos\theta_1 + l_2\cos\theta_2, & m_1\ddot{x}_1 &= f_1\sin\theta_1 - g_{x_1} + g_{x_2},\\
y_1 &= y_o + l_1\sin\theta_1, & m_2\ddot{x}_2 &= f_2\sin\theta_2 - g_{x_2},\\
y_2 &= y_1 + l_1\sin\theta_1 + l_2\sin\theta_2, & m_1\ddot{y}_1 &= -f_1\cos\theta_1 - g_{y_1} + g_{y_2},\\
w_i &= \dot{y}_i - \dot{x}_i\theta_i, & m_2\ddot{y}_2 &= -f_2\cos\theta_2 - g_{y_2},\\
a_i &= \ddot{y}_i - \ddot{x}_i\theta_i - 2\dot{x}_i\dot{\theta}_i, & J_1\ddot{\theta}_1 &= \tilde{u}_2 - \tilde{u}_1 + \tau_1 - (g_{x_1} + g_{x_2})l_1\sin\theta_1 + (g_{y_1} + g_{y_2})l_1\cos\theta_1,\\
& & J_2\ddot{\theta}_2 &= -\tilde{u}_2 + \tau_2 - g_{x_2}l_2\sin\theta_2 + g_{y_2}l_2\cos\theta_2,
\end{aligned}
$$

where g_{x_i} and g_{y_i} are constraint forces due to the neighboring panel(s), and $\tilde{u}_i$ are the total bending moments containing the effects of active muscle and body flexibility:

$$\tilde{u}_1 = u_1 + k_1\theta_1, \qquad \tilde{u}_2 = u_2 + k_2(\theta_2 - \theta_1).$$

The dynamic equations for translational motion can be solved for the constraint forces to give:

$$
\begin{bmatrix} g_{x_1} \\ g_{x_2} \end{bmatrix} = -\begin{bmatrix} 1 & 1 \\ 0 & 1 \end{bmatrix}\begin{bmatrix} m_1\ddot{x}_1 - f_1\sin\theta_1 \\ m_2\ddot{x}_2 - f_2\sin\theta_2 \end{bmatrix},
$$

$$
\begin{bmatrix} g_{y_1} \\ g_{y_2} \end{bmatrix} = -\begin{bmatrix} 1 & 1 \\ 0 & 1 \end{bmatrix}\begin{bmatrix} m_1\ddot{y}_1 + f_1\cos\theta_1 \\ m_2\ddot{y}_2 + f_2\cos\theta_2 \end{bmatrix}.
$$

These expressions are substituted into the rotational equations of tail motion. In the equation for the main body, the average of the external force $\xi(t)$ over one cycle is set to zero such that the average thrust balances the average drag:

$$\overline{\xi} = 0 = \overline{f_1\sin\theta_1 + f_2\sin\theta_2} + \overline{f_o}.$$

Assuming small $\theta_i = O(\epsilon)$ and neglecting $O(\epsilon^2)$ terms in the tail motion equation and $O(\epsilon^3)$ terms in the thrust drag balance equation, we find the following linear and bilinear equations of motion:

$$
\begin{aligned}
&J\ddot{\theta} + 2vG\dot{\theta} + K\theta = Bu,\\
&\overline{\theta^{\intercal}G^{\intercal}\ddot{\theta}} + cv^2 = 0,
\end{aligned}
$$

with the following parameter definitions:

$$J := L(M+M_A)L/3 + F^\intercal(M+M_A)F, \quad G := F^\intercal M_A, \quad K := BK_oB,$$

$$F := \begin{bmatrix} l_1 & 0 \\ 2l_1 & l_2 \end{bmatrix}, \quad B := \begin{bmatrix} -1 & 1 \\ 0 & -1 \end{bmatrix}, \quad \begin{aligned} M &:= \mathrm{diag}(m_1, m_2), & K_o &:= \mathrm{diag}(k_1, k_2), \\ M_A &:= \mathrm{diag}(m_{A_1}, m_{A_2}), & L &:= \mathrm{diag}(l_1, l_2), \end{aligned}$$

where $\theta, u \in \mathbb{R}^2$ are two dimensional vectors obtained by stacking θ_i and u_i for $i = 1, 2$, respectively. This two-input case with $u \in \mathbb{R}^2$ is considered in Section 3.4.2.3. In all other analyses, the tail is assumed passive ($u_2(t) \equiv 0$), and u and B are redefined as $u := u_1$ and $B := \begin{bmatrix} -1 & 0 \end{bmatrix}^\intercal$.

References

[1] F. Hess and J. J. Videler, "Fast continuous swimming of saithe (pollachius virens): a dynamic analysis of bending moments and muscle power," *Journal of Experimental Biology*, vol. 109, no. 1, pp. 229–251, 1984.

[2] J. J. Videler and F. Hess, "Fast continuous swimming of two pelagic predators, saithe (pollachius virens) and mackerel (scomber scombrus): a kinematic analysis," *Journal of Experimental Biology*, vol. 109, no. 1, pp. 209–228, 1984.

[3] R. W. Brockett, "On the rectification of vibratory motion," *Sensors Actuators*, vol. 20, pp. 91–96, 1989.

[4] M. H. Dickinson, C. T. Farley, R. J. Full, M. A. R. Koehl, R. Kram, and S. Lehman, "How animals move: an integrative view," *Science*, vol. 288, no. 5463, pp. 100–106, 2000.

[5] R. D. Beer, "A dynamical systems perspective on agent-environment interaction," *Artificial intelligence*, vol. 72, no. 1–2, pp. 173–215, 1995.

[6] A. Lesne, "Chaos in biology," in *Rivista di Biologia Biology Forum*, vol. 99, no. 3. Anicia Srl, 2006, p. 467.

[7] P. Faure and H. Korn, "Is there chaos in the brain? i. concepts of nonlinear dynamics and methods of investigation," *Comptes Rendus Biologies*, vol. 324, no. 9, pp. 773–793, 2001.

[8] H. Korn and P. Faure, "Is there chaos in the brain? ii. experimental evidence and related models," *Comptes Rendus Biologies*, vol. 326, no. 9, pp. 787–840, 2003.

[9] F. Delcomyn, "Neural basis of rhythmic behavior in animals," *Science*, vol. 210, no. 4469, pp. 492–498, 1980.

[10] M. Rabinovich and H. Abarbanel, "The role of chaos in neural systems," *Neuroscience*, vol. 87, no. 1, pp. 5–14, 1998.

[11] G. Bessonnet, S. Chesse, and P. Sardain, "Optimal gait synthesis of a seven-link planar biped," *International Journal of Robotics Research*, vol. 23, no. 10–11, pp. 1059–1073, 2004.

[12] G. Hicks and K. Ito, "A method for determination of optimal gaits with application to a snake-like serial-link structure," *IEEE Transactions on Automatic Control*, vol. 50, no. 9, pp. 1291–1306, 2005.

[13] J. Cortés, S. Martínez, J. P. Ostrowski, and K. A. McIsaac, "Optimal gaits for dynamic robotic locomotion," *International Journal of Robotics Research*, vol. 20, no. 9, pp. 707–728, 2001.

[14] J. P. Ostrowski, J. P. Desai, and V. Kumar, "Optimal gait selection for nonholonomic locomotion systems," *International Journal of Robotics Research*, vol. 19, no. 3, pp. 225–237, 2000.

[15] T. Saidouni and G. Bessonnet, "Generating globally optimised sagittal gait cycles of a biped robot," *Robotica*, vol. 21, no. 2, pp. 199–210, 2003.

[16] M. Srinivasan and A. Ruina, "Computer optimization of a minimal biped model discovers walking and running," *Nature*, vol. 439, no. 7072, pp. 72–75, 2006.

[17] K. Nagasaka, H. Inoue, and M. Inaba, "Dynamic walking pattern generation for a humanoid robot based on optimal gradient method," in *IEEE International Conference on Systems, Man and Cybernetics*, vol. 6, 1999, pp. 908–913.

[18] C. Chevallereau and Y. Aoustin, "Optimal reference trajectories for walking and running of a biped robot," *Robotica*, vol. 19, no. 5, pp. 557–569, 2001.

[19] M. Saito, M. Fukaya, and T. Iwasaki, "Modeling, analysis, and synthesis of serpentine locomotion with a multilink robotic snake," *IEEE Control Systems Magazine*, vol. 22, no. 1, pp. 64–81, 2002.

[20] K. A. McIsaac and J. P. Ostrowski, "Motion planning for anguilliform locomotion," *IEEE Transactions on Robotics and Automation*, vol. 19, no. 4, pp. 637–652, 2003.

[21] J. Blair and T. Iwasaki, "Optimal gaits for mechanical rectifier systems," *IEEE Transactions on Automatic Control*, vol. 56, no. 1, pp. 59–71, 2011.

[22] C. Ye, S. Ma, B. Li, and Y. Wang, "Turning and side motion of snake-like robot," in *IEEE International Conference on Robotics and Automation*, vol. 5, 2004, pp. 5075–5080.

[23] J. H. Long and K. S. Nipper, "The importance of body stiffness in undulatory propulsion," *American Zoologist*, vol. 36, no. 6, pp. 678–694, 1996.

[24] J. H. Long, "Muscles, elastic energy, and the dynamics of body stiffness in swimming eels," *American Zoologist*, vol. 38, no. 4, pp. 771–792, 1998.

[25] D. A. Pabst, "Springs in swimming animals," *American Zoologist*, vol. 36, no. 6, pp. 723–735, 1996.

[26] J. H. Long, M. Hale, M. J. McHenry, and M. W. Westneat, "Functions of fish skin: flexural stiffness and steady swimming of longnose gar, lepisosteus osseus," *Journal of Experimental Biology*, vol. 199, no. 10, pp. 2139–2151, 1996.

[27] R. Bainbridge, "The speed of swimming of fish as related to size and to the frequency and amplitude of the tail beat," *Journal of Experimental Biology*, vol. 35, no. 1, pp. 109–133, 1958.

[28] P. W. Webb, "Effects of partial caudal-fin amputation on the kinematics and metabolic rate of underyearling sockeye salmon (oncorhynchus nerka) at steady swimming speeds," *Journal of Experimental Biology*, vol. 59, no. 3, pp. 565–582, 1973.

[29] M. J. McHenry, C. A. Pell, and J. H. Long, "Mechanical control of swimming speed: stiffness and axial wave form in undulating fish models," *Journal of Experimental Biology*, vol. 198, no. 11, pp. 2293–2305, 1995.

[30] G. S. Triantafyllou, M. S. Triantafyllou, and M. A. Grosenbaugh, "Optimal thrust development in oscillating foils with application to fish propulsion," *Journal of Fluids and Structures*, vol. 7, no. 2, pp. 205–224, 1993.

[31] G. K. Taylor, R. L. Nudds, and A. L. R. Thomas, "Flying and swimming animals cruise at a strouhal number tuned for high power efficiency," *Nature*, vol. 425, no. 6959, pp. 707–711, 2003.

[32] M. S. Triantafyllou, G. S. Triantafyllou, and D. K. P. Yue, "Hydrodynamics of fishlike swimming," *Annual review of Fluid Mechanics*, vol. 32, no. 1, pp. 33–53, 2000.

[33] G. C. Lewin and H. Haj-Hariri, "Modelling thrust generation of a two-dimensional heaving airfoil in a viscous flow," *Journal of Fluid Mechanics*, vol. 492, pp. 339–362, 2003.

[34] K. W. Moored, P. A. Dewey, A. J. Smits, and H. Haj-Hariri, "Hydrodynamic wake resonance as an underlying principle of efficient unsteady propulsion," *Journal of Fluid Mechanics*, vol. 708, pp. 329–348, 2012.

[35] S. Mitra, M. A. Riley, and M. T. Turvey, "Chaos in human rhythmic movement," *Journal of Motor Behavior*, vol. 29, no. 3, pp. 195–198, 1997.

[36] N. Stergiou and L. M. Decker, "Human movement variability, nonlinear dynamics, and pathology: is there a connection?" *Human Movement Science*, vol. 30, no. 5, pp. 869–888, 2011.

[37] U. H. Buzzi, N. Stergiou, M. J. Kurz, P. A. Hageman, and J. Heidel, "Nonlinear dynamics indicates aging affects variability during gait," *Clinical Biomechanics*, vol. 18, no. 5, pp. 435–443, 2003.

[38] F. Cignetti, F. Schena, and A. Rouard, "Effects of fatigue on inter-cycle variability in cross-country skiing," *Journal of Biomechanics*, vol. 42, no. 10, pp. 1452–1459, 2009.

[39] M. J. Kurz and N. Stergiou, "An artificial neural network that utilizes hip joint actuations to control bifurcations and chaos in a passive dynamic bipedal walking model," *Biological Cybernetics*, vol. 93, no. 3, pp. 213–221, 2005.

[40] S. Steingrube, M. Timme, F. Wörgötter, and P. Manoonpong, "Self-organized adaptation of a simple neural circuit enables complex robot behaviour," *Nature Physics*, vol. 6, no. 3, pp. 224–230, 2010.

[41] Y. Kuniyoshi and S. Suzuki, "Dynamic emergence and adaptation of behavior through embodiment as coupled chaotic field," in *IEEE Proceedings Intelligent Robots and Systems*, vol. 2. IEEE, 2004, pp. 2042–2049.

[42] H. Castellini, E. Yudiarsah, L. Romanelli, and H. A. Cerdeira, "Coupled chaotic oscillators and their relation to a central pattern generator for artificial quadrupeds," *Pramana*, vol. 64, no. 4, pp. 525–534, 2005.

[43] O. V. Popovych, C. Hauptmann, and P. A. Tass, "Effective desynchronization by nonlinear delayed feedback," *Physical Review Letters*, vol. 94, no. 16, p. 164102, 2005.

[44] G. Miritello, A. Pluchino, and A. Rapisarda, "Phase transitions and chaos in long-range models of coupled oscillators," *Europhysics Letters*, vol. 85, no. 1, p. 10007, 2009.

[45] O. V. Popovych, Y. L. Maistrenko, and P. A. Tass, "Phase chaos in coupled oscillators," *Physical Review E*, vol. 71, no. 6, p. 065201, 2005.

[46] X. Li and G. Chen, "Synchronization and desynchronization of complex dynamical networks: an engineering viewpoint," *IEEE Transactions on Circuits and Systems I: Fundamental Theory and Applications*, vol. 50, no. 11, pp. 1381–1390, 2003.

[47] I. Z. Kiss, C. G. Rusin, H. Kori, and J. L. Hudson, "Engineering complex dynamical structures: sequential patterns and desynchronization," *Science*, vol. 316, no. 5833, pp. 1886–1889, 2007.

[48] S. Yu and G. Chen, "Anti-control of continuous-time dynamical systems," *Communications in Nonlinear Science and Numerical Simulation*, vol. 17, no. 6, pp. 2617–2627, 2012.

[49] G. Taylor, "Analysis of the swimming of long and narrow animals," in *Proceedings Royal Society of London A*, vol. 214, no. 1117, 1952, pp. 158–183.

[50] J. Chen, W. O. Friesen, and T. Iwasaki, "Mechanisms underlying rhythmic locomotion: body–fluid interaction in undulatory swimming," *Journal of Experimental Biology*, vol. 214, no. 4, pp. 561–574, 2011.

[51] H. K. Khalil, *Nonlinear systems*. New Jersey: Prentice hall, 1996, vol. 3.

[52] A. L. Fradkov and V. A. Yakubovich, "The S-procedure and duality relations in nonconvex problems of quadratic programming," *Vestn. LGU, Ser. Mat., Mekh., Astron*, vol. 6, pp. 101–109, 1979.

[53] R. E. Skelton, T. Iwasaki, and D. E. Grigoriadis, *A unified algebraic approach to control design*. CRC Press, 1997.

[54] G. S. Chirikjian and J. W. Burdick, "The kinematics of hyper-redundant robot locomotion," *IEEE Transactions on Robotics and Automation*, vol. 11, no. 6, pp. 781–793, 1995.

[55] F. Boyer and M. Porez, "Multibody system dynamics for bio-inspired locomotion: from geometric structures to computational aspects," *Bioinspiration & Biomimetics*, vol. 10, no. 2, 2015.

[56] L. J. Rosenberger, "Pectoral fin locomotion in batoid fishes: undulation versus oscillation," *Journal Experimental Biology*, vol. 204, no. 2, pp. 379–394, 2001.

[57] X. Liu, T. Iwasaki, and F. Fish, "Dynamic modeling and gait analysis of batoid swimming," in *Proceedings American Control Conference*, 2013, pp. 566–571.

[58] X. Liu, F. Fish, R. S. Rusho, S. S. Blemker, and T. Iwasaki, "Modeling and optimality analysis of pectoral fin locomotion," in *Neuromechanical Modeling of Posture and Locomotion*. Springer, 2016, ch. 11, pp. 309–332.

[59] J. Y. Cheng, T. J. Pedley, and J. D. Altringham, "A continuous dynamic beam model for swimming fish," *Philosophical Transactions of the Royal Society of London B: Biological Sciences*, vol. 353, no. 1371, pp. 981–997, 1998.

[60] M. J. Lighthill, "Note on the swimming of slender fish," *Journal of Fluid Mechanics*, vol. 9, no. 02, pp. 305–317, 1960.

[61] ——, "Aquatic animal propulsion of high hydrodynamic efficiency," *Journal of Fluid Mechanics*, vol. 44, pp. 256–301, 1970.

[62] ——, "Large-amplitude elongated-body theory of fish locomotion," *Proceedings Royal Society of London B: Biological Sciences*, vol. 179, no. 1055, pp. 125–138, 1971.

[63] J. Chen, W. O. Friesen, and T. Iwasaki, "Mechanisms underlying rhythmic locomotion: interactions between activation, tension and body curvature waves," *Journal of Experimental Biology*, vol. 215, no. 2, pp. 211–219, 2012.

[64] A. R. Blight, "The muscular control of vertebrate swimming movements," *Biological Reviews*, vol. 52, no. 2, pp. 181–218, 1977.

[65] J. H. Long, M. Mchenry, and N. Boetticher, "Undulatory swimming: how traveling waves are produced and modulated in sunfish (lepomis gibbosus)," *Journal of Experimental Biology*, vol. 192, no. 1, pp. 129–145, 1994.

[66] J. D. Altringham, C. S. Wardle, and C. I. Smith, "Myotomal muscle function at different locations in the body of a swimming fish," *Journal of Experimental Biology*, vol. 182, no. 1, pp. 191–206, 1993.

[67] T. L. Daniel, "Unsteady aspects of aquatic locomotion," *American Zoologist*, vol. 24, no. 1, pp. 121–134, 1984.

[68] J. J. Rohr and F. E. Fish, "Strouhal numbers and optimization of swimming by odontocete cetaceans," *Journal of Experimental Biology*, vol. 207, no. 10, pp. 1633–1642, 2004.

[69] G. Sundnes, "Swimming speed of fish as a factor in gear research," vol. 13, no. 6, pp. 126–132, 1963.

[70] J. J. Magnuson, "Locomotion by scombrid fishes: Hydromechanics, morphology, and behavior," *Fish Physiology*, vol. 7, pp. 239–313, 1978.

[71] H. L. Fierstine and V. Walters, "Studies in locomotion and anatomy of scombroid fishes," *Biological Sciences*, p. 4, 1968.

[72] B. Ahlborn, D. G. Harper, R. W. Blake, D. Ahlborn, and M. Cam, "Fish without footprints," *Journal of Theoretical Biology*, vol. 148, no. 4, pp. 521–533, 1991.

[73] E. D. Tytell, "Kinematics and hydrodynamics of linear acceleration in eels, anguilla rostrata," *Proceedings of the Royal Society of London B: Biological Sciences*, vol. 271, no. 1557, pp. 2535–2540, 2004.

[74] F. E. Fish and J. Rohr, "Review of dolphin hydrodynamics and swimming performance," DTIC Document, Tech. Rep., 1999.

[75] M. Sfakiotakis, D. M. Lane, and J. B. C. Davies, "Review of fish swimming modes for aquatic locomotion," *IEEE Journal of Oceanic Engineering*, vol. 24, no. 2, pp. 237–252, 1999.

[76] J. R. Hunter and J. R. Zweifel, "Swimming speed, tail beat frequency, tail beat amplitude, and size in jack mackerel, trachurus-symmetricus, and other fishes," *Fishery Bulletin of the National Oceanic and Atmospheric Administration*, vol. 69, no. 2, pp. 253–266, 1971.

[77] C. Eloy, "Optimal strouhal number for swimming animals," *Journal of Fluids and Structures*, vol. 30, pp. 205–218, 2012.

[78] H. Ohashi and N. Ishikawa, "Visualization study of flow near the trailing edge of an oscillating airfoil," *Bulletin of Japan Society of Mechanical Engineers*, vol. 15, no. 85, pp. 840–847, 1972.

[79] E. L. Brainerd and S. N. Patek, "Vertebral column morphology, c-start curvature, and the evolution of mechanical defenses in tetraodontiform fishes," *Copeia*, pp. 971–984, 1998.

[80] B. K. Ahlborn, R. W. Blake, and W. M. Megill, "Frequency tuning in animal locomotion," *Zoology*, vol. 109, no. 1, pp. 43–53, 2006.

[81] J. H. Long, "Stiffness and damping forces in the intervertebral joints of blue marlin (makaira nigricans)," *Journal of Experimental Biology*, vol. 162, no. 1, pp. 131–155, 1992.

[82] R. E. Shadwick, J. F. Steffensen, S. L. Katz, and T. Knower, "Muscle dynamics in fish during steady swimming," *American Zoologist*, vol. 38, no. 4, pp. 755–770, 1998.

[83] Y. Kuramoto, *Chemical oscillations, waves, and turbulence*. Springer Science & Business Media, 2012, vol. 19.

[84] N. Tukhlina, M. Rosenblum, A. Pikovsky, and J. Kurths, "Feedback suppression of neural synchrony by vanishing stimulation," *Physical Review E*, vol. 75, no. 1, p. 011918, 2007.

[85] C. Grebogi, E. Ott, S. Pelikan, and J. A. Yorke, "Strange attractors that are not chaotic," *Physica D: Nonlinear Phenomena*, vol. 13, no. 1, pp. 261–268, 1984.

[86] H. Abarbanel and J. Gollub, "Analysis of observed chaotic data," *Physics Today*, vol. 49, no. 11, p. 81, 1996.

[87] G. L. Baker and J. P. Gollub, *Chaotic dynamics: an introduction*. Cambridge University Press, 1996.

[88] B. Eckhardt and D. Yao, "Local lyapunov exponents in chaotic systems," *Physica D: Nonlinear Phenomena*, vol. 65, no. 1, pp. 100–108, 1993.

[89] A. L. Fradkov and R. J. Evans, "Control of chaos: methods and applications in engineering," *Annual Reviews in Control*, vol. 29, no. 1, pp. 33–56, 2005.

[90] A. J. Laub, *Matrix analysis for scientists and engineers*. Siam, 2005.

[91] R. L. Taylor, "Attractors: Nonstrange to chaotic," *Society for Industrial and Applied Mathematics*, pp. 72–80, 2010.